

Diploma thesis

Nonequilibrium Green's function approach to artificial atoms

by

Karsten Balzer

Kiel, 25th May 2007



Institut für
Theoretische Physik und Astrophysik
der Christian-Albrechts-Universität zu Kiel

Supervisor/1st examiner:

Prof. Dr. Michael Bonitz

2nd examiner:

Contents

1. Introduction	3
1.1. Chapter overview	4
1.2. Notational conventions and remarks	5
2. Nonequilibrium Green's functions	7
2.1. Overview	7
2.2. Nonequilibrium Green's functions. Definitions and properties	9
2.2.1. Subordinated quantities	12
2.2.2. Contour calculus	13
2.3. Determination of macroscopic observables	14
3. Keldysh/Kadanoff-Baym equations. Basis representation	17
3.1. Keldysh/Kadanoff-Baym equations (KKBE)	17
3.2. Basis representation of the Green's function	21
3.3. Keldysh/Kadanoff-Baym equations for $g_{kl}^{M, \gtrless, \uparrow/\downarrow}(t_1, t_2)$	23
3.3.1. Self-energy contributions	26
3.3.2. KKBE in basis representation. Summary	27
3.3.3. Equilibrium Dyson equation	28
4. Numerical procedure and implementation	31
4.1. Solving the Hartree-Fock equations	31
4.1.1. Hartree-Fock eigenvalues and convergence properties	34
4.1.2. Hartree-Fock orbital (HFO) representation	35
4.2. Discretization of the Hartree-Fock Green's function	35
4.3. Solving the Dyson equation	37
4.3.1. Self-energy contributions	40
4.3.2. Computation of relevant energies	40
4.4. Program structure. Overview	42
4.5. Solving the Keldysh/Kadanoff-Baym equations	45
4.5.1. Scheme of the numerical solution of the KKBE	47
4.5.2. Memory allocation for the Green's functions	48
4.5.3. Time-dependent energies and energy conservation	49
4.5.4. Calculation of retarded and advanced quantities during propagation	51
4.5.5. Spectral function and other time-dependent observables	52
5. Equilibrium properties of artificial atoms	55
5.1. Comparison with first order perturbation theory	56
5.2. The correlated Matsubara Green's function	58
5.2.1. Effective potential in coordinate space	60
5.3. Density profile, distribution function and energies	62
5.3.1. Computations without exchange	68

5.3.2. Strongly coupled fermions in thermal equilibrium	69
5.4. Comparison with PIMC simulations	71
6. Nonequilibrium behavior	77
6.1. The nonequilibrium Green's functions $\mathbf{g}^*(t, t')$, $\star \equiv \{\gtrless, \rfloor/\rfloor\}$	77
6.1.1. Numerical costs	81
6.2. Nonequilibrium situations	81
6.3. Kohn mode in a quantum many-body system	84
7. Conclusion and outlook	91
A. Matrix elements in oscillator representation	95
A.1. Kinetic/potential energy and dipole moment	95
A.2. Matrix elements of pair-interaction potentials	96
A.2.1. Contact interaction	96
A.2.2. Coulomb	97
A.2.3. Yukawa	99
B. Time-propagation of the Green's functions	101
B.1. Time-stepping $\mathbf{g}^*(T) \rightarrow \mathbf{g}^*(T + \Delta)$, $\star \equiv \{\gtrless, \rfloor/\rfloor\}$	101
B.2. Computation of matrix elements $U_{ij}(\Delta)$ from $U(t) = \exp(-i\bar{\mathbf{h}}t)$	104
C. Characterization of laser pulses	105
C.1. Duration and spectral width	105
D. Record of (frequently) used abbreviations and symbols	107
References	109

1. Introduction

Small and mesoscopic quantum systems trapped in confinement potentials are subject of investigation in many fields of actual research. Examples are ions in electro-magnetic traps [1, 2], dusty plasmas [3, 4], finite electron and exciton systems in semiconductor quantum wells and dots [5, 6] or even more sophisticated systems like trapped ultra-cold alkali metals forming Bose-Einstein condensates [7]. All these interacting quantum systems show a spatially inhomogeneous density, and, due to their multiple similarities to conventional atoms, they are commonly referred to as *artificial atoms*, see e.g. Ashoori [8]. However, one should be aware of considerable differences in comparison with real atoms. First, artificial atoms are typically much larger than natural atoms. For instance, electrons confined in semiconductor structures typically move on length scales of 50 – 100 nm, whereas real atoms in condensed matter have extensions of only a few Ångström (0.1 nm)—moreover, if an artificial atom is composed itself of atomic components (ions, neutral atoms or molecules), the overall size can be even comparable to macroscopic scales. Second, the physical nature of confining the components into artificial atoms is different: While electrons in natural atoms dominantly move according to the intrinsic attractive central force of the nucleus, artificially made atoms are often held together by an external potential. This circumstance e.g. leads to transitions between quantum many-body states that are unknown in natural atoms or to an increased relevance of correlation phenomena which then trigger a correlated particle dynamics. With the additional possibility of controlling the particle number, artificial atoms allow for a systematic study of quantum mechanics including effects of interparticle interactions and correlations. In parallel, aside from various experimental realizations, a large number of theoretical and numerical investigations have been performed on artificially made atoms, see e.g. [8, 9, 10, 11] and references therein. However, the application of a *generalized quantum kinetic theory* (KT) [12, 13]—using the technique of nonequilibrium Green’s functions (NEGF) [14]—turns out to be widely unexplored.

Thus, being motivated by recent works on conventional atoms and molecules (N.E. Dahlen and R. van Leeuwen *et al.* [15, 16]), the objective target of the present thesis is to present a nonequilibrium Green’s function approach to artificial atoms. This not only extends previous NEGF applications that are mostly concerned with quasi-homogeneous quantum systems (non-ideal quantum gases, nuclear matter, plasmas etc.—for a more detailed overview see Chap. 2), but also places the artificially made atom on a profound theoretical basis in order to numerically study its correlated quantum many-body state in thermodynamic equilibrium as well as in nonequilibrium, i.e. under the influence of arbitrarily strong time-dependent perturbations. The overall frame bounding this treatise is thereby non-relativistic quantum-field theory (QFT) [17, 18, 19] which equally applies to Fermi and Bose systems and, since the late 1940’s, has turned out to be a powerful method for studying interacting quantum many-body systems. Together with quantum statistical mechanics and the pioneering works of Matsubara [20], Kadanoff and Baym [14, 21], and (independently) Keldysh [22], the QFT formalism then leads to the concept of (non-)equilibrium Green’s functions basing—in contrast to microscopic *first principle* or *ab initio* approaches—upon macroscopic averages.

It is important to remark that the analytic continuation of the imaginary-time equilibrium Green’s function (first introduced by Matsubara for quantum many-body systems at zero and finite temperatures) into the real-time domain serves as the natural mechanism of generating quantum kinetic equations that include dissipative processes and memory (non-Markovian) ef-

fects and, therefore, go beyond traditional Boltzmann type equations [12]. Moreover, since all perturbation theory (PT) techniques, known from equilibrium Green's function theory, can be directly transferred and applied to nonequilibrium situations, the kinetic equations for the NEGF—commonly referred to as the Keldysh/Kadanoff-Baym equations (KKBE)—can be formulated in a closed or self-consistent form by incorporating familiar quantum many-body approximations (diagrammatically represented by Feynman diagrams, e.g. [23]).

At the center of this thesis is now the numerical solution of these Keldysh/Kadanoff-Baym equations for the special case of artificial atoms. The resulting Green's functions in thermodynamic equilibrium *and* in nonequilibrium then give direct access to most of the system's macrophysical properties which will be subject of investigation. As a representative example for an artificial atom, one thereby will focus on a weakly to moderate Coulomb-interacting system of N spin-polarized or spinless charged fermions being confined in a one-dimensional parabolic trap (1D quantum dot). However, the numerical procedure will be implemented on a very general level, so that applications to (many) other inhomogeneous quantum systems are straightforward.

1.1. Chapter overview

The present work is organized follows:

Chap. 2 begins with a general overview of nonequilibrium Green's function theory and its applications to interacting quantum many-body systems. Thereafter, the underlying quantum-field theoretical basics are presented leading to the definition of the nonequilibrium Green's functions as a $2s$ -time generalization of standard s -particle density matrices, $s \in \mathbb{N}$.

At the center of Chap. 3 are the equations of motion for the Green's functions in equilibrium (also known as Dyson equation) and nonequilibrium (Keldysh/Kadanoff-Baym equations) which, in combination with conserving many-body approximations, can be formulated in a closed (or self-consistent) form. As a preliminary for later numerical treatment, the here introduced expansion of the NEGF in terms of spatial one-particle wave functions allows one to reduce the equations of motion to simpler matrix equations which instead of continuous time *and* space variables now depend on time variables only.

Basing on the groundwork of Chaps. 2 and 3, Chap. 4 covers essential details needed to construct and implement the procedure which numerically solves the equations of motions for the NEGF. The concept will thereby be to start from a (Hartree-Fock) mean-field Green's function—originating from a separate self-consistent Hartree-Fock (SCHF) calculation—which serves as reference quantity in an iterative scheme solving the Dyson equation including correlations. As the resulting thermodynamic equilibrium state may evolve in time, also the numerical strategy of attacking the Keldysh/Kadanoff-Baym equations in nonequilibrium is discussed in-depth at the end of this chapter.

The subsequent chapter, Chap. 5, analyzes the finite temperature equilibrium Green's function (computed according to the procedure explained in Chap. 4) for an artificial atom of N Coulomb-interacting spin-polarized fermions confined in a 1D parabolic trap. As the equilibrium properties, such as particle density, energy or distribution function, depend on the many-body approximation applied to treat the interactions, results at (Hartree-Fock) mean-field level are compared with those at a correlated level (second Born approximation) which allows for particle collisions. Briefly outlined are, in addition, strongly correlated fermions and a comparison of the equilibrium results with path integral Monte Carlo (PIMC) simulations.

The nonequilibrium behavior is subject of Chap. 6. Here, the equilibrium state, as is obtained from the preceding Chap. 5, is evolved in time using the two-time NEGF and numerically integrating the Keldysh/Kadanoff-Baym equations. Besides the discussion on the temporal conservation of the total energy, one also examines the dynamics of the trapped Fermi system (initially

in thermodynamic equilibrium) under influence of pulsed laser fields in dipole approximation. Such excitations generally lead to the center of mass (COM) oscillation of the harmonically confined many-body system, and, therefore, the density response allows one to test and verify the numerical accuracy of the computations.

Finally, the remaining Chap. 7 concludes the present work by giving a summarizing overview followed by some brief remarks concerning future problems and domains of applicability. The end matter of this thesis, despite of the references, contains a small number of appendices which provide detailed information—particularly concerning the numerical time-propagation of the NEGF (described in Chap. 4) and the matrix elements (in oscillator representation) of the one-particle energy and the pair-interaction potential (required in Chaps. 5 and 6).

1.2. Notational conventions and remarks

Before beginning with a theoretical introduction to nonequilibrium Green's functions in the next chapter, it is necessary to give some general remarks.

Later in this work, mainly in Chaps. 5 and 6, subject of investigation will be a harmonically confined one-dimensional ensemble of quantum particles of (effective) mass m . The corresponding N -particle Hamiltonian including an external time-dependent potential $V_{\text{ext}}(x_i, t)$ and a pair-interaction $w(x_i, x_j)$ is given by $H = H_1 + \lambda H_{12}$, where using the confinement frequency Ω

$$H_1 = \sum_{i=1}^N \left(-\frac{\hbar^2}{2m} \nabla_{x_i}^2 + \frac{m}{2} \Omega^2 x_i^2 + V_{\text{ext}}(x_i, t) \right), \quad H_{12} = \sum_{i<j} w(x_i, x_j), \quad (1.1)$$

and λ is a dimensionless coupling parameter which is directly connected with the interaction strength and the absolute value of which characterizes the degree of binary (particle-particle) correlations.

However, dealing with (1.1) in this form is involved. For systems containing harmonic entrapment, it is more convenient to introduce natural unit scales (*oscillator units*) such as the oscillator or confinement length x_0 and the oscillator energy E_0 given by

$$x_0 = \sqrt{\frac{\hbar}{m\Omega}}, \quad E_0 = \hbar\Omega. \quad (1.2)$$

The Hamiltonian then transforms into an overall dimensionless form

$$H = \sum_{i=1}^N \left(\frac{1}{2} (-\partial_{x_i}^2 + x_i^2) + \bar{V}_{\text{ext}}(x_i, t) \right) + \lambda \sum_{i<j} \bar{w}(x_i - x_j), \quad (1.3)$$

which is equivalently obtained by taking $\hbar = m = \Omega = 1$ and which suits best for numerical treatment. The bound states of the noninteracting system with $\bar{w} \equiv 0$ take in particular the energies $\epsilon_k^0 = k + \frac{1}{2}$, and the thermal equilibrium state corresponding to (1.3) is further characterized by an additional parameter—namely the inverse temperature $\beta = 1/k_B T$ (with Boltzmann constant k_B and temperature T) measured in units of $\beta_0 = E_0^{-1}$. If not indicated differently all quantities and figures in the following chapters will refer to this set of units.

If the pair-interaction is chosen to be a Coulomb interaction referring to particles of charge q_0 , then the coupling parameter reads

$$\lambda = \frac{\alpha}{x_0 \hbar\Omega} = \frac{x_0}{a_B}, \quad \alpha = \frac{q_0^2}{4\pi\epsilon_0\epsilon_b}, \quad (1.4)$$

where α is the familiar interaction strength, $a_B = 4\pi\epsilon_0\epsilon_b\hbar^2/(mq_0^2)$ is the effective Bohr radius and ϵ_b denotes any background dielectric constant. Thus, λ is just the ratio of the characteristic

Coulomb energy $E_B = \alpha/x_0$ to the confinement energy $E_0 = \hbar\Omega$. Equivalently, this ratio can be stated in terms of the typical length scales x_0 and a_B . If now $a_B \gg x_0$, i.e. in the limit $\lambda \rightarrow 0$, the noninteracting part of the Hamiltonian H_1 will dominate the system properties, while for $\lambda \rightarrow \infty$ the system is said to be in the strongly correlated regime [6]. Further, as Ω enters definition (1.4), the coupling parameter is directly controlled by the trap frequency—the weaker the confinement the larger the relative interaction strength λ .

Another remark is due to the Coulomb potential which is singular at $x_i - x_j = 0$ and (in a 1D coordinate space) leads to computational difficulties. It is, therefore, convenient to use $w(x_i, x_j) = \lambda/\sqrt{(x_i - x_j)^2 + a^2}$ instead, where the small parameter a has a screening effect and prevents the singularity¹ (see Appendix A.2.2). Only as a marginal note: In the special case of $N = 2$, such a modified interaction can also be interpreted as the two particles being situated in different layers with a parallel separation a but interacting via pure Coulomb repulsion.

Furthermore, the restriction to $\hbar \equiv 1$ in definitions or expressions other than (1.3) throughout this thesis has been found advantageous due to notational simplicity. Particularly in the Green's function theory this leads to general clarity.

A last comment concerns two frequently used notations:

- (a) The spelling $\Psi^{(\dagger)}$ with the symbol \dagger in brackets means either the operator Ψ itself or the adjoint operator Ψ^\dagger .
- (b) Bold-typed expressions, as e.g. \mathbf{A} or $\mathbf{B}(t)$, without exception indicate matrices and the operation $\mathbf{A}\mathbf{B}(t)$ is to be understood as the standard matrix multiplication, i.e. $(\mathbf{A}\mathbf{B}(t))_{ij} = \sum_k A_{ik} B_{kj}(t)$.

¹By inducing the behavior $a^{-1} - \Delta x^2/(2a^3) + \mathcal{O}(\Delta x^3)$ around $\Delta x = x_i - x_j = 0$.

2. Nonequilibrium Green's functions

Before starting with nonequilibrium Green's function (NEGF) theory and explaining the underlying quantum statistical basics in mathematical and physical detail, the first section of this chapter gives a brief summary of existing NEGF applications known in the literature. This is useful to classify the aspired goal of applying the nonequilibrium Green's function techniques to artificial atoms—interacting confined quantum systems of strongly inhomogeneous density.

After this overview, the present chapter will proceed to the quantum statistical treatment of interacting many-body systems and will introduce its main ingredient—the (nonequilibrium) Green's function $G(x_1t_1, x_2t_2)$, which appears as a thermodynamic average over field operators and in general depends on two space-time coordinates. Being defined on the so-called Schwinger/Keldysh time contour (see Sect. 2.2), the NEGF—on a natural footing—thereby extends the imaginary times known from equilibrium theory (Matsubara formalism [20]) to the real-time axis allowing the description of arbitrary nonequilibrium situations. Further, as will be shown in Sect. 2.3, most statistical and dynamical information about the quantum N -particle system is directly accessible from G .

The quantum kinetic equations (Keldysh/Kadanoff-Baym equations (KKBE) [14]) that the nonequilibrium Green's functions obey, and which are of main numerical interest later in this work, are then intensively discussed in the next chapter. For topics which go beyond the scope of this introduction and the additional informations provided in Chap. 3, the interested reader is referred to Refs. [13, 14, 17] and the references therein.

2.1. Overview

Tracing back to the (early) developments of Kadanoff and Baym [14, 21], and Keldysh [22], the nonequilibrium Green's function method has, since the 1960's, led to most rapid progress in quantum kinetics of interacting many-body systems [11, 24]. Together with important contributions from Martin and Schwinger [25], and Kubo [26], the initial work on NEGF has successfully extended the imaginary-time formalism of (equilibrium) quantum statistical mechanics first introduced by Matsubara [20] in the mid 1950's. The developed techniques allow for a field-theoretical description of quantum systems (at zero and finite temperatures) which systematically takes particle-particle correlations into account, and, in nonequilibrium, incorporates ultrafast processes on the systems' intrinsic time scales. Problems related to e.g. dissipation and memory effects have thereby been straightforwardly overcome, and, providing most statistical and dynamical information (e.g. quantum Wigner distribution [27] and complete one-particle spectrum), the NEGF has turned out to be a very useful tool in a variety of fields.

Early demonstrations of the nonequilibrium Green's function method are related to many-body theory of homogeneous Fermi and Bose gases or liquids and nuclear matter—for an overview see e.g. Refs. [17] and [11, 24, 28]. The first numerical solution of the KKBE has been performed by Danielewicz [29] who studied the equilibration of nuclear matter including high energy collisions, and the works of Köhler [30], Božek [31], Ivanov *et al.* [32] and many others concern related problems. Beyond these investigations, there have been discussions on a large amount of applications in different areas including experimental accessibility. For instance, being motivated by the pioneering work of DuBois *et al.* [33], there exist NEGF approaches to (relativistic)

non-ideal plasmas [34, 35] and plasma oscillations [36]. In particular, Semkat *et al.* [37] have numerically investigated (energy) relaxation processes in dense plasmas on sub-femtosecond scales, and non-Markovian effects in charge-carrier scattering have been studied by Bonitz *et al.* [38]. In addition, nonequilibrium Green's functions are successfully applied to optical and electronic properties in semiconductors (Henneberger *et al.* [39], Haug and Koch *et al.* [40, 41], and others) and to quantum transport phenomena (e.g. Jauho [41]). Numerically solving the Keldysh/Kadanoff-Baym equations, Binder *et al.* [42] have studied electron hole plasmas in semiconductors, and the response of valence and conduction band electron populations to arbitrarily strong external fields has been investigated by Kwong *et al.* [43]. Latest developments in optics applications are due to e.g. Gartner and Lorke *et al.* [44] the work of which focuses on the quantum kinetics of charges in semiconductor nanostructures including phonons. On a more theoretical basis, also implications of the NEGF groundwork on time-dependent density functional theory (TDDFT) have been discussed by van Leeuwen [45].

Moreover, recent research interests increasingly involve interacting many-body systems that are confined in external potentials of various geometries. Especially parabolic entrapment is often realized when investigating ions in Penning or Paul traps [1, 2], charged dust particles in plasma environments [3, 4], electrons and excitons in quantum wells and dots [5, 6] or ultra-cold atoms and molecules which are candidates for Bose-Einstein condensation (BEC) [7]. Such (quantum) confined systems, which often—apart from typical BEC systems—contain a small or mesoscopic number of particles and may appear reduced in dimensionality, serve as interesting model systems, since they allow for well conditioned investigations on both experimental and theoretical grounds. For instance, diagnostic methods give direct access to (optical) absorption spectra or existing collective modes [5, 46] which can be theoretically understood and interpreted. Particular interest is thereby due to correlation phenomena which essentially affect the quantum many-body state and—changing the system parameters (particle number, temperature, confinement and interaction strength etc.)—may lead for example to Wigner crystallization of electrons within semiconductor materials [6]. Furthermore, besides varying the confinement strength itself, the quantum properties of trapped systems can easily be controlled by applying electric and magnetic fields the latter of which also couples to spin degrees of freedom. This offers diverse applications and might, in future, lead to reliable computing devices for (quantum) information storage and processing.

Many-body systems with reduced dimensionality—for instance interacting electrons in 2D quantum well structures [47]—have already been studied with nonequilibrium Green's function techniques. But most of these systems still imply quasi-homogeneity, and there is no confinement leading to densities that vary in space. This is of course different for the harmonically trapped systems (artificial atoms) mentioned above. However, Keldysh/Kadanoff-Baym approaches to such *inhomogeneous* systems have remained widely unexplored. Only very recently, progress has been made in quantum chemistry examining atoms and molecules. Using the nonequilibrium Green's functions, N.E. Dahlen *et al.* [48] and A. Stan *et al.* [49] have computed the total energies and ionization potentials for a number of atoms and small diatomic molecules. In addition, the atomic spectral function and the nonequilibrium electron dynamics (in linear response) have been treated in Ref. [16]. Nevertheless, very little is known on NEGF applications to confined systems other than electrons in atoms or molecules. Within this scope, Indlekofer *et al.* [50] have investigated nonequilibrium electron transport in a 1D nano-transistor including a harmonically-like confinement—however, this work is mainly based on a mean-field Green's function and the influence of correlations stays practically unresolved.

For this reasons, it has been found interesting—in the present thesis—to systematically apply the nonequilibrium Green's functions to inhomogeneous quantum systems as are e.g. artificial atoms. Similar to the works mentioned above, Refs. [16, 47], it is thereby advantageous to

incorporate the finite temperature (imaginary-time) formalism and, thus, to study the system's time-evolution starting from a correlated initial state (with predefined temperature). This overcomes difficulties in many other works, see e.g. Refs. [29, 37, 43, 51], where the system first needs to equilibrate from a many-body state which is not in thermodynamic equilibrium and, consequently, does not allow one to control the temperature.

2.2. Nonequilibrium Green's functions. Definitions and properties

In principle, all interacting quantum (and classical) many-body systems in equilibrium and nonequilibrium are completely described by a sufficiently large set of N -particle wave functions $|\Psi_{N,i}\rangle \equiv \Psi_{N,i}(q_1 \dots q_N, t)$ entering the time-dependent Schrödinger equation (TDSE) as $i \partial_t |\Psi_{N,i}\rangle = H(t) |\Psi_{N,i}\rangle$, where $\{q_i\}$ denotes a complete set of observables—e.g. space and spin variables $q_i \equiv x_i \sigma_i$. The associated Hamiltonian in coordinate representation thereby attains the form

$$H(t) = \sum_{i=1}^N h^0(x_i, t) + \sum_{i<j} w(x - x'), \quad h^0(x_i, t) = -\frac{\nabla_{x_i}^2}{2m} + v(x_i, t), \quad (2.1)$$

where $h^0(x_i, t)$ denotes the one-particle contributions containing kinetic energy and a (generally time-dependent) potential $v(x_i, t)$. Further, $w(x_i - x_j)$ is a specific pair-interaction potential added up over all $N(N - 1)/2$ classically distinguishable pairs $\{x_1, x_j\}$ and, for simplicity, spin degrees of freedom have been neglected.

However, if the number of particles approaches a mesoscopic or even macroscopic ($N \propto 10^{23}$) integral number, it becomes impossible to exactly solve the TDSE and even its stationary equivalent does not allow for an exact solution. In addition, the wave function $|\Psi_{N,i}\rangle$ has to fulfill the correct symmetry, i.e. must be (anti-)symmetric under particle exchange for bosons of zero or integer spin (fermions of odd half-integer spin). While it is simple to construct the (anti-)symmetric wave function in a few-particle system with $N \lesssim 3$, this becomes an intricate task for larger N , and in general one has to call on group theoretical considerations. Moreover, it is not trivial to incorporate thermodynamic situations where the interacting many-body system is connected to a given bath of finite temperature $k_B T = \beta^{-1}$ and, therefore, requires a respective statistical treatment.

Thus, apart from *first principle* approaches based on microscopic footings (see e.g. Ref. [13] or Sect. 5.4), it is more fruitful to proceed with a quantum field theoretical description. Using the second quantization language such a method equally applies to Fermi and Bose systems and, in particular, allows one to overcome the problem of (anti-)symmetrizing the wave functions as symmetry properties and spin statistics are automatically included and preserved. Furthermore, in combination with quantum statistics, ensemble averages become available at finite temperatures, which offers a profound basis to establish the (non)equilibrium Green's functions.

Acting within the abstract Fock space [52], which combines Hilbert spaces corresponding to different particle numbers N , the natural quantities to be handled in quantum statistical mechanics are fermionic or bosonic field operators $\Psi^{(\dagger)}(x)$ — $x \in \mathbb{R}^d$, where d indicates the dimensionality of the system. In the Heisenberg representation, they depend on both space and time coordinates, i.e. $\Psi^{(\dagger)}(x_1) \rightarrow \Psi_H^{(\dagger)}(1) = \Psi_H^{(\dagger)}(x_1 t_1)$, where conventionally one writes $1 \equiv x_1 t_1$ indicating simultaneously a coordinate in space and a particular point in time. Physically, the creation operator $\Psi_H^\dagger(1)$, when acting to the right on a state, adds a particle to this state at the space-time point $1 = x_1 t_1$ —the annihilation (adjoint) operator $\Psi_H(1)$, acting to the right, removes a particle from the state at point 1. Exactly in this sense the system description in terms of field operators also gives access to ionization and transport processes. Further, the

correct particle statistics is complied via commutation relations at equal times ($t_{1,2} = t$), i.e.

$$\left[\Psi_H(x_1 t), \Psi_H^\dagger(x_2 t) \right]_{\mp} = \delta(x_1 - x_2), \quad (2.2)$$

$$\left[\Psi_H^{(\dagger)}(x_1 t), \Psi_H^{(\dagger)}(x_2 t) \right]_{\mp} = 0, \quad (2.3)$$

where the upper sign—here and in most subsequent expressions—refers to bosons (commutator) and the lower one refers to fermions (anti-commutator), $\mp \equiv (b/f)$. Within the Heisenberg picture the many-body Hamiltonian, Eq. (2.1), can then be rewritten in the second-quantized form

$$\begin{aligned} H_H(t) &= \int dx \Psi_H^\dagger(xt) h^0(x, t) \Psi_H(xt) \\ &+ \iint dx dx' \Psi_H^\dagger(xt) \Psi_H^\dagger(x't) w(x - x') \Psi_H(x't) \Psi_H(xt), \end{aligned} \quad (2.4)$$

where now the total particle number $N(t_1) = \int dx_1 \Psi_H^\dagger(1) \Psi_H(1)$ is not necessarily fixed. Notice that the ordering of the last two operators in the interaction energy ensures that $H_H(t)$ is hermitian.

Next, it is important to know how expectation values can be calculated at finite temperatures, and how they change in time when the many-body system is affected by a time-dependent disturbance leading to deviations of the system properties from equilibrium. To this end, assume the system to be initially, at times $t < t_0$, in thermodynamic equilibrium corresponding to the time-independent Hamiltonian H_0 —Eq. (2.4) evaluated at t_0 in the Schrödinger picture. Performing grand canonical ensemble calculations, it is further useful to subtract the chemical potential μ from the quantity $h^0(x)$ entering the Hamiltonian, thus replacing $h^0(x) \rightarrow h^0(x) - \mu$. The expectation value of an observable O at a given time point $t \geq t_0$ is then accessible through the trace with the grand canonical density operator¹ ρ , i.e.

$$\langle O(t) \rangle = \text{Tr}\{\rho O_H(t)\}, \quad \rho = \frac{e^{-\beta H_0}}{\text{Tr}\{e^{-\beta H_0}\}}. \quad (2.5)$$

where the operator $O_H(t)$ is in the Heisenberg picture, $O_H(t) = U(t_0, t) O U(t, t_0)$, and the time-evolution operator U is defined by

$$U(t, t_0) = e^{-i \int_{t_0}^t d\bar{t} H(\bar{t})}. \quad (2.6)$$

From Eq. (2.6), one in particular finds that

$$U(t_0 - i\beta, t_0) = e^{-\beta H_0}, \quad (2.7)$$

i.e. the operator $e^{-\beta H_0}$ can be directly identified as an evolution operator U in imaginary time which, more precisely, propagates the system from the initial time t_0 parallel to the imaginary axis to $t_0 - i\beta$. Further, this allows to refine expression (2.5) for the time-dependent expectation values. Inserting definition (2.7) leads to the formula

$$\langle O(t) \rangle = \frac{\text{Tr}\{U(t_0 - i\beta, t_0) U(t_0, t) O U(t, t_0)\}}{\text{Tr}\{U(t_0 - i\beta, t_0)\}}. \quad (2.8)$$

While the denominator is just the grand canonical partition function expressed by U , the numerator of Eq. (2.8) gives rise to the following interpretation: Reading the time-arguments from

¹The density operator ρ is hermitian, positive definite and satisfies $\text{Tr}\{\rho\} \equiv 1$.

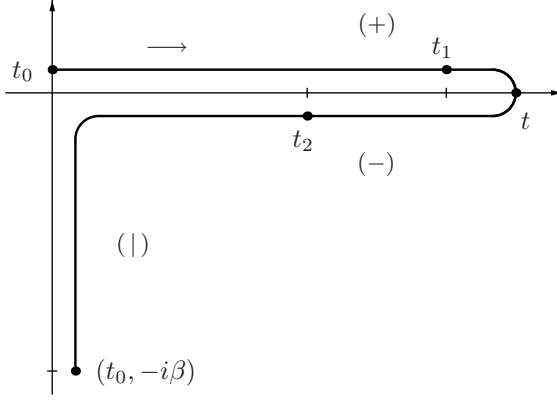


Figure 2.1: Schwinger/Keldysh-contour \mathcal{C} in the imaginary time plane, $\mathcal{C} = \{t \in \mathbb{C} \mid \Re t \in [t_0, \infty], \Im t \in [t_0, -\beta]\}$. For more clarity the different contour branches are displayed slightly off the axes. Time-ordering: Time t_2 is later on the contour than time t , and t is later than t_1 . The distinguishable subordinated Green's functions $G^*(1, 2)$ with $* \equiv \{M, \gtrsim, \rceil/\lceil\}$ —defined in Sect. 2.2.1—are either defined on the imaginary axis ($* = M$), on the real axis ($* = \gtrsim$) or on both ($* = \rceil/\lceil$). Symbols in brackets are explained in Sect. 2.2.2.

right to left, one may say that the system first evolves along the real chronological time axis from t_0 to time t at which the operator O acts. Then the system anti-chronologically evolves back along this axis from time t to t_0 and finally gets propagated parallel to the imaginary axis from t_0 to $t_0 - i\beta$. Graphically, this leads to the time contour $\mathcal{C}(t) = \{\bar{t} \in \mathbb{C} \mid \Re \bar{t} \in [t_0, t], \Im \bar{t} \in [t_0, -\beta]\}$ in the imaginary time plane which originally has been introduced by Keldysh [22] and is referred to as the Schwinger/Keldysh-contour—see Fig. 2.1. The imaginary branch of this contour then in particular accounts for the ensemble averaging at the given temperature β .

A more general expression for all time-dependent expectation values is consequently

$$\langle O(t) \rangle = \frac{\text{Tr}\{T_{\mathcal{C}}[\exp(-i \int_{\mathcal{C}} d\bar{t} H(\bar{t})) O(t)]\}}{\text{Tr}\{U(t_0 - i\beta, t_0)\}}, \quad (2.9)$$

where the exponential function is to be understood similarly to Eq. (2.6) as Dyson series [52], and $T_{\mathcal{C}}$ is now the contour time-ordering operator defined by

$$T_{\mathcal{C}}(O_1(t_1) \dots O_s(t_s)) = \sum_{\sigma \in \mathcal{P}_s} (\pm)^{I(\sigma)} \prod_{j=1}^{s-1} \theta(t_{\sigma_j}, t_{\sigma_{j+1}}) \prod_{k=1}^s O_{\sigma_k}(t_{\sigma_k}), \quad (2.10)$$

where later operators are moved to the left, and each exchange of a fermionic operator is accompanied by a minus sign, i.e. $I(\sigma)$ gives the number of inversions in the permutation σ . Furthermore, $\theta(t_1, t_2) = 1$ if t_1 is situated later on the contour than t_2 and 0 otherwise—see Fig. 2.1 for explanation. Note, that in Eq. (2.9) the operators $H(\bar{t})$ and $O(t)$ are independent of the particle species and, thus, $I(\sigma) \equiv 0 \forall \sigma \in \mathcal{P}_s$.

With the definitions and considerations above one is now ready to move on to the definition of the (non)equilibrium Green's functions. As the thermodynamic average over the contour-ordered product of an annihilation and a creation field operator being in the Heisenberg representation, the **one-particle Green's function** $G(1, 2) = G(x_1 t_1, x_2 t_2)$ is defined by

$$\begin{aligned} G(1, 2) &= -i \left\langle T_{\mathcal{C}} \left[\Psi_H(1) \Psi_H^\dagger(2) \right] \right\rangle \\ &= \frac{1}{i} \frac{\text{Tr}\left\{U(t_0 - i\beta, t_0) T_{\mathcal{C}} \left[\Psi_H(1) \Psi_H^\dagger(2) \right]\right\}}{\text{Tr}\{U(t_0 - i\beta, t_0)\}}, \end{aligned} \quad (2.11)$$

and, thus, occurs as a two-time generalization of the reduced (one-particle) density matrix $F_1(t)$ in coordinate representation [12]. This can be reobtained in the limit of equal times, i.e.

$$\langle x_1 | F_1(t) | x_2 \rangle = \left\langle \Psi^\dagger(x_1 t) \Psi(x_2 t) \right\rangle = -i G(x_1 t, x_2 t^+), \quad (2.12)$$

where, notationally, t^+ indicates that the limit $t \rightarrow t + 0$ is taken from above on the Keldysh-contour. Via the correlation functions, cf. Eqs. (2.18) and (2.44), the Green's function can additionally be related to the *Wigner function* $f(p, R, T)$ [27], which in principle agrees with the spatially resolved occupation probabilities of the momentum states realized in the considered many-body system (see Refs. [12, 13]), and allows for a direct computation of all one-particle observables $\langle O(t) \rangle$, see Sect. 2.3. In the case of thermodynamic equilibrium, the Green's function $G(1, 2)$ moreover includes the imaginary-time formalism for quantum statistical mechanics which dates back to Matsubara [20], see Sect. 2.2.1 and Sect. 3.3.3.

Going beyond the one-particle level of definition (2.11), the generalization to s -particle Green's functions is straightforward. Conveniently, one defines

$$G_{1\dots s}(1\dots s, 1'\dots s') = (-i)^s \left\langle T_{\mathcal{C}} \left[\Psi_H(1) \dots \Psi_H(s) \Psi_H^\dagger(s') \dots \Psi_H^\dagger(1') \right] \right\rangle, \quad (2.13)$$

where corresponding to Eq. (2.12) one may connect $G_{1\dots s}$ to an s -particle density operator $F_{1\dots s}(t)$, from which practically each s -particle observable is computable [13]. Later—mainly in Chap. 3—one has to account for the two-particle case with

$$G_{12}(12, 1'2') = (-i)^2 \left\langle T_{\mathcal{C}} \left[\Psi_H(1) \Psi_H(2) \Psi_H^\dagger(2') \Psi_H^\dagger(1') \right] \right\rangle. \quad (2.14)$$

Moreover, for all Green's functions there exist equations of motions—the Keldysh/Kadanoff-Baym equations. To study them is subject of Chap. 3.

2.2.1. Subordinated quantities

The analysis of the Schwinger/Keldysh-contour (Fig. 2.1) with respect to the definition of the time-ordered (one-particle) Green's function reveals, that one can distinguish different *subordinated* functions which depend on time-arguments that are differently positioned on the contour. Due to three existing branches one therefore may comprehend $G(1, 2)$ as a 3×3 matrix, constructed from the following two-time functions:

- i. **Matsubara Green's function**, $G^M(1, 2)$.

With restriction to the imaginary part of the contour ($\tau_{1,2} \in \Im \mathcal{C}$), one defines

$$G^M(x_1\tau_1, x_2\tau_2) = G(x_1t_0 - i\tau_1, x_2t_0 - i\tau_2). \quad (2.15)$$

- ii. **Correlation functions**, $G^{\gtrless}(1, 2)$.

As the Green's function can be rewritten in the form

$$G(1, 2) = \theta(t_1, t_2) G^>(1, 2) - \theta(t_2, t_1) G^<(1, 2), \quad (2.16)$$

one needs the greater and lesser correlation functions ($\pm \equiv (b/f)$)

$$G^>(1, 2) = (1/i) \left\langle \Psi_H(1) \Psi_H^\dagger(2) \right\rangle, \quad (2.17)$$

$$G^<(1, 2) = \pm(1/i) \left\langle \Psi_H^\dagger(2) \Psi_H(1) \right\rangle. \quad (2.18)$$

According to the opposite arrangement of the field operators in Eqs. (2.17) and (2.18), the quantity $G^>(1, 2)$ can be interpreted as the propagation of an added particle—the quantity $G^<(1, 2)$ describes the propagation of a removed particle or *hole* [17]. Further, the correlation functions are connected via the symmetry relations

$$G^{\gtrless}(1, 2) = - \left[G^{\gtrless}(2, 1) \right]^*, \quad (2.19)$$

$$G^>(x_1t, x_2t) = -i\delta(x_1 - x_2) + G^<(x_1t, x_2t). \quad (2.20)$$

iii. **Mixed functions**, $G^{\lceil/\rceil}(1, 2)$.

If $t_{1,2} \in \Re \mathcal{C}$ and $\tau_{1,2} \in \Im \mathcal{C}$, one defines

$$G^{\lceil}(x_1 t_1, x_2 \tau_2) = G^<(x_1 t_1, x_2 t_0 - i \tau_2), \quad (2.21)$$

$$G^{\rceil}(x_1 \tau_1, x_2 t_2) = G^>(x_1 t_0 - i \tau_1, x_2 t_2). \quad (2.22)$$

The notation is thereby quite suggestive when one reads both symbols, \lceil and \rceil , from left to right—compare with the appearance of the contour \mathcal{C} .

Some remarks: (a) In definitions (2.15) and (2.21-2.22) one may, without loss of generality, assume $t_0 \equiv 0$, since any initial (equilibrium) state can formally be translated in time. (b) Notice that, later in this work, one comprehends notations as e.g. $G^{\lceil}(-i \tau_1, t)$ and $G^{\rceil}(\tau_1, t)$ as fully equivalent. (c) According to definition (2.13) one may extend all subordinated quantities also to s -particle levels obtaining the functions $G_{1\dots s}^*(1\dots s, 1'\dots s')$ with $*$ $\equiv \{M, \gtrsim, \lceil/\rceil\}$.

2.2.2. Contour calculus

Besides the different types of single-particle Green's functions introduced by Eqs. (2.15), (2.17-2.18) and (2.21-2.22), i.e. $G^*(1, 2)$ with $*$ $\equiv \{M, \gtrsim, \lceil/\rceil\}$, one may also distinguish certain combinations of them. For instance—concerning the lesser and greater correlation functions—there exist the causal and anti-causal Green's functions, defined by

$$G^{c/a}(1, 2) = \theta(\pm[t_1 - t_2]) G^>(1, 2) + \theta(\pm[t_2 - t_1]) G^<(1, 2), \quad (2.23)$$

and, moreover, one has the retarded and advanced Green's functions

$$G^{R/A}(1, 2) = \pm \theta(\pm[t_1 - t_2]) [G^>(1, 2) - G^<(1, 2)], \quad (2.24)$$

with $\theta(t_1 - t_2)$ being the standard Heaviside step function. Notice that in Eqs. (2.23) and (2.24) the signs do not belong to different particle species but solely distinguish the quantities G^c and G^a as well as G^R and G^A , respectively. Further, one finds the relations

$$G^R = G^c - G^< = G^> - G^a, \quad G^A = G^c - G^> = G^< - G^a, \quad (2.25)$$

$$G^R - G^A = G^> - G^<, \quad G^R + G^A = G^c - G^a. \quad (2.26)$$

As one will see in Sect. 2.3, the retarded and advanced Green's functions in particular carry the dynamical information of the many-body system and, thus, are closely connected to the spectral function which describes the (un)correlated one-particle spectrum, cf. Eq. (2.40). However, from the six functions G^{\gtrsim} , $G^{c/a}$ and $G^{R/A}$ there are, in nonequilibrium, only two independent.²

As mentioned in Sect. 2.2.1, the general Green's function on the one-particle level can equally be understood as a 3×3 matrix containing the subordinated functions $G^{M, \gtrsim, \lceil/\rceil}(1, 2)$. In order to clearly define such a *Keldysh matrix* [13], it is thereby useful to review the arrangement of times on the contour \mathcal{C} . As it can be extracted from Fig. 2.1, the Keldysh-contour generally allows one to specify if any real time-argument is located on the chronological (+) or anti-chronological (−) branch. Together with the occurrence of imaginary times, symbolically denoted as (\lceil), one then may define matrix elements $G^{\alpha\beta}$ with respective superscripts $\alpha, \beta \in \Lambda = \{+, -, \lceil\}$. Collecting them into a matrix $\mathbf{G}_\Lambda(t_1, t_2)$ yields

$$\mathbf{G}_\Lambda(t_1, t_2) = \left(\begin{array}{cc|c} G^{++} & G^{+-} & G^{+\lceil} \\ G^{-+} & G^{--} & G^{-\lceil} \\ \hline G^{\lceil+} & G^{\lceil-} & G^{\lceil\lceil} \end{array} \right) = \left(\begin{array}{cc|c} G^c & G^< & G^{\lceil} \\ G^> & G^a & G^{\lceil} \\ \hline G^{\lceil} & G^{\lceil} & G^M \end{array} \right), \quad (2.27)$$

²In thermodynamic equilibrium, there is only a single independent function which in particular may be reconstructed from the Matsubara Green's function at imaginary times [53].

where $t_{1,2} \in \mathcal{C}$, and with the last equality one has identified the different matrix elements with the available subordinated Green's functions. For notational simplicity spatial coordinates have been neglected. The upper-left square matrix in Eq. (2.27) contains the real-time quantities and the lower-right corner the Matsubara Green's function at imaginary times—the rectangular matrices in between are linking both contour branches via the mixed functions.

In fact, the matrix $\mathbf{G}_\Lambda(t_1, t_2)$ offers a very compact notation for the Green's function. Moreover, operating with different matrices allows for a systematical treatment of the circumstance that all subordinated Green's functions are defined with respect to different contour branches. Computations are therefore essentially simplified. For instance, the performance of contour integrals over the product of two functions \mathbf{A}_Λ and \mathbf{B}_Λ , both defined on \mathcal{C} , then obeys rules of matrix multiplication, i.e.

$$\mathbf{C}_\Lambda(t_1, t_2) = \int_{\mathcal{C}} d\bar{t} \mathbf{A}_\Lambda(t_1, \bar{t}) \bullet \mathbf{B}_\Lambda(\bar{t}, t_2) = \left(\begin{array}{cc|c} C^{++} & C^{+-} & C^{+|} \\ C^{-+} & C^{--} & C^{-|} \\ \hline C^{|+} & C^{|-} & C^{||} \end{array} \right), \quad (2.28)$$

where the various matrix elements entering the quantity $\mathbf{C}_\Lambda(t_1, t_2)$ are given by³

$$C^{\alpha\beta}(t_1, t_2) = \sum_{\gamma=+,-} \gamma \left[A^{\alpha\gamma} \circ B^{\gamma\beta} \right](t_1, t_2) + \left[A^{|\alpha} \star B^{|\beta} \right](t_1, t_2), \quad (2.29)$$

and the operations \circ and \star are defined through integrals over the Keldysh-contour ($\alpha, \beta \in \Lambda$ and $\gamma \in \{+, -\}$):

$$\left[A^{\alpha\gamma} \circ B^{\gamma\beta} \right](t_1, t_2) = \int_{t_0}^{\infty} d\bar{t} A^{\alpha\gamma}(t_1, \bar{t}) B^{\gamma\beta}(\bar{t}, t_2), \quad (2.30)$$

$$\begin{aligned} \left[A^{|\alpha} \star B^{|\beta} \right](t_1, t_2) &= \int_{t_0}^{t_0 - i\beta} d\bar{t} A^{|\alpha}(t_1, \bar{t}) B^{|\beta}(\bar{t}, t_2) \\ &= -i \int_0^\beta d\bar{\tau} A^{|\alpha}(t_1, t_0 - i\bar{\tau}) B^{|\beta}(t_0 - i\bar{\tau}, t_2). \end{aligned} \quad (2.31)$$

In addition, one may need to evaluate delta functions on the contour. Acting according to

$$\mathbf{A}_\Lambda(t_1, t_2) = \int_{\mathcal{C}} d\bar{t} \delta_\Lambda(t_1 - \bar{t}) \bullet \mathbf{A}_\Lambda(\bar{t}, t_2), \quad (2.32)$$

there consequently occur the matrix elements $\delta_\Lambda^{\alpha\beta}(t_1, t_2) = \delta_{\mathcal{C}}(t_1 - t_2) \delta_{\alpha\beta}$, with $\alpha, \beta \in \Lambda$ and $\delta_{\mathcal{C}}(t_1 - t_2)$ being defined on \mathcal{C} .

2.3. Determination of macroscopic observables

As a far-reaching generalization of usual (single-time) density matrices, the Green's functions contain a wealth of information—both statistical *and* dynamical. In this context, the functions $G^{\cong}(1, 2)$, and exclusively $G^M(1, 2)$ in the case of thermodynamic equilibrium, are most closely related to the macrophysical properties. However, one is limited to a sub-class of expectation values since, generally, two-particle observables as e.g. the pair distribution function require information from $G_{12}(12, 1'2')$ which is essentially more involved to compute, see Chap. 3.

³The notational result (2.28,2.29) is due to M. Bonitz.

From the relation of the Green's function to the reduced density matrix $F_1(t)$ —cf. Eq. (2.12)—it follows directly that expectation values $\langle O(t_1) \rangle$ of one-body operators $o(x_1, t_1)$ are generally given by

$$\begin{aligned} \langle O(t_1) \rangle &= \int dx_1 \left\{ o(x_2, t_1) \left\langle \Psi_H^\dagger(x_1 t_1) \Psi_H(x_2 t_1) \right\rangle \right\}_{x_2=x_1} \\ &= \pm i \int dx_1 \left\{ o(x_2, t_1) G^<(x_1 t_1, x_2 t_1) \right\}_{x_2=x_1} , \end{aligned} \quad (2.33)$$

where after the action of $o(x_2, t_1)$ one equates both spatial coordinates, and as before mentioned the notation means $\mp \equiv (\text{b/f})$. In the case of thermodynamic equilibrium, at time t_0 , one further can replace the correlation function $G^<$ by the limit $\lim_{\tau_1 - \tau_2 \rightarrow 0^-} G^M(x_1 \tau_1, x_2 \tau_2)$ of the Matsubara Green's function.

The average density $\langle n(1) \rangle$ at a space-time point $1 \equiv x_1 t_1$ and the mean particle number $\langle N(t_1) \rangle$ are then quite simple:

$$\langle n(1) \rangle = -i G(1, 1^+) = \pm i G^<(x_1 t_1, x_1 t_1) , \quad (2.34)$$

$$\langle N(t_1) \rangle = \pm i \int dx_1 G(1, 1^+) . \quad (2.35)$$

Further, the current density $\langle \mathbf{j}(1) \rangle$ is accessible through

$$\langle \mathbf{j}(1) \rangle = \pm i \left\{ \frac{\nabla_{x_1} - \nabla_{x_2}}{2im} G^<(x_1 t_1, x_2 t_1) \right\}_{x_1=x_2} , \quad (2.36)$$

and is of course linked to the temporal change of the density by the *continuity equation*, i.e.

$$\partial_{t_1} \langle n(1) \rangle + \text{div} \langle \mathbf{j}(1) \rangle = 0 . \quad (2.37)$$

As such macroscopic conservation laws allow for a systematical analysis of the temporal behavior of the Fermi or Bose system, another important quantity is the time-dependent total energy. In terms of the one-particle Green's function (despite the fact that the interaction part of the total energy involves a two-particle operator) it can be derived [54] that

$$\langle \langle (H - \mu N)(t_1) \rangle \rangle = \pm i \int dx_1 \left\{ \frac{1}{2} (i \partial_{t_1} + h^0(1) - 2\mu) G(1, 2) \right\}_{2=1} \quad (2.38)$$

$$\begin{aligned} &= \pm i \int dx_1 \left\{ h^0(1) G(1, x_2 t_1^+) \right\}_{x_2=x_1} \pm i \iint_C dx_1 d3 \Sigma(1, 3) G(3, 2^+) \\ &\quad - \mu \langle N(t_1) \rangle , \end{aligned} \quad (2.39)$$

where μ is the chemical potential originating from the grand canonical treatment, and for explanation of the one-particle quantity or *self-energy* $\Sigma(1, 2)$ the reader is referred to Chap. 3, Sect. 3.1. In Eq. (2.39), the first term describes the single-particle energy (i.e. kinetic plus potential energy) and the second term determines the interaction energy. In equilibrium, especially the contour integral simplifies leading to an integration over the imaginary axis only—see Sect. 4.3.2 and compare also with Dahlen *et al.* [15].

But G contains even more information. For instance, the correlation functions G^{\gtrless} give direct access to the (un)correlated single-particle spectrum. This dynamical information is stored in the so-called *spectral function* defined by

$$\begin{aligned} A(1, 2) &= i [G^>(1, 2) - G^<(1, 2)] \\ &= \begin{cases} i G^R(1, 2) & , \quad t_1 \geq t_2 \\ -i G^A(1, 2) & , \quad t_1 < t_2 \end{cases} . \end{aligned} \quad (2.40)$$

2. Nonequilibrium Green's functions

To make the spectral content more obvious—it is convenient to rewrite the Green's function in terms of center of mass (COM) and relative coordinates, i.e. separating the scales (r, t) and (R, T) by

$$R = \frac{x_1 + x_2}{2} \quad , \quad r = x_1 - x_2 \quad , \quad (2.41)$$

$$T = \frac{t_1 + t_2}{2} \quad , \quad t = t_1 - t_2 \quad . \quad (2.42)$$

Performing, in addition, Fourier transforms with respect to both relative coordinates (r, t) , one arrives at

$$A(p, \omega; R, T) = i \int \frac{d\omega}{2\pi} \int dt e^{-ipr+i\omega t} [G^>(r, t; R, T) - G^<(r, t; R, T)] \quad . \quad (2.43)$$

In this form, the spectral function gives—for a particle located at the space-time point (R, T) with fixed momentum p —the occupation probability $A(\omega)$ of states with energy ω . Further, integrating Eq. (2.43) over the whole coordinate space and over all momenta one obtains the time-dependent density of states [41], i.e. $\rho^{\text{DOS}}(\omega, T) = \frac{1}{(2\pi)^d} \int dp \int dR A(p, \omega; R, T) \equiv -\frac{1}{\pi} \Im \text{Tr} \{g^R(p, \omega; R, T)\}$ with d being the dimension of the coordinate space.

Alternatively to Eq. (2.33), all macroscopic one-particle observables can equally be obtained from the Wigner distribution function, $f(p, R, T)$. Containing the complete statistical information offered by G , it is

$$f(p, R, T) = \int dr e^{-ipr} \left\langle \Psi_H^\dagger(R - r/2, T) \Psi_H(R + r/2, T) \right\rangle \quad (2.44)$$

$$\begin{aligned} &= \int \frac{d\omega}{2\pi} \int dr \int dt e^{-ipr+i\omega t} [\pm i G^<(r, t; R, T)] \\ &= \pm i \int \frac{d\omega}{2\pi} G^<(p, \omega; R, T) \quad , \end{aligned} \quad (2.45)$$

where in (2.44) the average $\langle \Psi_H^\dagger \Psi_H \rangle$ denotes the density operator $F_1(T)$ in relative and COM coordinates. For instance, integrating the Wigner function $f(p, x_1, t_1)$ over all momenta gives the spatial density, $\langle n(1) \rangle = \int \frac{dp}{(2\pi)^d} f(p, x_1, t_1)$, and further including the statistical weight p/m leads to the current density, $\langle \mathbf{j}(1) \rangle = \int \frac{dp}{(2\pi)^d} \frac{p}{m} f(p, x_1, t_1)$. In both expressions the integer number d denotes the dimensionality of the considered quantum system.

For discussion of other thermodynamic functions in the grand canonical ensemble, e.g. pressure or the partition function $Z_N^{\text{GCE}}(\beta, \mu)$ and their relation to the nonequilibrium Green's function, see e.g. Refs. [14, 54].

3. Keldysh/Kadanoff-Baym equations. Basis representation

In this chapter, the general equations of motion for the Green's function—the Keldysh/Kadanoff-Baym equations (KKBE) [14, 22]—are to be presented together with their closed (or self-consistent) form originating from many-body approximations and fully determining the one-particle Green's function $G(1, 2)$ in equilibrium and nonequilibrium.

The KKBE thereby appear as a far-reaching generalization of standard single-time kinetic equations. In contrast to such Boltzmann type equations [12] the KKBE are not limited by any characteristic time-scales. Due to their two-time structure, they are also applicable to describe ultrafast processes as e.g. particle dynamics or transport on femtosecond scales (or even below) as found in electronic structures. When including correlation effects, the memory kernels appearing as collision integrals on the right hand sides of the KKBE further account for a non-Markovian behavior of the system—see Sect. 3.1. In addition, the Keldysh/Kadanoff-Baym equations allow one to systematically include conserving many-body approximations [21] leading to preservation of total energy, total momentum and fulfillment of the continuity equation which are indispensable demands on the description of the quantum many-body system. Exactly in this context, the Boltzmann type equations mentioned above are substantially limited.

Moreover, the main subject of the present chapter is to go beyond the general form of the equations of motion and to work out a respective basis representation which makes the KKBE well applicable to inhomogeneous systems and offers a straightforward numerical strategy of attack. Hence, after the discussion of the Keldysh/Kadanoff-Baym equations in their standard form [14] in the first section of this chapter, Sect. 3.2 will—being motivated by Ref. [15]—focus on the representation of the Green's function in terms of spatial single-particle wave functions. With $G(1, 2)$ being expanded in such a way the derivation of equations of motion is then reviewed in Sect. 3.3 leading to the KKBE in form of a set of matrix equations whereby all advantageous properties of the usual Keldysh/Kadanoff-Baym equations are preserved and equilibrium initial correlations are systematically included by first solving the Dyson equation at finite temperatures—see Sect. 3.3.3. In total, this chapter thus gives the theoretical foundations required to set up the numerical procedure for the (thermodynamic) equilibrium and nonequilibrium solution of the KKBE as it will be described in detail in the next chapter.

Bear in mind, that although all numerical results to be shown in Chap. 5 and 6 are restricted to fermions, the equations and derivations given here are generally valid for both particle species, i.e. for fermions *and* bosons.

3.1. Keldysh/Kadanoff-Baym equations (KKBE)

Following from the equations of motion for the field operators $\Psi_H^{(\dagger)}(1) \equiv \Psi_H^{(\dagger)}(x_1 t_1)$ in the Heisenberg picture, i.e. derivable from the *Heisenberg equation* with the full Hamiltonian $H_H(t)$ in second quantization (remember Eq. (2.4)),

$$\partial_t \Psi_H^{(\dagger)}(1) = \frac{1}{i} \left[\Psi_H^{(\dagger)}(1), H_H(t) \right]_-, \quad (3.1)$$

the Green's functions are found to obey the Keldysh/Kadanoff-Baym equations (KKBE) [13, 14]:

$$(i \partial_{t_1} - h^0(1)) G(1, 2) = \pm i \int_{\mathcal{C}} d3 W(1-3) G_{12}(13; 23^+) + \delta_{\mathcal{C}}(1-2), \quad (3.2)$$

$$(-i \partial_{t_2} - h^0(2)) G(1, 2) = \pm i \int_{\mathcal{C}} d3 W(2-3) G_{12}(13; 23^+) + \delta_{\mathcal{C}}(1-2). \quad (3.3)$$

The upper signs thereby refer to bosons and the lower ones to fermions, and, as before, it is $1 \equiv (x_1 t_1)$. Furthermore, one has to explain:

- i. The equations of motion for G appear as a coupled pair of first order integro-differential equations in the time-arguments t_1 and t_2 , whereby the second equation, Eq. (3.3), is the adjoint equation with the space-time variables interchanged.
- ii. The quantity $h^0(1)$ denotes the single-particle Hamiltonian as contained in Eq. (2.4).
- iii. The integral $\int_{\mathcal{C}} d3 \equiv \int_{\mathcal{C}} \int dt_3 dx_3$ simultaneously indicates integration over the whole coordinate space and over the full time-contour \mathcal{C} .
- iv. The generalized pair-interaction potential $W(1-2)$ is to be understood as local on the Keldysh-contour, i.e. $W(1-2) \equiv w(x_1 - x_2) \delta_{\mathcal{C}}(t_1 - t_2)$, where $w(x_1 - x_2)$ denotes the usual pair-interaction potential as it enters Eq. (2.4), and the delta function is defined on the contour. Correspondingly, it is $\delta_{\mathcal{C}}(1-2) \equiv \delta(x_1 - x_2) \delta_{\mathcal{C}}(t_1 - t_2)$.
- v. As introduced in Chap. 2 the notation 3^+ means that the limit $t \rightarrow t_3 + 0$ is taken from above on the contour.
- vi. Under the (collision) integrals on the right hand sides of the KKBE, the two-particle Green's function $G_{12}(13; 23^+)$ indicates that the equations for $G(1, 2)$ are not closed but couple to higher orders. Moreover, one can show [34] that an equation determining the n -particle Green's function generally requires information from a $n \pm 1$ -particle Green's function—the particular structure for $n = 2$ is given e.g. in Ref. [13].

Thus, Eqs. (3.2) and (3.3) are only the first equations of an entire hierarchy—the so-called Martin-Schwinger (MS) hierarchy [25]—of equations of motion. The simultaneous solution of all equations to all orders would then be equivalent to exactly solving the N -particle problem. However, this is not possible in a (quantum or classical) many-body system, so that it is necessary to truncate the MS hierarchy. This is discussed below.

- vii. The integro-differential equations (3.2) and (3.3) for $G(1, 2)$ must be supplied with boundary and initial conditions. These are summarized in the Kubo-Martin-Schwinger (KMS) conditions [26, 14]

$$G(x_1 t_0, 2) = \pm G(x_1 t_0 - i\beta, 2), \quad (3.4)$$

$$G(1, x_2 t_0) = \pm G(1, x_2 t_0 - i\beta), \quad (3.5)$$

which easily follow from considering the one-particle Green's function (2.11) at $t_{1,2} = t_0 - i\beta$ and using the cyclic property of the trace ($\text{Tr}\{ABC\} = \text{Tr}\{BCA\} = \text{Tr}\{CAB\}$). For details concerning the equilibrium state given by the Green's function $G^M(1, 2)$ see Sect. 3.3.3, and for the nonequilibrium quantities $G^{\gtrless, \rceil/\lceil}(1, 2)$, it is referred to Sect. 4.5.

The set of Eqs. (3.2) and (3.3) is not directly solvable, and due to the involved mathematical structure of the Martin-Schwinger hierarchy (see point (vi)) an approximate treatment of the interaction $W(1-2)$ cannot be avoided. A natural way of truncating the hierarchy is thereby to

express the two-particle Green's function G_{12} as a functional of one-particle Green's functions. If such an approximation leads to acceptable macroscopic observables, the approximation is generally said to be adequate.

However, an additional and important demand on a specific approximation is not to violate macrophysical conservation laws as e.g. total energy and total momentum preservation or the satisfaction of the continuity equation (2.37) of Sect. 2.3. Thus, approximate expressions for G_{12} need to be properly chosen whereby, consequently, one is restricted to a special sub-class of so-called *conserving approximations* for many-body systems. Moreover, it is possible to present two criteria first formulated by Kadanoff and Baym [21], which precisely give the conditions under which no violation of conservation laws occurs. In this sense, all conservation laws are fulfilled when

- (A) the approximate single-particle Green's function $G(1, 2)$ satisfies the general equations of motions, i.e. Eq. (3.2) and (3.3).
- (B) The approximation for G_{12} satisfies the symmetry condition

$$G_{12}(12, 1^+ 2^+) = G_{12}(21, 2^+ 1^+) . \quad (3.6)$$

Being in agreement with conditions (A) and (B), one of the most simple approximate forms of G_{12} is the Hartree-Fock approximation [13, 55],

$$G_{12}(12; 1' 2') = G(1, 1') G(2, 2') \pm G(1, 2') G(2, 1') . \quad (3.7)$$

Here, the interactions between the quantum particles are treated at mean-field level and one sums up the (direct) Hartree term and the contribution from the exchange potential. However, to do so means that one neglects all kinds of correlation effects, and inserting expression (3.7) into the general KKBE yields equations of motion which are identical to the well known time-dependent Hartree-Fock (TDHF) equations [56]—for time-independent Hartree-Fock calculations see also Sect. 4.1.

To do better than Eq. (3.7), it is helpful to make use of field theoretical perturbation techniques. To this end, a formal decoupling of the MS hierarchy can be obtained by replacing the right hand sides of the KKBE by integrations over the so-called *self-energy* $\Sigma(1, 2)$, i.e. for the first equation

$$\pm i \int_{\mathcal{C}} d3 W(1-3) G_{12}(13; 23^+) =: \int_{\mathcal{C}} d3 \Sigma[G](1, 3) G(3, 2) , \quad (3.8)$$

where $\Sigma(1, 2)$ appears as a functional of the single-particle Green's function $G(1, 2)$. Thus, both Keldysh/Kadanoff-Baym equations transform into the closed (or self-consistent) form

$$(i \partial_{t_1} - h^0(1)) G(1, 2) = \delta_{\mathcal{C}}(1-2) + \int_{\mathcal{C}} d3 \Sigma[G](1, 3) G(3, 2) , \quad (3.9)$$

$$(-i \partial_{t_2} - h^0(2)) G(1, 2) = \delta_{\mathcal{C}}(1-2) + \int_{\mathcal{C}} d3 G(1, 3) \Sigma[G](3, 2) . \quad (3.10)$$

The remaining question is now, how to derive appropriate expressions for the one-particle self-energy $\Sigma[G](1, 2)$ which are consistent with the above criteria (A) and (B) about conserving approximations. But this has been answered by Baym [54], who has shown that if the self-energy is obtained from a functional derivative of an underlying functional $\Phi[G]$, i.e.

$$\Sigma[G](1, 2) = \frac{\delta \Phi[G]}{\delta G(2, 1)} , \quad (3.11)$$

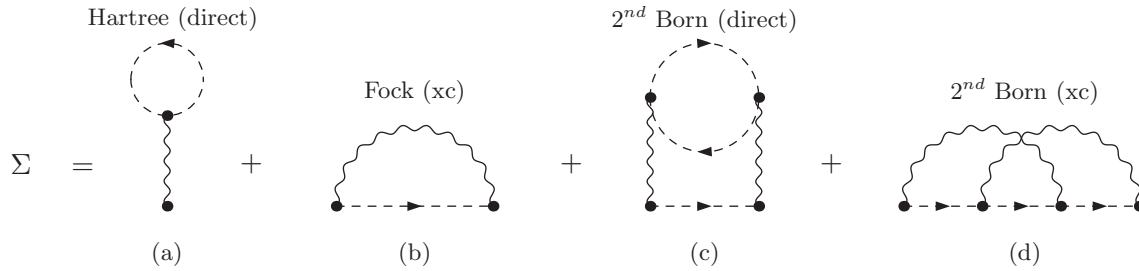


Figure 3.1: First (a,b) and second order (c,d) contributions to the diagrammatic self-energy expansion. Displayed are the Feynman (skeleton) diagrams corresponding to $\Sigma(1,2) = \Sigma^{\text{HF}}(x_1, x_2) \delta_{\mathcal{C}}(t_1 - t_2) + \Sigma^{\text{corr,B}}(1,2)$. The dashed lines denote the Green's functions or propagators G and the solid wavy lines indicate the interaction links W . "xc" means exchange.

conditions (A) and (B) are automatically satisfied and consequently all conservation laws, too. In particular, requirement (B) is then equivalent to saying that Eqs. (3.9) and (3.10) remain unchanged upon the transformation $G(12, 1^+2^+) \rightarrow G(21, 2^+1^+)$.

Moreover, any such Φ -derivable approximation according to Eq. (3.11) allows for a systematic summation of the different self-energy contributions in terms of interaction diagrams. This is demonstrated in Fig. 3.1, where besides the first order Hartree-Fock diagrams, (a) and (b), also the second order diagrams of the *second Born approximation* are displayed, (c) and (d). The first order diagrams thereby include only a single Green's function G (propagator) and a single interaction line W , while both second order diagrams consist of three propagators and two interactions. Further, each term of the order m takes a prefactor of γi^m whereby the sign is alternating between $\gamma = \pm 1$ for the direct contributions and $\gamma = 1$ for the exchange terms. Translated back into formulas [14], the Hartree-Fock self-energy reads

$$\begin{aligned} \Sigma^{\text{HF}}(1,2) &= \Sigma^{\text{F/xc}}(1,2) + \Sigma^{\text{H}}(1,2) \\ &= i G(1,2) W(1^+, 2) \pm i \delta_{\mathcal{C}}(1-2) \int d3 W(1,3) G(3,3^+) \end{aligned} \quad (3.12)$$

$$= i \delta_{\mathcal{C}}(t_1^+ - t_2) \left(G(1,2) w(x_1 - x_2) \pm \delta(x_1 - x_2) \int d3 W(1,3) G(3,3^+) \right), \quad (3.13)$$

and the additional contributions arising in second Born approximation and accounting for correlation effects are given by

$$\begin{aligned} \Sigma^{\text{corr,B}}(1,2) &= \Sigma_1^{\text{corr,B}}(1,2) + \Sigma_2^{\text{corr,B}}(1,2) \\ &= i^2 \iint d3 d4 G(1,3) W(1^+, 4) G(3,4) G(4,2) W(3^+, 2) \\ &\quad \pm i^2 \iint d3 d4 G(1,2) W(1^+, 3) W(2,4) G(4,3) G(3,4^+). \end{aligned} \quad (3.14)$$

The total self-energy entering and, thus, completing the equations of motion (3.9) and (3.10) is then the sum $\Sigma(1,2) = \Sigma^{\text{HF}}(1,2) + \Sigma^{\text{corr,B}}(1,2)$.

Besides the self-energy expression which follows from Eqs. (3.12) and (3.14) there exist other partially more sophisticated conserving schemes like the GW method [21, 49, 54] or the T -matrix approximation [21, 51, 54]. However, the present expansion up to second order is the most convenient form of including correlations and will be applied in this work only.

In order to make the mathematical structure of the Keldysh/Kadanoff-Baym equations (3.9) and (3.10) more obvious, it is worth working out the equations in terms of the greater and lesser correlation functions $G^{\gtrless}(1,2)$ and writing the collision integrals in a more explicit form.

Thereby, the contour delta functions $\delta_{\mathcal{C}}$ vanish and the KKBE become

$$\begin{aligned} (i \partial_{t_1} - h^0(1)) G^{\gtrless}(1, 2) &= \int_{t_0}^{t_1} d3 \Sigma^R(1, 3) G^{\gtrless}(3, 2) + \int_{t_0}^{t_2} d3 \Sigma^{\gtrless}(1, 3) G^A(3, 2) \\ &\quad - i \int_0^\beta d3 \Sigma^{\lrcorner}(1, 3) G^{\lrcorner}(3, 1) , \end{aligned} \quad (3.15)$$

$$\begin{aligned} (-i \partial_{t_2} - h^0(2)) G^{\gtrless}(1, 2) &= \int_{t_0}^{t_1} d3 G^R(1, 3) \Sigma^{\gtrless}(3, 2) + \int_{t_0}^{t_2} d3 G^{\gtrless}(1, 3) \Sigma^A(3, 2) \\ &\quad - i \int_0^\beta d3 G^{\lrcorner}(1, 3) \Sigma^{\lrcorner}(3, 1) . \end{aligned} \quad (3.16)$$

Bear in mind, that the definition of the retarded and advanced quantities here differ from the conventional definition (2.24) by

$$G^{R/A}(1, 2) = G^{\gtrless}(1, 2) - G^{\lessgtr}(1, 2) , \quad \Sigma^{R/A}(1, 2) = \Sigma^{\gtrless}(1, 2) - \Sigma^{\lessgtr}(1, 2) . \quad (3.17)$$

While the l.h.s. of the KKBE—involving time derivative and single-particle Hamiltonian $h^0(1)$ —is relatively simple, the collision term appearing on the r.h.s. is more involved extending over the Keldysh-contour. The first two integrals thereby include integrations over all earlier times $t_0 \leq t_3 \leq t_1, t_2$ and, thus, act as memory kernels and take care of non-Markovian effects which become important when binary (or higher) correlations are taken into account. The last term integrating the mixed functions over the imaginary branch of \mathcal{C} finally accounts for the correct influence of initial correlations at times $t_{1,2} \geq t_0$.

3.2. Basis representation of the Green's function

In order to derive equations of motion for the Green's function which are better tractable numerically than Eqs. (3.9) and (3.10), it is useful to expand the Green's function $G(1, 2)$ in a suitable basis $\{\phi_i(x)\}$, $i = 0, 1, 2, \dots$, [16]. The natural orbitals (NO) or single-particle wave functions $\phi_i(x)$ may thereby obey a single-particle eigenvalue problem such as a stationary Schrödinger equation of the form $h^0(x, t_0) \phi_m(x) = \epsilon_m \phi_m(x)$, or may arise from a more sophisticated problem as e.g. a Hartree-Fock Hamiltonian which partially—at mean-field level—takes interaction effects into account. However, the fulfillment of completeness and orthonormality is an important demand on the orbitals $\phi_i(x)$ when used to expand the Green's function, i.e.

$$\sum_{m=0}^{\infty} \phi_m^*(x) \phi_m(x') = \delta(x - x') \quad (3.18)$$

$$\int dx \phi_k^*(x) \phi_l(x) = \delta_{kl} . \quad (3.19)$$

For the single-particle Green's function, the basis representation of the field operators $\Psi_H^{(\dagger)}(1)$ in the Heisenberg picture now implies the following expansion which includes coefficients $g_{kl}(t_1, t_2)$ of $G(1, 2)$ that depend on time-arguments only:

$$G(1, 2) = G(x_1 t_1, x_2 t_2) = \sum_{kl} \phi_k(x_1) \phi_l^*(x_2) g_{kl}(t_1, t_2) . \quad (3.20)$$

More precisely, this means that one begins with the transformation of the field operators into the single-particle basis $\{\phi_i(x)\}$ [17] according to

$$\Psi_H(x t) = \sum_{m=0}^{\infty} \phi_m(x) c_m(t) , \quad \Psi_H^\dagger(x t) = \sum_{m=0}^{\infty} \phi_m^*(x) c_m^\dagger(t) , \quad (3.21)$$

where $c_i^\dagger(t)$ and $c_i(t)$ denote time-dependent creation and annihilation operators which are connected with the level i and are also to be understood in the Heisenberg picture. Only for brevity the subscript H indicating the evolution picture has been neglected. Further, the operators $c_i^{(\dagger)}(t)$ obey—similar to the field operators themselves—at equal time-arguments the commutation relations ($\mp \equiv$ bosons/fermions)

$$\left[c_k(t), c_l^\dagger(t) \right]_{\mp} = \delta_{kl}, \quad (3.22)$$

$$\left[c_k^{(\dagger)}(t), c_l^{(\dagger)}(t) \right]_{\mp} = 0. \quad (3.23)$$

Then, one directly can insert the expressions (3.21) for the field operators into definition (2.11) of the single-particle Green's function in the contour (see Sect. 2.2) and finds that

$$\begin{aligned} G(x_1 t_1, x_2 t_2) &= -i \left\langle T_{\mathcal{C}} \left[\Psi_H(1) \Psi_H^\dagger(2) \right] \right\rangle \\ &= -i \sum_{kl} \phi_k(x_1) \phi_l^*(x_2) \left\langle T_{\mathcal{C}} \left[c_k(t_1) c_l^\dagger(t_2) \right] \right\rangle \\ &= \sum_{kl} \phi_k(x_1) \phi_l^*(x_2) g_{kl}(t_1, t_2). \end{aligned} \quad (3.24)$$

Consequently, the coefficients $g_{kl}(t_1, t_2) \equiv -i \langle T_{\mathcal{C}} [c_k(t_1) c_l^\dagger(t_2)] \rangle$ —which can be comprised into a single matrix $\mathbf{g}(t_1, t_2)$ —are simply the time-ordered Green's functions with respect to the creation and annihilation operators c_i^\dagger and c_i in the given basis.

In addition, alike the full space-time Green's function $G(1, 2)$ one also can define all kinds of subordinated quantities $G^*(1, 2)$, $*$ $\equiv \{M, \gtrsim, \lceil/\rceil\}$, with respect to the creation and annihilation operators. For instance, the basis elements of the Matsubara Green's function, with its time-arguments $\tau_{1,2} \in \mathfrak{Im} \mathcal{C}$, and of the real-time correlation functions read

$$g_{kl}^M(\tau_1, \tau_2) = -i \left\langle c_l^\dagger(t_0 - i\tau_1) c_k(t_0 - i\tau_2) \right\rangle, \quad (3.25)$$

$$g_{kl}^{\lceil/\rceil}(t_1, t_2) = \pm(1/i) \left\langle c_l^\dagger(t_2) c_k(t_1) \right\rangle, \quad (3.26)$$

$$g_{kl}^{\gtrsim}(t_1, t_2) = (1/i) \left\langle c_k(t_1) c_l^\dagger(t_2) \right\rangle, \quad (3.27)$$

and thus transform—as well as the mixed functions $G^{\lceil/\rceil}(1, 2)$ —into square matrices $\mathbf{g}^*(t_1, t_2)$ with $*$ $\equiv \{M, \gtrsim, \lceil/\rceil\}$ and $t_{1,2} \in \mathcal{C}$. Further, the single-particle self-energy $\Sigma(1, 2)$ entering the Keldysh/Kadanoff-Baym equations (3.9,3.10) can be translated in the same way as $G(1, 2)$ in Eq. (3.20), i.e. it attains the form

$$\Sigma(1, 2) = \sum_{kl} \phi_k(x_1) \phi_l^*(x_2) \Sigma_{kl}(t_1, t_2), \quad (3.28)$$

and, again, one can distinguish the quantities $\Sigma^*(t_1, t_2)$, $*$ $\equiv \{M, \gtrsim, \lceil/\rceil\}$. Moreover, the generalization to s -particle quantities is straightforward. When the Green's function accounts for $2s$ space-time coordinates $(1 \dots s, 1' \dots s') = (x_1 t_1 \dots x_s t_s, x_{s+1} t_{s+1} \dots x_{2s} t_{2s})$, then the expansion in terms of the orbitals $\phi_i(x)$ includes $2s$ summations according to

$$\begin{aligned} G_{1 \dots s}(1 \dots s, 1' \dots s') &= \sum_{k_1 \dots k_{2s}} \phi_{k_1}(x_1) \dots \phi_{k_s}(x_s) \phi_{k_{2s}}^*(x_{2s}) \dots \phi_{k_{s+1}}^*(x_{s+1}) \times \\ &\quad \times g_{k_1 \dots k_s, k_{2s} \dots k_{s+1}}(t_1 \dots t_s, t_{s+1} \dots t_{2s}), \end{aligned} \quad (3.29)$$

where the object $\mathbf{g}(t_1 \dots t_s, t_{s+1} \dots t_{2s})$ now takes $2s$ indices and depends on $2s$ time-arguments.

3.3. Keldysh/Kadanoff-Baym equations for $g_{kl}^{M, \gtrless, |/\rangle} (t_1, t_2)$

Once one has expanded the Green's function and the self-energy according to Eq. (3.20) and Eq. (3.28), respectively, the thermodynamic equilibrium state is fully characterized by the matrices $\mathbf{g}^M(\tau_1, \tau_2)$ and $\mathbf{\Sigma}^M(\tau_1, \tau_2)$ and, further, the time-evolution of the system is fully determined by the temporal behavior of the matrices $\mathbf{g}^\star(t_1, t_2)$ and $\mathbf{\Sigma}^\star(t_1, t_2)$ with $\star \equiv \{\gtrless, |/\rangle\}$. However, what is left unknown so far are the equations of motion for these quantities. These are to be derived in the present section.

Without anticipating the final result, one may notice that the equations of motion will appear in the pure time-domain but otherwise will structurally be similar to the general KKBE which contain both time *and* space coordinates. In principle, one simply may replace the Green's function and the self-energy entering Eqs. (3.9) and (3.10) by their respective two-time matrices and consequently may reduce the spatial integrations over $w(x_1 - x_2)$ to matrix elements of the pair-interaction potential. Nevertheless, the formal derivation which now follows gives some more insight and, furthermore, reveals the procedure needed for an analogous derivation of the general equations which has only been touched by Sect. 3.1.

As for the general Keldysh/Kadanoff-Baym equations, the starting point of the derivation is here the Heisenberg equation for the field operators, i.e.

$$i \partial_t \Psi_H^{(\dagger)}(xt) = \left[\Psi_H^{(\dagger)}(xt), H_H(t) \right]_- , \quad (3.30)$$

according to the many-body system governed by the second-quantized Hamiltonian (in Heisenberg's picture)

$$H_H(t) = H_1(t) + H_{12}(t) , \quad (3.31)$$

$$H_1(t) = \int dx' \Psi_H^\dagger(x't) h^0(x', t) \Psi_H(x't) , \quad (3.32)$$

$$H_{12}(t) = \iint dx dx' \Psi_H^\dagger(xt) \Psi_H^\dagger(x't) w(x - x') \Psi_H(x't) \Psi_H(xt) . \quad (3.33)$$

Since the Hamiltonian $H_H(t)$ splits into the two contributions (3.32) and (3.33), one further can consider the different parts separately in the equation of motion.

i. Contributions from $H_1(t)$:

Insert the expansion of the field operators $\Psi_H^{(\dagger)}(xt) = \sum_k(x) \phi_k^{(*)}(x) c_k^{(\dagger)}(t)$ and $H_1(t)$ into the Heisenberg equation, Eq. (3.30). Note, that for a short notation a few time-arguments have been neglected in some of the following expressions for the creation and annihilation operators.

a) The commutator of $\Psi(xt)$ with $H_1(t)$ yields

$$\begin{aligned} [\Psi_H(xt), H_1(t)]_- &= \sum_{klm} \int dx' \phi_m(x) \phi_k^*(x') h^0(x', t) \phi_l(x') \left(c_m c_k^\dagger c_l - c_k^\dagger c_l c_m \right) \\ &= \sum_{klm} \phi_m(x) \int dx' \phi_k^*(x') h^0(x', t) \phi_l(x') \underbrace{\left(c_m c_k^\dagger \mp c_k^\dagger c_m \right)}_{=\delta_{km}} c_l(t) \\ \sum_m i \partial_t \phi_m(x) c_m(t) &= + \sum_{kl} \phi_k(x) h_{kl}^0(t) c_l(t) . \end{aligned} \quad (3.34)$$

b) The commutator of the adjoint field operator $\Psi^\dagger(x't')$ with $H_1(t')$ gives

$$\begin{aligned} [\Psi_H^\dagger(x't'), H_1(t')]_- &= \sum_{klm} \int dx \phi_m^*(x') \phi_k^*(x) h^0(x, t') \phi_l(x) \left(c_m^\dagger c_k^\dagger c_l - c_k^\dagger c_l c_m^\dagger \right) \\ &= - \sum_{klm} \phi_m^*(x') h_{kl}^0(t') c_k^\dagger(t') \underbrace{\left(\mp c_m^\dagger c_l + c_l c_m^\dagger \right)}_{=\delta_{lm}} \\ \sum_m i\partial_{t'} \phi_m^*(x') c_m^\dagger(t') &= - \sum_{kl} \phi_l^*(x') h_{kl}^0(t') c_k^\dagger(t') . \end{aligned} \quad (3.35)$$

On the l.h.s. of Eqs. (3.34) and (3.35) one has introduced the time-derivative of the Heisenberg equation (3.30), and on the r.h.s. the matrix $\mathbf{h}^0(t)$ contains the integrals

$$h_{kl}^0(t) = \int dx \phi_k^*(x) h^0(x, t) \phi_l(x) . \quad (3.36)$$

As a side remark: If one assumes the separability $\mathbf{h}^0(x, t) = \bar{\mathbf{h}}(x) + \mathbf{v}_{\text{ext}}(x, t)$ into a stationary and a time-dependent part and allows the orbitals $\phi_k(x)$ to be exact eigenstates to $\bar{\mathbf{h}}(x)$, one can refine the integrals to be $h_{kl}^0(t) = \epsilon_k \delta_{kl} + \int dx \phi_k^*(x) v_{\text{ext}}(x, t) \phi_l(x)$ with ϵ_k being the corresponding energy eigenvalues of the level k .

Through comparison of coefficients with respect to the orbitals $\phi_m(x)$ and $\phi_m^*(x')$ one further finds from the last equalities in a) and b), Eq. (3.34) and Eq. (3.35), that

$$i\partial_t c_k(t) - \sum_m h_{km}^0(t) c_m(t) = 0 \quad (3.37)$$

$$-i\partial_{t'} c_l^\dagger(t') - \sum_m c_m^\dagger(t') h_{ml}^0(t') = 0 . \quad (3.38)$$

After multiplication by the creation operator $c_l^\dagger(t')$ from the r.h.s. and the annihilation operator $c_k(t)$ from the l.h.s., time-ordering via $T_{\mathcal{C}}$ and ensemble averaging one finally arrives at

$$i\partial_t \left\langle T_{\mathcal{C}} \left[c_k(t) c_l^\dagger(t') \right] \right\rangle - \sum_m h_{km}^0(t) \left\langle T_{\mathcal{C}} \left[c_m(t) c_l^\dagger(t') \right] \right\rangle = i\delta_{\mathcal{C}}(t - t') , \quad (3.39)$$

$$-i\partial_{t'} \left\langle T_{\mathcal{C}} \left[c_k(t) c_l^\dagger(t') \right] \right\rangle - \sum_m \left\langle T_{\mathcal{C}} \left[c_k(t) c_m^\dagger(t') \right] \right\rangle h_{ml}^0(t') = i\delta_{\mathcal{C}}(t - t') , \quad (3.40)$$

where the contour delta functions on the r.h.s. arise from writing $T_{\mathcal{C}}$ under the time derivative which does not commute with $T_{\mathcal{C}}$ [14]. Further, it is $-i\langle T_{\mathcal{C}}[c_k(t) c_l^\dagger(t')] \rangle = g_{kl}(t, t')$. Depending on how the time-arguments t and t' are now arranged on the Keldysh-contour, Eqs. (3.39) and (3.40) directly allow to identify the equations of motion for the subordinated quantities $g_{kl}^*(t_1, t_2)$, $* \equiv \{M, \gtrless, \lrcorner/\lrcorner\}$. For instance, the lesser and greater correlation functions then obey (with respect to $H_1(t)$ only)

$$i\partial_t g_{kl}^{\gtrless}(t, t') - \sum_m h_{km}^0(t) g_{ml}^{\gtrless}(t, t') = 0 , \quad (3.41)$$

$$-i\partial_{t'} g_{kl}^{\gtrless}(t, t') - \sum_m g_{km}^{\gtrless}(t, t') h_{ml}^0(t') = 0 , \quad (3.42)$$

which can equivalently be written in form of a matrix equation including the standard matrix multiplication $(\mathbf{A}\mathbf{B})_{kl} = \sum_m A_{km} B_{ml}$:

$$i\partial_t \mathbf{g}^{\gtrless}(t, t') - \mathbf{h}^0(t) \mathbf{g}^{\gtrless}(t, t') = 0 , \quad (3.43)$$

$$-i\partial_{t'} \mathbf{g}^{\gtrless}(t, t') - \mathbf{g}^{\gtrless}(t, t') \mathbf{h}^0(t') = 0 . \quad (3.44)$$

ii. **Contributions from $H_{12}(t)$:**

In Eqs. (3.39) and (3.40), there is no pair-interaction potential $w(x, x') \equiv w(x - x')$ included. To incorporate this, it is necessary to calculate the commutator of the field operator with the interaction part $H_{12}(t)$. Together with the Heisenberg equation this will then lead to a non-vanishing r.h.s. of the equations of motion.

a) Heisenberg equation for $\Psi_H(xt)$:

$$\begin{aligned}
 [\Psi_H(xt), H_{12}(t)]_- &= \frac{1}{2} \sum_{ijklm} \iint dx' dx'' \phi_m(x) \phi_i^*(x') \phi_k^*(x'') w(x', x'') \phi_j(x') \phi_l(x'') \\
 &\quad \times \left(c_m c_i^\dagger c_k^\dagger c_l c_j - c_i^\dagger c_k^\dagger c_l c_j c_m \right) \\
 &= \frac{1}{2} \sum_{ijklm} \phi_m(x) w_{ij,kl} \left(c_m c_i^\dagger c_k^\dagger c_l c_j - c_i^\dagger c_k^\dagger c_m c_l c_j \right) \\
 &= \frac{1}{2} \sum_{ijklm} \phi_m(x) w_{ij,kl} \left(c_m c_i^\dagger c_k^\dagger c_l c_j - c_i^\dagger \left[\mp \delta_{klm} \pm c_m c_k^\dagger \right] c_l c_j \right) \\
 &= \frac{1}{2} \sum_{ijklm} \phi_m(x) w_{ij,kl} \left(\pm \delta_{km} c_i^\dagger c_l c_j + \delta_{im} c_k^\dagger c_l c_j \right) \\
 &= \pm \frac{1}{2} \sum_{ijkl} \phi_k(x) w_{ij,kl} c_i^\dagger c_l c_j + \frac{1}{2} \sum_{ijkl} \phi_i(x) w_{ij,kl} c_k^\dagger c_l c_j \quad (3.45)
 \end{aligned}$$

$$\sum_m i\partial_t \phi_m(x) c_m(t) = + \sum_{ijkl} \phi_i(x) w_{ij,kl} c_k^\dagger(t) c_l(t) c_j(t). \quad (3.46)$$

To arrive at the last equality, one in Eq. (3.45) has used the symmetry of the pair-interaction potential, i.e. more precisely $w_{ij,kl} \equiv w_{kl,ij}$ —for definition see Eq. (3.48).

b) Analogously to a), one finds from the adjoint field operator that

$$\sum_m i\partial_t \phi_m^*(x') c_m^\dagger(t') = - \sum_{ijkl} \phi_j^*(x') w_{ij,kl} c_i^\dagger(t') c_k^\dagger(t') c_l(t'). \quad (3.47)$$

The introduced integrals $w_{ij,kl}$ —also called two-electron integrals in the fermionic case—are defined by

$$w_{ij,kl} = \iint dx' dx'' \phi_i^*(x') \phi_k^*(x'') w(x' - x'') \phi_j(x') \phi_l(x''), \quad (3.48)$$

where indices separated by comma refer to different spatial coordinates. Further, similar to step (i) it follows from Eqs. (3.46) and (3.47) after comparison of coefficients, multiplication by operators $c_l^\dagger(t')$ and $c_k(t)$, time-ordering and ensemble averaging:

$$\begin{aligned}
 i\partial_t \left\langle T_C \left[c_k(t) c_l^\dagger(t') \right] \right\rangle &= i\delta_C(t - t') \\
 &\quad \pm \int_C d\bar{t} \delta_C(\bar{t} - t) \sum_{bcd} w_{kb,cd} \left\langle T_C \left[c_d(t) c_b(\bar{t}) c_c^\dagger(\bar{t}^+) c_l^\dagger(t') \right] \right\rangle, \quad (3.49)
 \end{aligned}$$

$$\begin{aligned}
 -i\partial_{t'} \left\langle T_C \left[c_k(t) c_l^\dagger(t') \right] \right\rangle &= i\delta_C(t - t') \\
 &\quad \pm \int_C d\bar{t} \delta_C(\bar{t} - t') \sum_{acd} \left\langle T_C \left[c_k(t) c_d(\bar{t}) c_a^\dagger(\bar{t}^+) c_l^\dagger(t') \right] \right\rangle w_{al,cd}, \quad (3.50)
 \end{aligned}$$

where on the r.h.s. one additionally has used the cyclic property of the trace included in $\langle \dots \rangle$ to rearrange the creation and annihilation operators, and moreover has introduced the contour integrations to supply the time-arguments with an unambiguous ordering on \mathcal{C} . Multiplication of both equations by $-i$ and identification of the averaged quantities with the one- and two-particle Green's function matrices yields

$$i\partial_t g_{kl}(t, t') = \delta_{\mathcal{C}}(t - t') \pm i \int_{\mathcal{C}} d\bar{t} \delta_{\mathcal{C}}(\bar{t} - t) \sum_{bcd} w_{kb,cd} g_{db,lc}(t\bar{t}, t' \bar{t}^+) , \quad (3.51)$$

$$-i\partial_{t'} g_{kl}(t, t') = \delta_{\mathcal{C}}(t - t') \pm i \int_{\mathcal{C}} d\bar{t} \delta_{\mathcal{C}}(\bar{t} - t') \sum_{acd} g_{kd,ca}(t\bar{t}, t' \bar{t}^+) w_{al,cd} . \quad (3.52)$$

Analogue to Sect. 3.1, a formal decoupling can then be obtained by introducing the self-energy $\Sigma_{kl}(t, t')$, i.e. by writing the equations of motion above as

$$i\partial_t g_{kl}(t, t') = \delta_{\mathcal{C}}(t - t') + \int_{\mathcal{C}} d\bar{t} \sum_m \Sigma_{km}[\mathbf{g}](t, \bar{t}) g_{ml}(\bar{t}, t') , \quad (3.53)$$

$$-i\partial_{t'} g_{kl}(t, t') = \delta_{\mathcal{C}}(t - t') + \int_{\mathcal{C}} d\bar{t} \sum_m g_{km}(t, \bar{t}) \Sigma_{ml}[\mathbf{g}](\bar{t}, t') . \quad (3.54)$$

Combining Eqs. (3.39-3.40) and Eqs. (3.53-3.54), one finally arrives at the complete set of equations of motion for $g_{kl}(t, t')$ which describe the interacting Fermi or Bose system. Evaluating them for the lesser and greater correlation functions $\mathbf{g}^{\lessgtr}(t, t')$ and furthermore decomposing the contour integrals on the r.h.s. into real and imaginary time contributions gives

$$\begin{aligned} i\partial_t \mathbf{g}^{\lessgtr}(t, t') - \mathbf{h}^0(t) \mathbf{g}^{\lessgtr}(t, t') &= \int_{t_0}^t d\bar{t} \Sigma^R(t, \bar{t}) \mathbf{g}^{\lessgtr}(\bar{t}, t') + \int_{t_0}^{t'} d\bar{t} \Sigma^{\lessgtr}(t, \bar{t}) \mathbf{g}^A(\bar{t}, t') \\ &\quad - i \int_0^{\beta} d\bar{\tau} \Sigma^{\lrcorner}(t, \bar{\tau}) \mathbf{g}^{\lrcorner}(\bar{\tau}, t') , \end{aligned} \quad (3.55)$$

$$\begin{aligned} -i\partial_{t'} \mathbf{g}^{\lessgtr}(t, t') - \mathbf{g}^{\lessgtr}(t, t') \mathbf{h}^0(t') &= \int_{t_0}^t d\bar{t} \mathbf{g}^R(t, \bar{t}) \Sigma^{\lessgtr}(\bar{t}, t') + \int_{t_0}^{t'} d\bar{t} \mathbf{g}^{\lessgtr}(t, \bar{t}) \Sigma^A(\bar{t}, t') \\ &\quad - i \int_0^{\beta} d\bar{\tau} \mathbf{g}^{\lrcorner}(t, \bar{\tau}) \Sigma^{\lrcorner}(\bar{\tau}, t') , \end{aligned} \quad (3.56)$$

where the retarded and advanced quantities are defined according to Eq. (3.17), Sect. 3.1.

3.3.1. Self-energy contributions

Similar to Sect. 3.1, the basis representation of the Green's function allows for a diagrammatic expansion of the self-energy matrix $\Sigma[\mathbf{g}](t, t')$ entering the equations of motion. As shown in Fig. 3.2, the propagator lines are thereby identifiable with the matrix elements $g_{kl}(t, t')$ and the interaction lines directly correspond to the objects $w_{ij,kl}$. Indicating the same structure as found in Eqs. (3.12-3.14) [16], the Hartree-Fock self-energy follows to be

$$\begin{aligned} \Sigma_{ij}^{\text{HF}}(t, t') &= \Sigma_{ij}^{\text{H}}(t, t') + \Sigma_{ij}^{\text{F/xc}}(t, t') \\ &= \delta_{\mathcal{C}}(t - t') \sum_{kl} (w_{kl,ij} \pm w_{kj,il}) g_{kl}(t, t') , \end{aligned} \quad (3.57)$$

while for the second Born terms one obtains

$$\begin{aligned} \Sigma_{ij}^{\text{corr,B}}(t, t') &= \Sigma_{2,ij}^{\text{corr,B}}(t, t') + \Sigma_{1,ij}^{\text{corr,B}}(t, t') \\ &= \sum_{klmnr} w_{ik,ms} (w_{lj,rn} \pm w_{nj,rl}) g_{kl}(t, t') g_{mn}(t, t') g_{rs}(t', t) . \end{aligned} \quad (3.58)$$

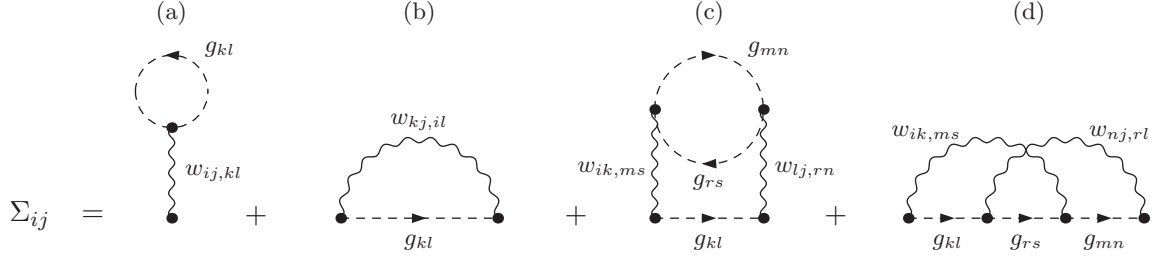


Figure 3.2: Diagrammatic expansion of the self-energy matrix $\Sigma(t, t') = \Sigma^{\text{HF}} \delta_{\mathcal{C}}(t - t') + \Sigma^{\text{corr, B}}(t, t')$ up to second order. As in Fig. 3.1, the dashed lines denote the propagators and the solid wavy lines indicate the interactions. The matrix elements g_{kl} arise from definition (3.20) and the two-particle integrals $w_{ij,kl}$ are as defined in Eq. (3.48). (a,b): Hartree-Fock mean-field, (c,d): second Born terms.

3.3.2. KKBE in basis representation. Summary

Collecting Eqs. (3.39), (3.40), (3.53) and (3.54) and evaluating them for the different possibilities of $t_{1,2} \in \mathcal{C}$, the Keldysh/Kadanoff-Baym equations—in *basis representation*—follow to be coupled integro differential equations for the square matrices $\mathbf{g}^*(t_1, t_2)$, $* \equiv \{M, \gtrless, \lrcorner/\lrcorner\}$. With the tree different types of collision integrals on the right hand sides, $\mathbf{I}^{\gtrless}(t_1, t_2)$, $\mathbf{I}^{\lrcorner/\lrcorner}(t_1, t_2)$ and $\mathbf{I}^M(t_1, t_2)$, they read

$$(i\partial_{t_1} - \mathbf{h}(t_1)) \mathbf{g}^{\gtrless}(t_1, t_2) = \left[\Sigma^R \bullet \mathbf{g}^{\gtrless} + \Sigma^{\gtrless} \circ \mathbf{g}^A + \Sigma^{\lrcorner} \star \mathbf{g}^{\lrcorner} \right] (t_1, t_2) = \mathbf{I}_1^{\gtrless}(t_1, t_2), \quad (3.59)$$

$$\mathbf{g}^{\gtrless}(t_1, t_2) (-i\partial_{t_2} - \mathbf{h}(t_2)) = \left[\mathbf{g}^R \bullet \Sigma^{\gtrless} + \mathbf{g}^{\gtrless} \circ \Sigma^A + \mathbf{g}^{\lrcorner} \star \Sigma^{\lrcorner} \right] (t_1, t_2) = \mathbf{I}_2^{\gtrless}(t_1, t_2), \quad (3.60)$$

$$(i\partial_{t_1} - \mathbf{h}(t_1)) \mathbf{g}^{\lrcorner}(t_1, t_2) = \left[\Sigma^R \bullet \mathbf{g}^{\lrcorner} + \Sigma^{\lrcorner} \star \mathbf{g}^M \right] (t_1, t_2) = \mathbf{I}^{\lrcorner}(t_1, t_2), \quad (3.61)$$

$$\mathbf{g}^{\lrcorner}(t_1, t_2) (-i\partial_{t_2} - \mathbf{h}(t_2)) = \left[\mathbf{g}^{\lrcorner} \circ \Sigma^A + \mathbf{g}^M \star \Sigma^{\lrcorner} \right] (t_1, t_2) = \mathbf{I}^{\lrcorner}(t_1, t_2), \quad (3.62)$$

$$(-\partial_{\tau_1} - \mathbf{h}(t_0)) \mathbf{g}^M(\tau_1, \tau_2) = i\delta(\tau_1 - \tau_2) + \left[\Sigma^M \star \mathbf{g}^M \right] (\tau_1, \tau_2) = \mathbf{I}^M(\tau_1, \tau_2), \quad (3.63)$$

$$(\partial_{\tau_2} - \mathbf{h}(t_0)) \mathbf{g}^M(\tau_1, \tau_2) = i\delta(\tau_1 - \tau_2) + \left[\Sigma^M \star \mathbf{g}^M \right] (\tau_1, \tau_2) = \mathbf{I}^M(\tau_1, \tau_2), \quad (3.64)$$

where the derivatives in Eqs. (3.60) and (3.62) are acting to the left and in $\mathbf{h}(t_1) = \mathbf{h}^0(t_1) + \Sigma^{\text{HF}}(t_1)$ one included the time-local Hartree-Fock self-energy. The signs in front of the τ -derivatives in Eqs. (3.63) and (3.64) are interchanged because τ_1 and τ_2 are situated on the imaginary branch of the contour. Recall that all bold quantities are matrices in the eigenstates $\phi_i(x)$, $i = 0, 1, 2, \dots$. Further, the operations \bullet , \circ and \star denote integrations over particular branches of the contour, i.e. more precisely

$$[\mathbf{a} \circ \mathbf{b}](t_1, t_2) = \int_{t_0}^{t_3} d\bar{t} \mathbf{a}(t_1, \bar{t}) \mathbf{b}(\bar{t}, t_2), \quad t_3 = \begin{cases} t_1, & \text{if } \circ = \bullet \\ t_2, & \text{if } \circ = \circ \end{cases}, \quad (3.65)$$

$$[\mathbf{a} \star \mathbf{b}](t_1, t_2) = -i \int_0^\beta d\bar{\tau} \mathbf{a}(t_1, \bar{\tau}) \mathbf{b}(\bar{\tau}, t_2). \quad (3.66)$$

The equations (3.63) and (3.64) determining the Matsubara (equilibrium) Green's function can further be simplified under application of special properties which $\mathbf{g}^M(\tau_1, \tau_2)$ obeys. This will be done in the following section.

3.3.3. Equilibrium Dyson equation

The set of equations (3.63) and (3.64) which lead to the finite temperature Matsubara Green's function $\mathbf{g}^M(1, 2)$ is usually referred to as the *Dyson equations* [17]. However, it is inconvenient to consider them in this particular form. Instead, one can take advantage of the fact that $\mathbf{g}^M(1, 2)$ and $\Sigma^M(1, 2)$ —varying solely on the imaginary part of the Keldysh-contour \mathcal{C} —only depend on the difference between their time-arguments $-i\tau_1$ and $-i\tau_2$. One therefore can define real functions according to

$$g_{ij}^M(\tau_1 - \tau_2) := -i g_{ij}^M(-i\tau_1, -i\tau_2), \quad (3.67)$$

$$\Sigma_{ij}^M(\tau_1 - \tau_2) := -i \Sigma_{ij}^M(-i\tau_1, -i\tau_2), \quad (3.68)$$

where without loss of generality one has assumed $t_0 \equiv 0$. The appearing relative time $\tau = \tau_1 - \tau_2$ then lies in the symmetric interval $[-\beta, +\beta]$, and as a direct consequence of the KMS boundary conditions (3.4-3.5) both quantities are (anti-)periodic in the inverse temperature β which means that it is

$$\mathbf{g}^M(\tau + \beta) = \pm \mathbf{g}^M(\tau), \quad \Sigma^M(\tau + \beta) = \pm \Sigma^M(\tau). \quad (3.69)$$

With these new quantities one can easily rewrite and simplify the set of equations of motion: Adding Eq. (3.63) and Eq. (3.64) and collecting all self-energy contributions in $\Sigma^M(t_1, t_2)$, one obtains

$$\left[\frac{-\partial_{\tau_1} + \partial_{\tau_2}}{2} - \mathbf{h}^0 \right] \frac{1}{i} \mathbf{g}^M(\tau_1, \tau_2) = \delta(\tau_1 - \tau_2) - \int_0^\beta d\bar{\tau} \Sigma^M(\tau_1, \bar{\tau}) \mathbf{g}^M(\bar{\tau}, \tau_2). \quad (3.70)$$

Further, by introducing definitions (3.67) and (3.68) in this expression and also inserting the relative time τ , one arrives at

$$[-\partial_\tau - \mathbf{h}^0] \mathbf{g}^M(\tau) = \delta(\tau) + \int_0^\beta d\bar{\tau} \Sigma^M(\tau_1 - \bar{\tau}) \mathbf{g}^M(\bar{\tau} - \tau_2), \quad (3.71)$$

Finally, to completely eliminate the time-arguments $\tau_{1,2}$, one can rearrange the integral by substituting $\tilde{\tau} = \bar{\tau} - \tau_2$, i.e.

$$[-\partial_\tau - \mathbf{h}^0] \mathbf{g}^M(\tau) = \delta(\tau) + \int_{-\tau_2}^0 d\tilde{\tau} \Sigma^M(\tau - \tilde{\tau}) \mathbf{g}^M(\tilde{\tau}) + \int_0^{\beta - \tau_2} d\tilde{\tau} \Sigma^M(\tau - \tilde{\tau}) \mathbf{g}^M(\tilde{\tau}) \quad (3.72)$$

$$\begin{aligned} &= \delta(\tau) + \int_{\beta - \tau_2}^\beta d\tilde{\tau} \Sigma^M(\tau - \tilde{\tau} + \beta) \mathbf{g}^M(\tilde{\tau} - \beta) + \int_0^{\beta - \tau_2} d\tilde{\tau} \Sigma^M(\tau - \tilde{\tau}) \mathbf{g}^M(\tilde{\tau}) \\ &= \delta(\tau) + \int_0^\beta d\tilde{\tau} \Sigma^M(\tau - \tilde{\tau}) \mathbf{g}^M(\tilde{\tau}), \end{aligned} \quad (3.73)$$

where in the last step the anti-periodicity property of the Matsubara Green's function and the self-energy has been used. The *Dyson equation* in its usual form thus reads

$$[-\partial_\tau - \mathbf{h}^0] \mathbf{g}^M(\tau) = \delta(\tau) + \int_0^\beta d\bar{\tau} \Sigma^M(\tau - \bar{\tau}) \mathbf{g}^M(\bar{\tau}). \quad (3.74)$$

Note, that—in contrast to the notation used at Eqs. (3.63) and (3.64)—the Matsubara quantity $\Sigma^M(\tau)$ here contains both the Hartree-Fock self-energy and all higher order self-energy expressions, and on the l.h.s thus appears the noninteracting part of the Hamiltonian, \mathbf{h}^0 , only. For the more advanced representation of the Dyson equation in its integral form [15] one refers to Sect. 4.3 and Eq. (4.25) in the following chapter.

Moreover, for linguistic convenience, the Matsubara Green's function in a self-energy approximation beyond Hartree-Fock, e.g. in second Born approximation, will be referred to as the *correlated* Matsubara Green's function in the remainder of this work and the corresponding equation of motion (3.74) will be called the *correlated* Dyson equation. The *uncorrelated* Dyson equation which only includes the time-local Hartree-Fock self-energy according to $\Sigma^M(\tau) \rightarrow \Sigma^0 \delta(\tau)$ is then given by

$$[-\partial_\tau - \mathbf{h}^0 - \Sigma^0] \mathbf{g}^0(\tau) = \delta(\tau), \quad (3.75)$$

where, in order to stress the difference, one has introduced the notation $\mathbf{g}^0(\tau)$ instead of $\mathbf{g}^M(\tau)$. Further, because of the anti-periodicity properties (3.69) of the Matsubara Green's function and the respective self-energy one can restrict oneself to exclusively solve the Dyson equations (3.74) and (3.75) on half the interval $[-\beta, +\beta]$. It is thereby convenient to use the negative sub-interval $[-\beta, 0]$, since this way the density matrix, which equals $\mathbf{g}^M(\tau)$ in the limit $\tau \rightarrow 0^-$, becomes directly accessible.

4. Numerical procedure and implementation

In the following sections, important numerical issues concerning the computation of the correlated equilibrium state (solution of the Dyson equation (3.74)) and the propagation of the two-time Green's functions under nonequilibrium conditions (solution of the KKBE (3.59-3.62)) are being discussed. Due to the basis representation of the nonequilibrium Green's functions and all other quantities entering the equations of motion, the objects to be handled are in general time-dependent matrices which allow—besides discretization in time or frequency—a numerically straightforward implementation.

However, the question arises in which particular basis the calculations should be carried out. Natural orbitals such as the familiar oscillator eigenfunctions for a harmonic confinement are appropriate to the spatial inhomogeneity but do not take the particle interactions into account. It is therefore convenient [15] to spend efforts and CPU time on obtaining a more advanced basis set, as e.g. wave functions obeying an effective single-particle equation (Hartree-Fock or mean-field equation) or orbitals obtained via density functional theory (DFT) calculations. Including only lowest order self-energy contributions the corresponding Green's functions are much easier accessible than the correlated ones and will serve as good start or reference quantities in iterative schemes which lead to higher order solutions of (3.59-3.64) as they will be discussed in Sect. 4.3.

Here, it has been found advantageous—with respect to the applicability to a variety of systems—to implement a Hartree-Fock method in order to generally start from a Green's function being expanded in terms of Hartree-Fock orbitals [15, 48]. To this end the first and second section of this chapter covers the main ideas and its conditioning.

Furthermore, the numerical procedure which is implemented throughout in the direct time space is summarized as a whole in Sect. 4.4 by giving a schematic program overview, before afterwards—in the last Sect. 4.5—the time-propagation of $g_{ij}^*(t, t')$, $\star \equiv \{\gtrless, \lrcorner/\lrcorner\}$, is described in explicit detail.

4.1. Solving the Hartree-Fock equations

In a self-consistent Hartree-Fock (SCHF) theory [57, 58], the general many-particle problem can be replaced by an effective one-particle problem, where a single particle is moving in an effective static field. It can be viewed either as a variational method, where the full many-body wave function is approximated by a single Slater determinant $S_N(\{\Phi_i(x_j)\})$, or as the lowest order term in a perturbative expansion with respect to the particle interaction.

The following discussion leads to the central equations of the SCHF method—the Roothaan-Hall equations [59] which are well known from computation of atomic and molecular ground state orbitals. For generality the derivation is given for both fermions and bosons. As already mentioned in previous chapters, the many-particle problem takes the second-quantized form

$$H = \int dx \Psi^\dagger(x) h^0(x) \Psi(x) + \frac{1}{2} \iint dx dx' \Psi^\dagger(x) \Psi^\dagger(x') w(x, x') \Psi(x') \Psi(x), \quad (4.1)$$

where, for instance, it is $h^0(x) = [-\frac{1}{2}\nabla_x^2 + V_{\text{ext}}(x)]$, the quantity $\Psi(x)$ denotes a bosonic or fermionic field operator, and $w(x, x')$ is the pair-interaction potential. Using the generalized density $\rho(x, x') = \langle \Psi^\dagger(x) \Psi(x') \rangle$ with a grand canonical ensemble averaging including an inverse

4. Numerical procedure and implementation

temperature β and a chemical potential μ , the interaction term of (4.1) can be replaced in Hartree-Fock approximation according to

$$\begin{aligned} \Psi^\dagger(x) \Psi^\dagger(x') \Psi(x') \Psi(x) &\rightarrow \rho(x, x) \Psi^\dagger(x') \Psi(x') + \rho(x', x') \Psi^\dagger(x) \Psi(x) \\ &\pm \rho(x, x') \Psi^\dagger(x') \Psi(x) \pm \rho(x', x) \Psi^\dagger(x) \Psi(x'). \end{aligned} \quad (4.2)$$

As throughout this work, the upper signs are referring to bosons and the lower ones indicate fermions. The effective Hartree-Fock Hamiltonian is then given by

$$\begin{aligned} H^{\text{eff}} &= \iint dx dx' \Psi^\dagger(x) \{ h^0(x) \delta(x - x') + \Sigma^{\text{HF}}(x, x') \} \Psi(x') \\ &= \iint dx dx' \Psi^\dagger(x) \left\{ \left[h^0(x) + \int d\bar{x} \rho(\bar{x}, \bar{x}) w(\bar{x}, x) \right] \delta(x - x') \pm \rho(x', x) w(x', x) \right\} \Psi(x'), \end{aligned} \quad (4.3)$$

where the self-energy expression $\Sigma^{\text{HF}}(x, x')$ is identical to inclusion of both first order diagrams of Fig. 3.1. The second term on the r.h.s. of (4.3) is the Hartree contribution whereas the third term denotes the exchange potential the sign of which depends on the particle species. Expressing the field operators in a single-particle basis, i.e. $\Psi(x) = \sum_k \sum_{\sigma_k} c_k^{\sigma_k} \phi_k(x) \chi(\sigma_k)$ where $\chi(\sigma_k)$ denotes a spin wave function with degrees of freedom σ_k , one arrives at

$$H^{\text{eff}} = \sum_{kl} \sum_{\sigma_k \sigma_l} \left(H_{kl}^{\text{eff}} \right)^{\sigma_k \sigma_l} (c_k^{\sigma_k})^\dagger c_l^{\sigma_l}, \quad (4.4)$$

with definitions

$$\left(H_{ij}^{\text{eff}} \right)^{\sigma_i \sigma_j} = (h_{ij}^0)^{\sigma_i \sigma_j} + \sum_{kl} \sum_{\sigma_k \sigma_l} \left(w_{kl,ij}^{\sigma_k \sigma_l, \sigma_i \sigma_j} \pm w_{kj,il}^{\sigma_k \sigma_j, \sigma_i \sigma_l} \right) \rho_{kl}^{\sigma_k \sigma_l}, \quad (4.5)$$

$$\rho_{kl}^{\sigma_k \sigma_l} = \langle (c_k^{\sigma_k})^\dagger c_l^{\sigma_l} \rangle \quad (4.6)$$

$$(h_{ij}^0)^{\sigma_i \sigma_j} = h_{ij}^0 \delta_{\sigma_i \sigma_j} = \delta_{\sigma_i \sigma_j} \int dx \phi_i^*(x) h^0(x) \phi_j(x), \quad (4.7)$$

$$w_{ij,kl}^{\sigma_i \sigma_j, \sigma_k \sigma_l} = \delta_{\sigma_i \sigma_j} \delta_{\sigma_k \sigma_l} w_{ij,kl} = \delta_{\sigma_i \sigma_j} \delta_{\sigma_k \sigma_l} \iint dx dx' \phi_i^*(x) \phi_k^*(x') w(x, x') \phi_j(x) \phi_l(x'). \quad (4.8)$$

With the restriction to spinless or spin-polarized systems with a single spin-projection only, the effective Hamiltonian (4.5) essentially simplifies to

$$H_{ij}^{\text{eff}} = h_{ij}^0 + \sum_{kl} (w_{kl,ij} \pm w_{kj,il}) \rho_{kl}. \quad (4.9)$$

In order to calculate the Hartree-Fock orbitals (HFO), i.e. to compute an orthonormal set of single-particle orbitals $\{\Phi_m(x)\}$ obeying $\langle \Phi_i | H^{\text{eff}} - \epsilon | \Phi_j \rangle = 0$, one now can expand these in terms of natural basis functions $\phi_n(x)$ and solve the resulting generalized eigenvalue problem (GEP)

$$\sum_k \left(H_{ik}^{\text{eff}} - \epsilon_j O_{ik} \right) A_{kj} = 0, \quad \Phi_m(x) = \sum_n A_{nm} \phi_n(x), \quad (4.10)$$

where $O_{ij} = \langle \phi_i | \phi_j \rangle$ is the overlap matrix, ϵ_j denotes the energy eigenvalue of the Hartree-Fock orbital j , and A_{ij} is the component i of the corresponding eigenvector. The set of Eqs. (4.10) are thereby referred to as the Roothaan-Hall equations in the literature [59], and their solution determines the orbitals $\Phi_m(s)$ which later will serve to expand the Green's functions.

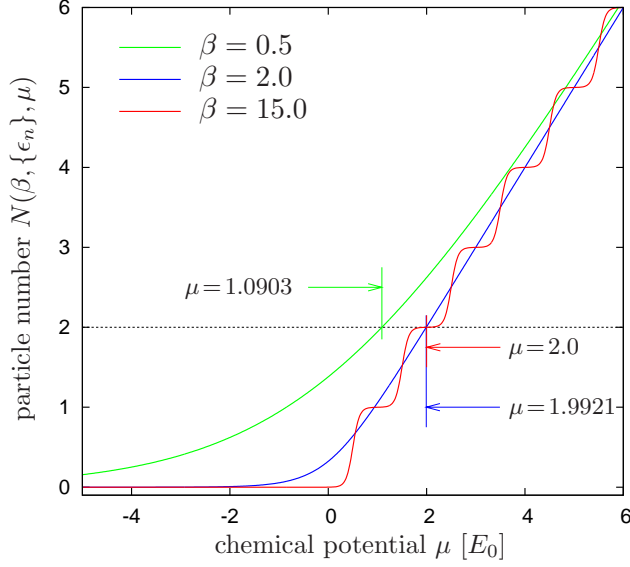


Figure 4.1: Computation of the chemical potential according to Eq. (4.12) for a fermionic system: Particle number $N(\beta, \{\epsilon_n\}, \mu)$ in dependence on the chemical potential μ for three different inverse temperatures as indicated within the figure. For demonstration, the energy eigenvalues are assumed to be the 1D harmonic oscillator energies $\epsilon_n = n + \frac{1}{2}$. For $\beta \rightarrow \infty$, it is $\mu = \frac{1}{2}(\epsilon_{m+1} - \epsilon_m)$ with m labeling the last occupied state. The calculated values of μ refer to $N = 2$. μ is given in units of $E_0 = \hbar\Omega$ and β in $\beta_0 = E_0^{-1}$.

Due to the intrinsic coupling of the grand canonical density matrix and the effective Hamiltonian, the generalized eigenvalue problem cannot be treated directly but has to be solved to self-consistency by an iteration procedure—self-consistent field procedure [57]. As an overview for practical computation, the following enumeration summarizes the important steps to be processed:

- i. Pick a set of n_b (in general non-orthogonal) single-particle orbitals $\phi_n(x)$.
- ii. Analytically or numerically precompute matrix elements h_{ij}^0 and $w_{ij,kl}$.
- iii. Calculate the Hamiltonian H_{ij}^{eff} as given in Eq. (4.9) with an initial guess for ρ_{ij} .
- iv. Solve the generalized eigenvalue problem

$$\sum_k \left(H_{ik}^{\text{eff}} - \epsilon_j O_{ik} \right) A_{kj} = 0 \quad \Leftrightarrow \quad \mathbf{H}^{\text{eff}} \mathbf{A} = \epsilon \mathbf{O} \mathbf{A}, \quad (4.11)$$

requiring the normalization $\mathbf{A}^\dagger \mathbf{O} \mathbf{A} = \mathbf{1}$. The corresponding (numerical) strategy is the following: First, one performs a basis transformation to an orthogonal basis set in order to make \mathbf{O} vanish. Then, one simply has to diagonalize the matrix \mathbf{H}^{eff} .

- v. Determine the chemical potential μ by requiring the total particle number N to be

$$N(\beta, \{\epsilon_k\}, \mu) = \sum_k f(\epsilon_k - \mu), \quad (4.12)$$

where $f(\epsilon_k - \mu) = 1/(\exp(\beta[\epsilon_k - \mu]) \pm 1)$ denotes the statistical distribution function—either a Fermi-Dirac or Bose-Einstein distribution. Fig. 4.1 illustrates the μ -dependence of the particle number for noninteracting harmonically trapped fermions. To be numerically computed are the intersections of the curves with the straight lines of $N = \text{const}$.

- vi. Calculate the new density matrix ρ_{ij} and new total energy E_{tot} by

$$\rho_{ij} = \sum_k A_{ik} f(\epsilon_k - \mu) A_{jk}^*, \quad (4.13)$$

$$E_{\text{tot}} = \frac{1}{2} \sum_k \epsilon_k f(\epsilon_k - \mu) + \frac{1}{2} \sum_{ij} h_{ij}^0 \rho_{ji}. \quad (4.14)$$

- vii. Return to (iii) with updated density matrix ρ_{ij} as long as the total energy is changing, i.e. as long as $|E_{\text{tot}}^{(\nu)} - E_{\text{tot}}^{(\nu-1)}| > \Delta E_{\text{tot}}$ where ν labels the iteration cycle and ΔE_{tot} is the claimed accuracy.

Although there is no general guarantee that this iterative scheme will converge it is known to do well [57] for small basis sets and simple geometries. Improvements such as extrapolation of $\mathbf{H}^{\text{eff}}(\nu)$ or damping of oscillatory behaviors in ρ are straightforward to implement but have not been found necessary concerning the investigations of trapped fermions in Chaps. 5 and 6.

However, there is something to note in addition. To avoid an unphysical result it is—besides the convergence of total energy—important to ensure that enough basis functions are being provided so that the number of basis functions n_b has only little effect on the total energy.

4.1.1. Hartree-Fock eigenvalues and convergence properties

Together with the density matrix and the eigenvectors, the eigenvalues following from Eq. (4.10) are relevant quantities and will lead to the definition of the Hartree-Fock Green's function in the next section. Fig. 4.2 (a) shows how these depend on the number n_b of used basis functions. Thereby, the self-consistent procedure has been applied to the system described by the Hamiltonian given in Sect. 1.2 which is fully characterized by the particle number, the inverse temperature and the coupling parameter, i.e. by (N, β, λ) . Due to the repulsive interaction potential all the HF eigenvalues or levels ϵ_k are up-shifted in comparison to the energies of the harmonic oscillator with $\epsilon_k^0 = k + 1/2$. There is only a slight change in the lowest energy levels when using more or less basis functions (if $n_b > N$), but typically up to four or five of the highest levels are computed to low accuracy—these should be disregarded in further calculations.

Also presented are the energy level spacings, i.e. $\Delta\epsilon_k = \epsilon_{k+1} - \epsilon_k$, which are (except close to the chemical potential region) less than $\Delta\epsilon_k^0 = 1$. This behavior is consistent with the local increase of the effective Hartree-Fock potential becoming flatter compared to the parabolic potential. For large quantum numbers $k \gg 1$ the HF eigenvalues should approach the energies ϵ_k^0 of the noninteracting system, but this tendency cannot be well extracted from Fig. 4.2 (a).

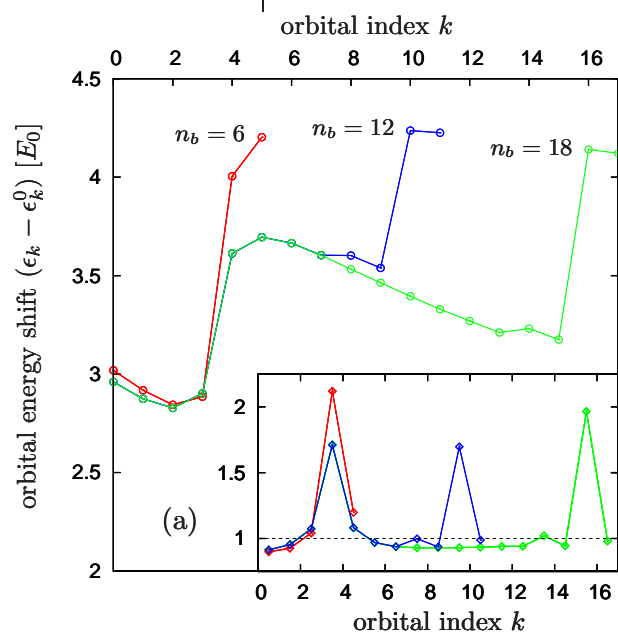
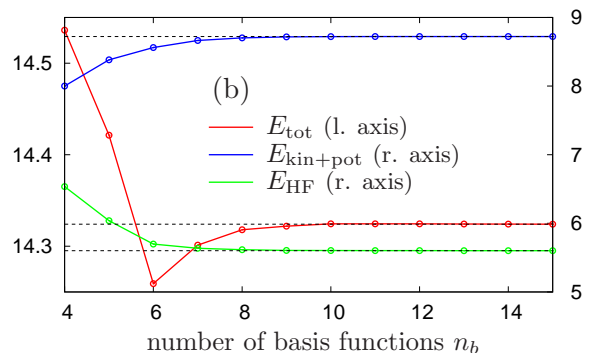


Figure 4.2: (a) HFO energies ϵ_k as obtained from Eq. (4.10) for $N = 4$ trapped fermions at $\beta = 2.0$ —coupling parameter $\lambda = 1.5$, $a = 0.1$. Displayed are the differences $(\epsilon_k - \epsilon_k^0)$ for calculations with different numbers of basis functions. ϵ_k^0 denotes the ideal eigenvalue $\epsilon_k^0 = k + \frac{1}{2}$. Inset: Energy level spacing in units of E_0 . (b) Convergence of different energy contributions.



In Fig. 4.2 (b), the total Hartree-Fock energy—split up into the single-particle contribution $E_{\text{kin+pot}}$ and the interaction part E_{HF} —is analyzed for different sizes of the basis set. As can be seen good convergence is already obtained for $n_b \gtrsim 10$. Thus, it is possible to restrict oneself to a relatively small basis although one has to note that higher temperatures and an increased coupling parameter will have an essential effect on the minimal n_b .

Besides the total and orbital energies there are more objects that can be checked to ensure a correct computation. Since the calculation starts with an initial guess for the density matrix it is a good idea to prove the properties of the real density matrix, e.g. its properties of being positive definite and symmetric. Further, the sum over the diagonal elements ρ_{kk} must yield the particle number N with acceptable error and the computation of $\xi = \text{Tr}\{\rho^2\}$ in addition allows to distinguish if the particle ensemble is in a pure ($\xi = N$) or mixed state ($\xi > N$).

4.1.2. Hartree-Fock orbital (HFO) representation

If one is interested in doing computations within the basis built up from the Hartree-Fock orbitals, all quantities related to the natural basis set $\phi_k(x)$ have to be merged into the HFO representation according to the orthogonal transformation $\mathbf{O}^{\text{HFO}} = \mathbf{A}^\dagger \mathbf{O} \mathbf{A}$, where \mathbf{A} denotes the matrix incorporating all HF eigenvectors in its columns and \mathbf{O} is defined in the natural basis. Recalling the expansion of (4.10), $\Phi_m(x) = \sum_n A_{nm} \phi_n(x)$, for all single-particle observables or operators O_{kl} in the natural basis holds

$$\begin{aligned} O_{ij}^{\text{HFO}} &= \langle \Phi_i | O | \Phi_j \rangle = \sum_{kl} A_{ki}^* A_{lj} \int dx \phi_k^*(x) O(x) \phi_l(x) \\ &= \sum_{kl} A_{ki}^* O_{kl} A_{lj}. \end{aligned} \quad (4.15)$$

For the single-particle energy, as the sum over kinetic and potential energy ($h_{ij}^0 = t_{ij} + v_{ij}$), it is thereby convenient to subtract the chemical potential, i.e. one transforms according to

$$(h_{ij}^0)^{\text{HFO}} = \left(\sum_{kl} A_{ki}^* h_{kl}^0 A_{lj} \right) - \delta_{ij} \mu. \quad (4.16)$$

Another special case is the density matrix ρ_{ij} which by definition transforms into a diagonal matrix containing the occupation numbers of the HF orbitals. This property serves as a sensitive test for the correctness of the eigenvectors in matrix \mathbf{A} .

Furthermore, the two-electron integrals $w_{kl,mn}$ transform in the same way as the single-particle quantities and one obtains in detail

$$w_{ab,cd}^{\text{HFO}} = \sum_{klmn} [A_{ka} A_{lb}^*]^* w_{kl,mn} [A_{mc}^* A_{nd}]. \quad (4.17)$$

4.2. Discretization of the Hartree-Fock Green's function

Using the set of Hartree-Fock eigenvalues obtained in the preceding section the corresponding Hartree-Fock Green's function, denoted $\mathbf{g}^0(\tau)$ with $\tau \in [-\beta, 0]$ (see Sect. 3.3.3), is straightforwardly accessed. It is the (equilibrium) Matsubara Green's function with respect to the first order self-energy contributions only. Since it obeys the uncorrelated Dyson equation (recall Eq. (3.75))

$$\begin{aligned} -\partial_\tau g_{ij}^0(\tau) - \sum_k (h_{ik}^0 + \Sigma_{ik}^0) g_{kj}^0(\tau) &= \delta_{ij} \delta(\tau), \\ \Leftrightarrow [-\partial_\tau - \mathbf{h}^0 - \mathbf{\Sigma}^0] \mathbf{g}^0(\tau) &= \delta(\tau), \end{aligned} \quad (4.18)$$

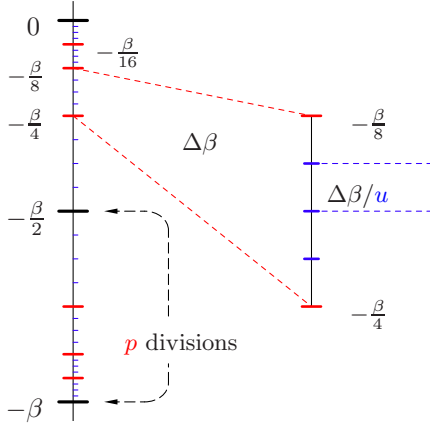


Figure 4.3: Uniform power-mesh (UPM) on which the imaginary-time Green's function (and the corresponding self-energy) is represented. The τ -interval $[-\beta, 0]$ is divided according to the parameters u and p which lead to a grid being dense around the end-points $\tau = -\beta$ and $\tau = 0$. Here, one has chosen $u = p = 4$.

where \mathbf{h}^0 refers to the single-particle Hamiltonian and Σ^0 is the HF self-energy. Generally all quantities are now and in the remainder of this chapter in the HFO representation. Since, the eigenvalues $\{\epsilon_k\}$ diagonalize the matrix $(\mathbf{h}^0 + \Sigma^0)$, the Hartree-Fock Green's function can directly be constructed as diagonal matrix on the HFO, i.e.

$$g_{ij}^0(\tau) = \delta_{ij} \exp(\tau[\epsilon_i - \mu]) f(\epsilon_i - \mu) = \delta_{ij} \frac{e^{\tau(\epsilon_i - \mu)}}{e^{\beta(\epsilon_i - \mu)} \pm 1}. \quad (4.19)$$

That this definition is a correct solution of Eq. (4.18) is easily verified. If $\mathbf{g}^0(\tau)$ is a zero-temperature HF Green's function then $g_{ii}^0(0^-) = n_i$ equals 1 if orbital i is occupied ($\epsilon_i - \mu < 0$) and 0 otherwise. In addition, one always finds that $g_{ii}^0(-\beta^+) = 1 - n_i$ and $g_{ii}^0(0^+) - g_{ii}^0(0^-) = -g_{ii}^0(-\beta^+) - g_{ii}^0(0^-) = -1$ as well as $\mathbf{g}^0(\tau)$ being anti-periodic in β .

In order to perform numerical computations that include $\mathbf{g}^0(\tau)$ —in particular to solve the sophisticated correlated Dyson equation (3.74) in the next section—the continuous time-interval $[-\beta, 0]$ has to be discretized. Due to the specific time-dependence of the Green's function elements in Eq. (4.19)—notice that they are strongly peaked at the boundaries of the τ -interval—it is inconvenient to represent them on an evenly spaced time-grid. Instead, it is advantageous to introduce a grid which is dense around the end-points $\tau = 0$ and $\tau = -\beta$. Widely used in this sense [48, 60] is the uniform power-mesh (UPM) which is defined by three parameters: the inverse temperature β and two grid parameters u and p . As is illustrated in Fig. 4.3, such a grid is built up from p quadratic divisions of the half-intervals $[-\beta, -\beta/2]$ and $[-\beta/2, 0]$ whereby each part itself contains u evenly spaced subdivisions. The main properties of this grid are the following:

- i. The total number of points on the grid is $M = 2up + 1$.
- ii. For the largest mesh-spacing in the center around $\tau = -\beta/2$ one obtains $\Delta\tau_{\max} = \beta/(4u)$.
- iii. The smallest mesh-spacing at the end-points $\tau \in \{0, -\beta\}$ is given by $\Delta\tau_{\min} = \frac{1}{2}\beta/(2^{p-1}u)$.

Computations on the UPM are not more difficult than on an even-spaced grid. However, care is advisable when evaluating differences $\Delta\tau = \tau_1 - \tau_2$ (where τ_1 and τ_2 are grid points) since $\Delta\tau$ not necessarily corresponds to an existing point on the grid. To this end, interpolations should be used to compute general quantities $f(\Delta\tau)$.

Moreover, also the correlated Green's function and the explicitly τ -dependent (equilibrium) self-energies which arise in second or higher order perturbative expansion are well represented on the uniform power-mesh. Numerically, all relevant quantities are thus to be implemented

as three-dimensional arrays $a[i][j][q]$, where besides both matrix indices $\{i, j\}$ the discrete time argument q appears.

In the following section the correlated Dyson equation (3.74) will be solved on this uniform power-mesh while the Hartree-Fock Green's function of Eq. (4.19) serves as the reference state in an iteration procedure.

4.3. Solving the Dyson equation

In this section, the correlated Dyson equation (3.74) of Chap. 3 for the (equilibrium) Matsubara Green's function $\mathbf{g}^M(\tau)$ will be prepared for an adequate numerical treatment. It is a standard procedure [15, 48] to rewrite the equation of motion in a form suitable for a self-consistent iterative solution. The reformulation is thereby not restricted to a finite order in the perturbative self-energy expansion. Recall the Dyson equation in its matrix form

$$\begin{aligned} -\partial_\tau g_{ij}^M(\tau) - \sum_k h_{ik}^0 g_{kj}^M(\tau) &= \delta_{ij} \delta(\tau) + \int_0^\beta d\bar{\tau} \sum_k \Sigma_{ik}^M(\tau - \bar{\tau}) g_{kj}^M(\bar{\tau}), \quad (4.20) \\ \Leftrightarrow \quad [-\partial_\tau - \mathbf{h}^0] \mathbf{g}^M(\tau) &= \delta(\tau) + \int_0^\beta d\bar{\tau} \Sigma^M(\tau - \bar{\tau}) \mathbf{g}^M(\bar{\tau}), \end{aligned}$$

with $\Sigma^M(\tau)$ being the full Matsubara self-energy.

The reference or starting system now to be applied to Eq. (4.20) will, in the present calculation, be the Hartree-Fock Green's function with the time-independent self-energy as it is given in the last section, Eqs. (4.18) and (4.19). Since the Green's functions are expanded in terms of the Hartree-Fock orbitals this is the natural choice. There exist other possibilities as discussed in [48] which, however, use orbitals and respective Green's functions originating from LDA (local density approximation) or DFT calculations.

Integrating Eq. (4.20) over $\int_0^\beta d\tau \dots \tilde{\mathbf{g}}^0(\bar{\tau} - \tau)$, where $\bar{\tau}$ is restricted to be positive ranging from 0 to $+\beta$, one obtains

$$\begin{aligned} &\int_0^\beta d\tau \{ [-\partial_\tau - \mathbf{h}^0] \mathbf{g}^M(\tau) \} \mathbf{g}^0(\bar{\tau} - \tau) \quad (4.21) \\ &= \mathbf{g}^0(\bar{\tau}) + \int_0^\beta d\tau \int_0^\beta d\tau' (\Sigma^M(\tau - \tau') \mathbf{g}^M(\tau')) \mathbf{g}^0(\bar{\tau} - \tau). \end{aligned}$$

Further, using the identity

$$\partial_\tau (\mathbf{g}^M(\tau) \mathbf{g}^0(\bar{\tau} - \tau)) = \mathbf{g}^0(\bar{\tau} - \tau) \cdot \partial_\tau \mathbf{g}^M(\tau) - \mathbf{g}^M(\tau) \cdot \partial_{(\bar{\tau} - \tau)} \mathbf{g}^0(\bar{\tau} - \tau), \quad (4.22)$$

the l.h.s. of Eq. (4.21) can be evaluated by partial integration to

$$\begin{aligned} &\int_0^\beta d\tau \{ [-\partial_\tau - \mathbf{h}^0] \mathbf{g}^M(\tau) \} \mathbf{g}^0(\bar{\tau} - \tau) \quad (4.23) \\ &= [-\mathbf{g}^M(\tau) \mathbf{g}^0(\bar{\tau} - \tau)]_0^\beta + \int_0^\beta d\tau [-\partial_{(\bar{\tau} - \tau)} \mathbf{g}^0(\bar{\tau} - \tau) - \mathbf{h}^0 \mathbf{g}^0(\bar{\tau} - \tau)] \mathbf{g}^M(\tau) \\ &= \mathbf{g}^M(\bar{\tau}) + \int_0^\beta d\tau \Sigma^0 \mathbf{g}^0(\bar{\tau} - \tau) \mathbf{g}^M(\tau). \end{aligned}$$

To get the last equality, the equation of motion (4.18) for the reference function $\mathbf{g}^0(\tau)$ from Sect. 4.3 has been used and the anti-periodicity property of the Matsubara Green's function is responsible for the vanishing term

$$[-\mathbf{g}^M(\tau) \mathbf{g}^0(\bar{\tau} - \tau)]_0^\beta = -\mathbf{g}^M(\beta) \mathbf{g}^0(\bar{\tau} - \beta) + \mathbf{g}^M(0) \mathbf{g}^0(\bar{\tau}) = 0. \quad (4.24)$$

Collecting expressions (4.21) and (4.23), the Dyson equation takes the integral form [15]

$$\begin{aligned} \mathbf{g}^M(\bar{\tau}) &= \mathbf{g}^0(\bar{\tau}) + \int_0^\beta d\tau \int_0^\beta d\tau' \mathbf{g}^0(\bar{\tau} - \tau) [\boldsymbol{\Sigma}^M(\tau - \tau') - \delta(\tau - \tau') \boldsymbol{\Sigma}^0] \mathbf{g}^M(\tau') \\ &= \mathbf{g}^0(\bar{\tau}) + \int_0^\beta d\tau \int_0^\beta d\tau' \mathbf{g}^0(\bar{\tau} - \tau) \boldsymbol{\Sigma}^c[\mathbf{g}^{M/0}](\tau - \tau') \mathbf{g}^M(\tau'), \end{aligned} \quad (4.25)$$

where the reference (Hartree-Fock) and Matsubara self-energy—both functionals of their respective Green's functions—have been summarized in $\boldsymbol{\Sigma}^c[\mathbf{g}^{M/0}](\tau) = \boldsymbol{\Sigma}^M(\tau) - \delta(\tau) \boldsymbol{\Sigma}^0$. The iteration cycle now starts with $\mathbf{g}^M(\tau) = \mathbf{g}^0(\tau)$ for which the self-energy $\boldsymbol{\Sigma}^M(\tau)$ is calculated. Fixing this self-energy the Dyson equation (4.25) is solved for $\mathbf{g}^M(\tau)$. Then a new self-energy is computed, and the process is repeated until convergence. Obviously, this procedure is similar to the strategy of solving the Roothaan-Hall equations in Sect. 4.1—however, the self-energy is here generally included to an arbitrary order.

To simplify the numerical handling even further, the discretization of the time-interval $[-\beta, 0]$ is used in the following to transform Eq. (4.25) into systems of linear equations: Assuming $\tau^{(p)}$ to be the points on the uniform power-mesh $\Pi = \{\tau^{(0)} = 0, \tau^{(1)}, \dots, \tau^{(m)} = -\beta\}$ and using $g_{ij}^0(\tau) =: \delta_{ij} g_i^0(\tau)$, one can write

$$\begin{aligned} &\delta_{ij} g_i^0(\tau^{(p)}) \\ &= g_{ij}^M(\tau^{(p)}) + \sum_k \int_0^\beta d\tau_2 \left[\int_0^\beta d\tau_1 g_i^0(\tau^{(p)} - (\tau_1 - \beta)) \Sigma_{ik}^c(\tau_1 - \tau_2) \right] g_{kj}^M(\tau_2) \\ &= g_{ij}^M(\tau^{(p)}) + \sum_k \int_{-\beta}^0 d\tau_2 \left[\int_0^\beta d\tau_1 g_i^0(\tau^{(p)} - (\tau_1 - \beta)) \Sigma_{ik}^c(\tau_1 - (\tau_2 + \beta)) \right] g_{kj}^M(\tau_2 + \beta) \\ &\approx g_{ij}^M(\tau^{(p)}) - \sum_k \sum_{q=0}^m \frac{\Delta\tau^{(q)}}{2} \left[\int_0^\beta d\tau_1 g_i^0(\tau^{(p)} - (\tau_1 - \beta)) \Sigma_{ik}^c(\tau_1 - (\tau^{(q)} + \beta)) \right] g_{kj}^M(\tau^{(q)}) \\ &= \sum_k \sum_{q=0}^m \left[\delta_{ik} \delta_{pq} - \frac{\Delta\tau^{(q)}}{2} F_{ik}(\tau^{(p)}, \tau^{(q)}) \right] g_{kj}^M(\tau^{(q)}), \end{aligned} \quad (4.26)$$

where one has approximated the integral $\int \dots d\tau_2$ by a sum over the discrete time-grid Π . The convolution integrals $F_{ij}(\cdot, \cdot)$ have been defined through

$$\begin{aligned} F_{ij}(\tau^{(p)}, \tau^{(q)}) &= \int_0^\beta d\tau_1 g_i^0(\tau^{(p)} - (\tau_1 - \beta)) \Sigma_{ij}^c(\tau_1 - (\tau^{(q)} + \beta)) \\ &= \int_{-\beta}^0 d\tau g_i^0(\tau^{(p)} - \tau) \Sigma_{ij}^c(\tau - \tau^{(q)}). \end{aligned} \quad (4.27)$$

Further, the introduced time step-size $\Delta\tau^{(q)}$ in (4.26) is positive by definition

$$\Delta\tau^{(q)} = \begin{cases} \tau^{(0)} - \tau^{(1)}, & q = 0 \\ \tau^{(m-1)} - \tau^{(m)}, & q = m \\ \tau^{(q-1)} - \tau^{(q+1)}, & \text{otherwise} \end{cases}, \quad (4.28)$$

and corresponds to the replacement of integrals in accordance with the standard (trapezoid) formula

$$\int_{-x_0}^0 dx f(x) \approx \sum_{k=0}^m \frac{\Delta x^{(k)}}{2} f(x^{(k)}). \quad (4.29)$$

For fixed index j , Eq. (4.26) can now easily be reinterpreted as a set of linear equations. Combining the orbital index i and the time-grid index p into a single index Q_1 one has

$$\mathbf{A} \cdot \mathbf{x}^{(j)} = \mathbf{b}^{(j)}, \quad \sum_{Q_2} A_{Q_1 Q_2} \cdot x_{Q_2}^{(j)} = b_{Q_1}^{(j)}, \quad (4.30)$$

with expressions

$$A_{Q_1 Q_2} = A_{(ip)(kq)} = \delta_{ik} \delta_{pq} - \frac{\Delta\tau^{(q)}}{2} F_{ik}(\tau^{(p)}, \tau^{(q)}), \quad (4.31)$$

$$x_{Q_2}^{(j)} = x_{(kq)}^{(j)} = g_{kj}^M(\tau^{(q)}), \quad (4.32)$$

$$b_{Q_1}^{(j)} = b_{(ip)}^{(j)} = \delta_{kj} g_i^0(\tau^{(p)}). \quad (4.33)$$

Thus, the correlated Dyson equation has been mapped onto a linear algebra problem where one iteratively searches for the self-consistent vectors $\mathbf{x}^{(j)}$. Each iteration cycle will consequently contain the following three steps:

- i. Computation of the convolution integrals $F_{ik}(\cdot, \cdot)$ for all time-points $\tau^{(p)}$ and $\tau^{(q)}$. Note, that the self-energy $\Sigma^c(\tau)$ therein depends on the time-dependent Matsubara Green's function, i.e. on all actual $\mathbf{x}^{(j)}$.
- ii. Determination of the coefficient matrix $\mathbf{A}(F)$. The inhomogeneities $\mathbf{b}^{(j)}$ are stationary and need to be computed only once.
- iii. Numerical solution of the linear system $\mathbf{A} \cdot \mathbf{x}^{(j)} = \mathbf{b}^{(j)}$ for each existing index j .

The convergence of the vectors $\mathbf{x}^{(j)}$ can be established for example by taking the norm over all components and all grid points, i.e.

$$\Delta \mathbf{x}^{(j)} = \left\| \mathbf{x}^{(j, \nu+1)} - \mathbf{x}^{(j, \nu)} \right\| := \sum_i \sum_{p=0}^m \left| x_{(ip)}^{(j, \nu+1)} - x_{(ip)}^{(j, \nu)} \right|, \quad (4.34)$$

where ν labels the current iteration. If the norm $\Delta \mathbf{x}^{(j)}$ stays below a given bound for all indices j the iteration procedure can be truncated and the Matsubara Green's function—being represented on the uniform power-mesh Π —follows to be $g_{ij}^M(\tau^{(p)}) = x_{(ip)}^{(j)}$.

To conclude this section, the definition (4.27) is recalled and written out in detail:

$$\begin{aligned} F_{ij}(\tau^{(p)}, \tau^{(q)}) &= \int_{-\beta}^0 d\tau g_i^0(\tau^{(p)} - \tau) \Sigma_{ij}^c(\tau - \tau^{(q)}) \\ &= \int_{-\beta}^0 d\tau g_i^0(\tau^{(p)} - \tau) \left[\Sigma_{ij}^{\text{corr}}(\tau - \tau^{(q)}) + \delta(\tau - \tau^{(q)}) (\Sigma_{ij}^{\text{HF}} - \Sigma_{ij}^0) \right] \\ &= g_i^0(\tau^{(p)} - \tau^{(q)}) (\Sigma_{ij}^{\text{HF}} - \Sigma_{ij}^0) + \int_{-\beta}^0 d\tau g_i^0(\tau^{(p)} - \tau) \Sigma_{ij}^{\text{corr}}(\tau - \tau^{(q)}) \\ &\approx g_i^0(\tau^{(p)} - \tau^{(q)}) (\Sigma_{ij}^{\text{HF}} - \Sigma_{ij}^0) + \sum_{s=0}^m \frac{\Delta\tau^{(s)}}{2} g_i^0(\tau^{(p)} - \tau^{(s)}) \Sigma_{ij}^{\text{corr}}(\tau^{(s)} - \tau^{(q)}). \end{aligned} \quad (4.35)$$

Thereby, the Matsubara Green's function has been split into the time-independent Hartree-Fock part and the correlation part according to

$$\Sigma^M[\mathbf{g}^M](\tau) = \delta(\tau) \Sigma^{\text{HF}}[\mathbf{g}^M(0^-)] + \Sigma^{\text{corr}}[\mathbf{g}^M(\tau)](\tau), \quad (4.36)$$

and in the last equality the integral $\int_{-\beta}^0 \dots d\tau$ has been replaced by a sum over the uniform power-mesh.

The numerical computation of the convolution integrals is—besides the calculation of the different self-energies—rather involved. Although all the self-energy matrices are symmetric any symmetry properties do not hold for the integrals F_{ij} , and in addition the evaluation of differences $\tau_1 - \tau_2$ on the UPM needs to be carefully implemented as discussed in Sect. 4.2. For this reasons the determination of $F_{ij}(\tau^{(p)}, \tau^{(q)})$ will be the most time-consuming part in the actual calculation concerning the Dyson equation.

4.3.1. Self-energy contributions

For completeness, the different self-energy expressions entering the correlated Dyson equation (4.25) in second Born approximation are here summarized once again:

- The static reference self-energy Σ^0 follows from the density matrix ρ of Eq. (4.13)—more precisely after transformation of ρ into the HFO representation. It is

$$\Sigma_{ij}^0 = \sum_{kl} (w_{kl,ij} \pm w_{kj,il}) \rho_{kl}. \quad (4.37)$$

- The static Hartree-Fock self-energy Σ^{HF} appears as a functional of the correlated density $\rho_{ij}^M = g_{ij}^M(0^-)$, i.e.

$$\Sigma_{ij}^{\text{HF}} = \sum_{kl} (w_{kl,ij} \pm w_{kj,il}) \rho_{kl}^M. \quad (4.38)$$

- Each part of the dynamic (τ -dependent) self-energy $\Sigma^{\text{corr}}(\tau)$ contains in second Born approximation two interaction lines and three propagators. In notational detail, it is

$$\begin{aligned} \Sigma_{ij}^{\text{corr}}(\tau) &= - \sum_{klmnr} w_{ik,ms} (w_{lj,rn} \pm w_{nj,rl}) g_{kl}^M(\tau) g_{mn}^M(\tau) g_{rs}^M(-\tau) \\ &= \sum_{kl} g_{kl}^M(\tau) \sum_{mn} g_{mn}^M(\tau) \sum_{rs} g_{rs}^M(-\tau - \beta) w_{ik,ms} (w_{lj,rn} \pm w_{nj,rl}). \end{aligned} \quad (4.39)$$

Assuming negative τ -values only, all time arguments on the r.h.s. of Eq. (4.39) are within the discretized interval $[-\beta, 0]$. Exactly in this way the dynamic self-energy is implemented.

All the interaction matrix elements $w_{ab,cd}$ are thereby defined in terms of the Hartree-Fock orbitals (HFO), $\Phi_k(x) = \sum_l A_{lk} \phi_l(x)$, i.e. according to Sect. 4.1.2

$$\begin{aligned} w_{ab,cd} &= \iint dx dx' \Phi_a^*(x) \Phi_c^*(x') w(x, x') \Phi_b(x) \Phi_d(x) \\ &= \iint dx dx' \sum_{klmn} (A_{ka}^* \phi_k^*(x)) (A_{mc}^* \phi_m^*(x')) w(x, x') (A_{lb} \phi_l(x)) (A_{nd} \phi_n(x')) \\ &= \iint dx dx' \sum_{klmn} [A_{ka} A_{lb}^*] \phi_k^*(x) \phi_m^*(x') w(x, x') \phi_l(x) \phi_n(x') [A_{mc}^* A_{nd}]. \end{aligned} \quad (4.40)$$

4.3.2. Computation of relevant energies

Besides the determination of other equilibrium properties from the Matsubara Green's function, such as distribution function or density which will be subject of investigation in Chap. 5, the

computation of relevant energies contributing to the total energy is an important task. In particular, it is interesting to compare with the Hartree-Fock Green's function which will reveal the effects of including the particle collisions. To this end the different energies are presented in the following in terms of the correlated Green's function matrix $\mathbf{g}^M(\tau)$.

Although there are many different ways to extract the total energy from the Green's function, here the straightforward definition given in Refs. [15, 54] has been found useful. In the basis representation of the Green's function it reads

$$E_{\text{tot}} = \text{Tr}\{\mathbf{h}^0 \mathbf{g}^M(0^-)\} + \frac{1}{2} \int_0^\beta d\tau \text{Tr}\{\boldsymbol{\Sigma}^M(-\tau) \mathbf{g}^M(\tau)\} + \mu N, \quad (4.41)$$

where $\text{Tr}\{\dots\}$ indicates the trace, μ is the chemical potential and N is the total particle number. The first term on the r.h.s. of (4.41) containing the matrix \mathbf{h}^0 belongs to the single-particle Hamiltonian and the second term gives the interaction energy $E_{\text{int}} = E_{\text{HF}} + E_{\text{corr}}$ in the particular applied self-energy approximation. Thus, one can distinguish:

- i. **Single-particle energy** with $\mathbf{h}^0 = \mathbf{t} + \mathbf{v}$ originating from Eq. (4.16):

$$E_{\text{single}} = \text{Tr}\{\mathbf{h}^0 \mathbf{g}^M(0^-)\} + \mu N, \quad (4.42)$$

- ii. **Hartree-Fock energy** with the self-energy being local in time, i.e. $\boldsymbol{\Sigma}^{\text{HF}}(\tau) = \delta(\tau) \boldsymbol{\Sigma}^{\text{HF}}$. The integral in Eq. (4.41) can be taken with help of the delta function and one obtains

$$E_{\text{HF}} = \frac{1}{2} \text{Tr}\{\boldsymbol{\Sigma}^{\text{HF}} \mathbf{g}^M(0^-)\}. \quad (4.43)$$

- iii. **Correlation energy** with the explicitly time-dependent self-energy $\boldsymbol{\Sigma}^{\text{corr}}(\tau)$:

$$\begin{aligned} E_{\text{corr}} &= \frac{1}{2} \int_0^\beta d\tau \text{Tr}\{\boldsymbol{\Sigma}^{\text{corr}}(-\tau) \mathbf{g}^M(\tau)\} \\ &= -\frac{1}{2} \int_0^\beta d\tau \text{Tr}\{\boldsymbol{\Sigma}^{\text{corr}}(-\tau) \mathbf{g}^M(\tau - \beta)\}. \end{aligned} \quad (4.44)$$

For the system already used for demonstration in Sect. 4.1.1, now the Dyson equation has been solved in second Born approximation, and Fig. 4.4 below shows the dependence of the resulting total energy on different time-mesh parameters (u, p). As a function of total number of

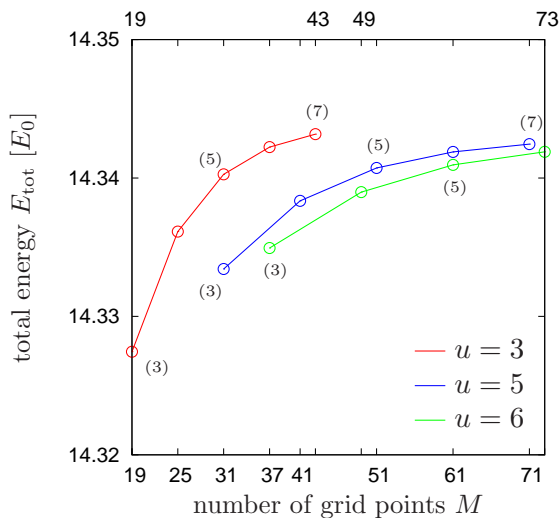


Figure 4.4: Total energy E_{tot} as obtained from solving the correlated Dyson equation for $N = 4$ interacting trapped fermions (all parameters as in Fig. 4.2). Presented is the dependence on the total number of grid points $M(u, p) = 2up + 1$. The differently colored lines show the behavior for ($u = \text{const.}, p$) and numbers in brackets indicate the values of p . The computations have been carried out with $n_b = 15$ Hartree-Fock orbitals.

grid points M the energy is thereby changing due to the representation of $\mathbf{g}^M(\tau)$ on the UPM and due to the additional numerical integration involved in Eq. (4.44). One recognizes that for $M \gtrsim 60$ relatively good convergence ($\Delta E_{\text{tot}} \lesssim \pm 2.0 \times 10^{-3} E_0$) is obtained. This agrees with a number of 40 to 80 grid points stated as being sufficient in the work of N.E. Dahlen *et al.* [48] on the self-consistent solution of the Dyson equation for atoms and molecules. As a comment however, a large enough number M is not the only convergence criterion: Obviously, when the mesh-parameter p is being increased so is the number M , but for a fixed parameter u the time-grid can become (compared with points around $\tau = -\beta/2$) too dense at the end-points of the interval $[-\beta, 0]$ and, thus, will not appropriately represent the Green's function. This refers to the red curve in Fig. 4.4, where for $p \gtrsim 7$ a slightly different total energy is obtained.

4.4. Program structure. Overview

So far, numerical details corresponding to the solution of the Dyson equation have been discussed whereby precedingly it had been necessary to introduce the Hartree-Fock Green's function generated by the solution of the HF (Roothaan-Hall) equations.

In this section—before proceeding with the numerical details for the real-time propagation in nonequilibrium (see Sect. 4.5)—a brief overview of the structure of the code as a whole is given and is illustrated by the flow chart shown in Fig. 4.5. Furthermore, general aspects on the equilibrium computations and the simulation of the N -particle dynamics are addressed.

The general scheme of the program is organized as follows. After all necessary input has been read from file—see Table 4.1 for a summary of the particular quantities and explanation—the program starts to perform the main calculations which are divided into three separate main kernels (A), (B) and (C). The first two parts contain self-consistent iterative procedures and lead to the solution of the mean-field (Hartree-Fock) problem and the computation of the correlated thermal equilibrium state, respectively. The last kernel (which is turned off in an equilibrium calculation) then proceeds with the numerical integration of the real-time Keldysh/Kadanoff-Baym equations and propagates the Green's function matrices $\mathbf{g}^{\lessgtr,1/\Gamma}$ in the two-time plane (t, t') starting from the just obtained correlated initial state. All the details which here are included and consequently appear in the flow chart are elaborately explained in the next section.

Throughout in the course of the different procedures and in particular during time-propagation, several subroutines have auxiliary jobs or compute physical quantities (as e.g. density or relevant

input quantity	referring symbol
particle number, (fermions/bosons)	$N, (f/b)$
inverse temperature	β
coupling parameter	λ
# basis functions, # neglected orbitals, overlap	$n_b, n_b^{\text{cutoff}}, o_{ij}$
UPM parameters	u, p
real-time discretization, # steps	Δ, n_Δ
precomputed matrices; $i, j \in \{0, \dots, n_b - 1\}$	$h_{ij}^0(t) = t_{ij} + v_{ij}(t), w_{ij,kl}$
self-energy approximation	HF, HF+2 nd Born; xc: ON/OFF

Table 4.1: Explanation of input quantities appearing in the flow chart of Fig. 4.5. The abbreviation 'xc' refers to the exchange contributions of Σ which either can be included (ON) or omitted (OFF) within the numerical computations.

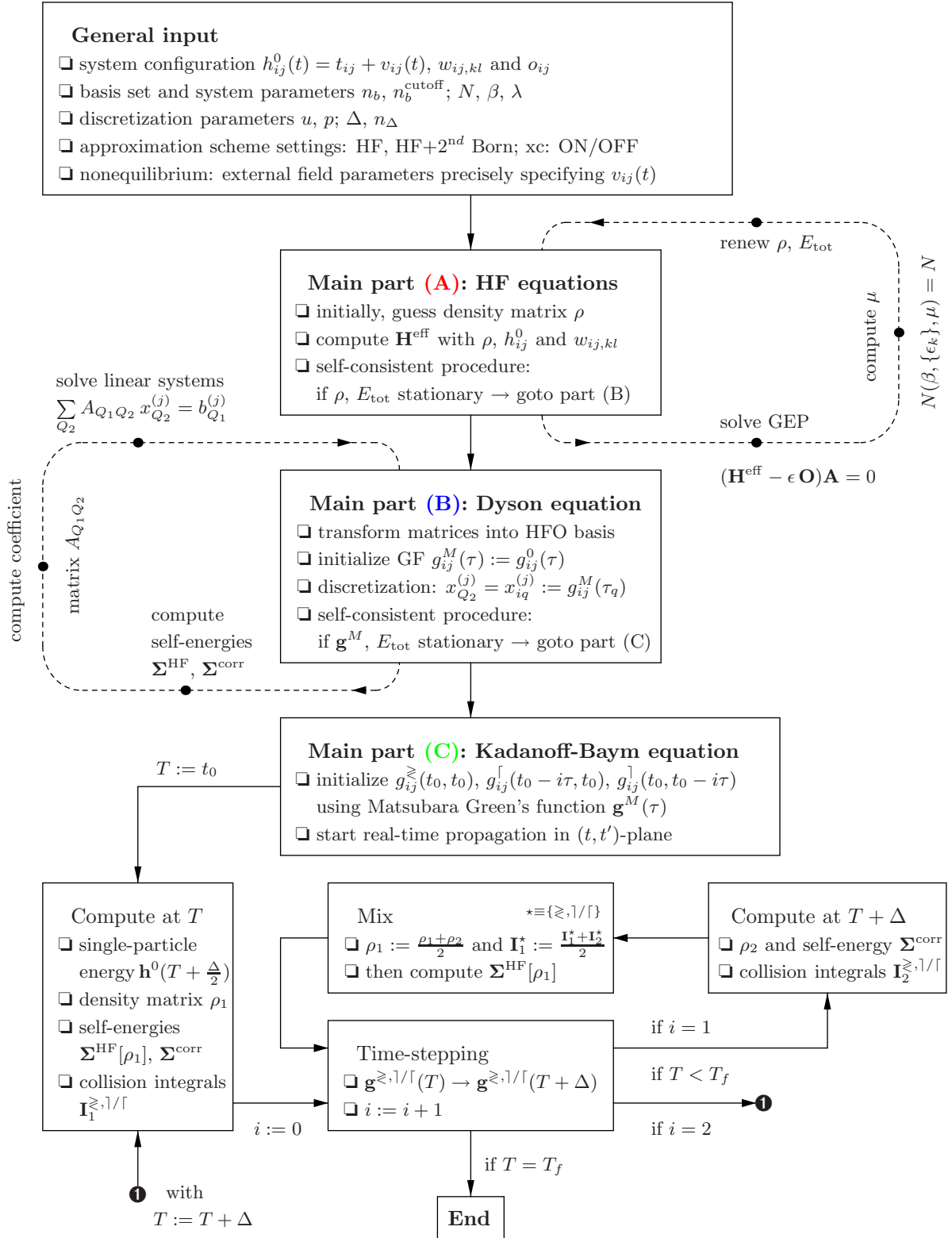


Figure 4.5: Scheme of the numerical solution of the Dyson equation and the Keldysh-/Kadanoff-Baym equations within a basis representation. Solid lines denote the normal program flux while dashed lines indicate the self-consistency loops of main part (A) and (B), respectively. For simplicity, routines concerning any data output and computation of physical quantities are not shown.

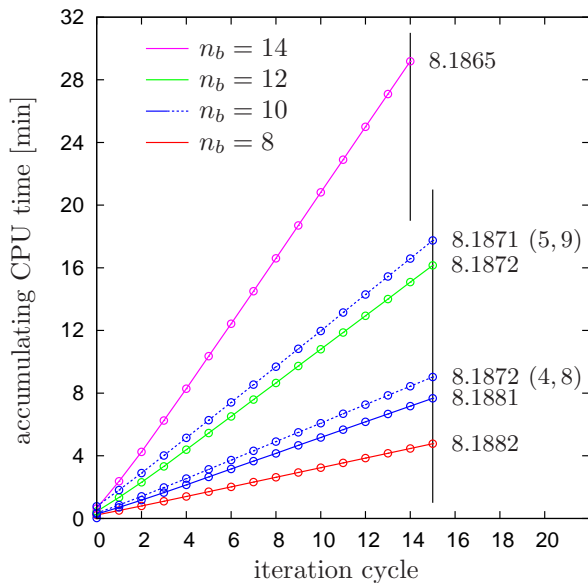


Figure 4.6: CPU time required for the computation of the self-consistent Matsubara Green’s function for $N = 3$ trapped fermions at $\beta = 2$ and $\lambda = 1.6$ (full second Born approximation). Per iteration cycle a constant computing time is necessary leading to the linear increase of the shown curves. Convergence is thereby obtained within 14 or 15 iteration cycles. The different curves correspond to different sizes n_b of the HF basis and the numbers indicate the resulting total energy E_{tot} . Except for the dashed curves all computations have been carried out with uniform power-mesh parameters $(u, p) = (3, 9)$, $M = 55$. Required norm: $\Delta \mathbf{x}^{(j)} \approx 10^{-7}$. Processor: Intel Core 2 CPU, 1.66 GHz.

energy contributions) writing them to data output files. The corresponding graphical details are neglected in Fig. 4.5.

For computation of the Matsubara Green’s function, typical simulation parameters are the following. Usually, a relatively low number of basis states is inserted in the calculations, i.e. typically it is $8 \leq n_b \leq 20$. Consequently, this of course limits the possible number of treated particles ranging from $N = 2$ to about $N \lesssim 10$ for small coupling parameters $\lambda \lesssim 1$ and moderate temperatures of $\beta > 1$, (see the beginning of the next chapter for a more precise classification of the numerical results). In addition, the accurate representation of the Matsubara Green’s function on the uniform power-mesh (UPM) is necessary for the simulation of the equilibrium state, and to this end the parameters (u, p) have to be chosen adequately as discussed in Sects. 4.2 and 4.3, respectively.

Of interest is also the performance of the numerical algorithm (B) which is limited by the set of discretization parameters $\{n_b, (u, p)\}$ and by the applied coupling λ which in practice turns out to solely determine the number of needed iteration cycles. Fig. 4.6 shows the CPU (central processing unit) time typically required by kernel (B) for different situations solving the Dyson equation. Optimum performance is thereby reached when a relatively small HF basis coincides with an appropriate uniform power-mesh resulting in low errors in the observables, as e.g. the system’s total energy. On a single machine—being equipped similarly as stated within the caption of Fig. 4.6—the computing time typically does not exceed one hour leading to acceptable physical results. However, the number of applied HF orbitals has a large effect on the CPU time: The computing time namely scales quadratically with n_b whereas the number of required iteration cycles—that make $\mathbf{g}^M(\tau)$ stationary—only changes slightly. Thus, a large basis set ($n_b \approx 20$) in general leads to a time-consuming calculation which refers to the involved computations of the self-energies and the convolution integrals $F_{ij}(\tau_1, \tau_2)$ as mentioned in the end of Sect. 4.3.

Furthermore, the performance properties of kernel (C) differ from part (B) due the appearing of more sophisticated quantities as there are the two-time correlation functions $\mathbf{g}^{\geq}(t, t')$ and the mixed functions $\mathbf{g}^{|\cdot|}(t, t')$ which both increase in size during time-propagation. Especially, the evaluation of the memory kernels, i.e. the collision integrals over earlier times, then influences the algorithm speed. For a more detailed discussion which explains the behavior in dependence on the HF basis and the time-step Δ see Sect. 6.1.1.

4.5. Solving the Keldysh/Kadanoff-Baym equations

Once the thermodynamic equilibrium state is known from the Matsubara Green's function $\mathbf{g}^M(\tau)$, one can start to propagate it in real-time according to the Keldysh/Kadanoff-Baym equations (KKBE) of Chap. 3, Eqs. (3.59-3.62). This implies that one has to compute all the complex Green's function matrices with one or two time arguments situated on the real axis. These are of course the four propagators $\mathbf{g}^{\gtrless}(t, t')$, $\mathbf{g}^{\lrcorner}(t_0 - i\tau, t')$ and $\mathbf{g}^{\lrcorner/}(t, t_0 - i\tau)$.

The propagation scheme to be explained here is practically identical to the one used by N.E. Dahlen *et al.* [15] and implemented similar to the one described by Köhler *et al.* [61], Semkat *et al.* [51] and Ref. [13]. The differences concerning Refs. [13, 51, 61] thereby lie in the inhomogeneity of the considered quantum system and in the way of treating the initial correlations. Due to the former aspect, the dimensionality of the numerical objects is in the present application increased—to be handled are matrices rather than vectors. Regarding the latter, the initial correlations here follow in a natural way from the correlated initial state characterized by the finite temperature Matsubara Green's function.

Assuming $t_0 = 0$ without loss of generality, the lesser and greater functions, $\mathbf{g}^<(t, t')$ and $\mathbf{g}^>(t, t')$, and the mixed functions, $\mathbf{g}^{\lrcorner}(-i\tau, t)$ and $\mathbf{g}^{\lrcorner/}(t, -i\tau)$, satisfy the initial conditions

$$\mathbf{g}^<(0, 0) = i \mathbf{g}^M(0^-), \quad \mathbf{g}^>(0, 0) = i \mathbf{g}^M(0^+) = -i \mathbf{g}^M(-\beta), \quad (4.45)$$

$$\mathbf{g}^{\lrcorner/}(0, -i\tau) = i \mathbf{g}^M(-\tau), \quad \mathbf{g}^{\lrcorner}(-i\tau, 0) = i \mathbf{g}^M(\tau) = -i \mathbf{g}^M(\tau - \beta). \quad (4.46)$$

With the general symmetry properties discussed in Chap 2—one has $[\mathbf{g}^{\gtrless}(t, t')]^\dagger = -\mathbf{g}^{\gtrless}(t', t)$, and on the time-diagonal applies $\mathbf{g}^>(t, t) = -i + \mathbf{g}^<(t, t)$ as boundary condition—one can restrict oneself to solve $\mathbf{g}^>(t, t')$ for $t > t'$ and $\mathbf{g}^<(t, t')$ for $t' \leq t$. This is illustrated in Fig. 4.7, where the lesser correlation function is represented on the red triangle and the greater one on the adjacent blue triangle which both expand during time-propagation.

The equations of motion (KKBE, Eqs. (3.59-3.62)) can then be rewritten in the form

$$i \partial_t \mathbf{g}^>(t, t') = \mathbf{h}(t) \mathbf{g}^>(t, t') + \mathbf{I}_1^>(t, t'), \quad (4.47)$$

$$-i \partial_t \mathbf{g}^<(t', t) = \mathbf{g}^<(t', t) \mathbf{h}(t) + \mathbf{I}_2^<(t', t), \quad (4.48)$$

$$i \partial_t \mathbf{g}^{\lrcorner/}(t, -i\tau) = \mathbf{h}(t) \mathbf{g}^{\lrcorner/}(t, -i\tau) + \mathbf{I}^{\lrcorner/}(t, -i\tau), \quad (4.49)$$

$$-i \partial_t \mathbf{g}^{\lrcorner}(-i\tau, t) = \mathbf{g}^{\lrcorner}(-i\tau, t) \mathbf{h}(t) + \mathbf{I}^{\lrcorner}(-i\tau, t), \quad (4.50)$$

where in $\mathbf{h}(t) = \mathbf{h}^0(t) + \mathbf{\Sigma}^{\text{HF}}(t)$ the Hartree-Fock self-energy and the time-dependent contribution from the single-particle Hamiltonian are collected. Furthermore, the collision terms in Eqs. (4.47-4.50) are given by

$$\begin{aligned} \mathbf{I}_1^>(t, t') &= \int_0^t d\bar{t} [\mathbf{\Sigma}^>(t, \bar{t}) - \mathbf{\Sigma}^<(t, \bar{t})] \mathbf{g}^>(\bar{t}, t') + \int_0^{t'} d\bar{t} \mathbf{\Sigma}^>(t, \bar{t}) [\mathbf{g}^<(\bar{t}, t') - \mathbf{g}^>(\bar{t}, t')] \\ &\quad - i \int_0^\beta d\bar{\tau} \mathbf{\Sigma}^{\lrcorner/}(t, -i\bar{\tau}) \mathbf{g}^{\lrcorner/}(-i\bar{\tau}, t'), \end{aligned} \quad (4.51)$$

$$\begin{aligned} \mathbf{I}_2^<(t', t) &= \int_0^{t'} d\bar{t} [\mathbf{g}^>(t', \bar{t}) - \mathbf{g}^<(t', \bar{t})] \mathbf{\Sigma}^<(\bar{t}, t) + \int_0^t d\bar{t} \mathbf{g}^<(t', \bar{t}) [\mathbf{\Sigma}^<(\bar{t}, t) - \mathbf{\Sigma}^>(\bar{t}, t)] \\ &\quad - i \int_0^\beta d\bar{\tau} \mathbf{g}^{\lrcorner/}(t', -i\bar{\tau}) \mathbf{\Sigma}^{\lrcorner/}(-i\bar{\tau}, t), \end{aligned} \quad (4.52)$$

$$\mathbf{I}^{\lrcorner/}(t, -i\tau) = \int_0^t d\bar{t} [\mathbf{\Sigma}^>(t, \bar{t}) - \mathbf{\Sigma}^<(t, \bar{t})] \mathbf{g}^{\lrcorner/}(\bar{t}, -i\tau) + \int_0^\beta d\bar{\tau} \mathbf{\Sigma}^{\lrcorner/}(t, -i\bar{\tau}) \mathbf{g}^M(\bar{\tau} - \tau), \quad (4.53)$$

$$\mathbf{I}^{\lrcorner}(-i\tau, t) = \int_0^t d\bar{t} \mathbf{g}^{\lrcorner/}(-i\tau, \bar{t}) [\mathbf{\Sigma}^<(\bar{t}, t) - \mathbf{\Sigma}^>(\bar{t}, t)] + \int_0^\beta d\bar{\tau} \mathbf{g}^M(\tau - \bar{\tau}) \mathbf{\Sigma}^{\lrcorner/}(-i\bar{\tau}, t), \quad (4.54)$$

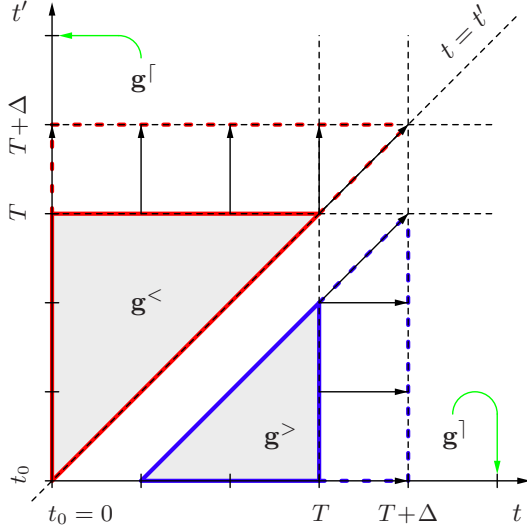


Figure 4.7: Two-time plane in which the correlation functions $\mathbf{g}^{\gtrless}(t, t')$ are defined. Due to symmetry properties it is sufficient to propagate $\mathbf{g}^<$ on the upper (red) triangle plus time-diagonal and to integrate the equation of motion for $\mathbf{g}^>$ on the lower (blue) triangle. The mixed functions $\mathbf{g}^|$ and \mathbf{g}^{\lrcorner} have a single real-time argument and are defined on the corresponding time-axis only—their second time argument is situated on the imaginary branch of the contour. Also illustrated is the time-stepping $T \rightarrow T + \Delta$ with an expanding square for $t, t' \leq T$.

and in particular obey the following symmetry relations:

$$\mathbf{I}^{\gtrless}(t, t') = - \left[\mathbf{I}^{\gtrless}(t', t) \right]^{\dagger}, \quad \mathbf{I}^{\lrcorner}(-i\tau, t) = \left[\mathbf{I}^{\lrcorner}(t, -i(\beta - \tau)) \right]^{\dagger}. \quad (4.55)$$

In order to numerically integrate this set of integro-differential equations one starts with expressions (4.45) and (4.46) at $t = t' = 0$ and extends the Green's function matrices into the two-time plane (t, t') as illustrated in Fig. 4.7. Thereby, the correlation functions become discretized on a 2D even-spaced grid with temporal width Δ , and the mixed functions consequently get associated with a single real-time argument (discretized by Δ) and their respective imaginary time which lies—due to the representation of $\mathbf{g}^M(\tau)$ —on the uniform-power mesh, see Sect. 4.4.

Assume now that the Green's functions are fully known for $t, t' \leq T$. As derived in-depth in Appendix B.1 for a *small* time-step of length Δ , the pure real-time Green's functions in $T + \Delta$ are then given by¹

$$\mathbf{g}^>(T + \Delta, t') = U(\Delta) \mathbf{g}^>(T, t') - V(\Delta) \mathbf{I}_1^>(t'), \quad (4.56)$$

$$\mathbf{g}^<(t', T + \Delta) = \mathbf{g}^<(t', T) U^{\dagger}(\Delta) - \mathbf{I}_2^<(t') V^{\dagger}(\Delta), \quad (4.57)$$

$$\mathbf{g}^<(T + \Delta, T + \Delta) = U(\Delta) \left[\mathbf{g}^<(T, T) + \sum_{n=0}^{\infty} C^{(n)} \right] U^{\dagger}(\Delta), \quad (4.58)$$

while for the mixed Green's functions one obtains

$$\mathbf{g}^{\lrcorner}(t + \Delta, -i\tau') = U(\Delta) \mathbf{g}^{\lrcorner}(t, -i\tau') - V(\Delta) \mathbf{I}^{\lrcorner}(-i\tau'), \quad (4.59)$$

$$\mathbf{g}^{\lrcorner}(-i\tau, t' + \Delta) = \mathbf{g}^{\lrcorner}(-i\tau, t') U^{\dagger}(\Delta) - \mathbf{I}^{\lrcorner}(-i\tau) V^{\dagger}(\Delta). \quad (4.60)$$

The introduced matrices $U(\Delta)$ and $V(\Delta)$, see also Appendix B.2 for practical implementation, are thereby defined in terms of the effective energy $\bar{\mathbf{h}} = \mathbf{h}(T + \frac{\Delta}{2})$ through

$$U(\Delta) = \exp(-i \bar{\mathbf{h}} \Delta), \quad V(\Delta) = \frac{1}{\bar{\mathbf{h}}} (1 - e^{-i \bar{\mathbf{h}} \Delta}), \quad (4.61)$$

and recursively the coefficient matrices $C^{(n)}$ are given by the commutator

$$C^{(n)} = \frac{i \Delta}{n + 1} \left[\bar{\mathbf{h}}, C^{(n-1)} \right], \quad C^{(0)} = -i \mathbf{I}_{12}^< \Delta, \quad (4.62)$$

¹This is due to N.E. Dahlen and the related work [15].

with $\mathbf{I}_{12}^<$ being constant in the interval $T \leq t, t' \leq T + \Delta$. As discussed in Appendix B.1, for a small time-step

$$\mathbf{I}_{12}^< \approx - [\mathbf{I}_1^>(t', t)]^\dagger - \mathbf{I}_2^<(t, t'), \quad (4.63)$$

and since $\mathbf{I}_{12}^<$ is directly connected with the time-derivative of the Green's function $\mathbf{g}^<$ on the time-diagonal, it has the property $\text{Tr}\{\mathbf{I}_{12}^<\} = 0$, corresponding to conservation of the particle number. In the numerical treatment, the computation of this trace serves as a sensitive test for the self-energies—if obtained from a conserving theory—being accurate.

Furthermore, the notation of the collision integrals appearing in Eqs. (4.56-4.60) has to be explained: For $T \leq t \leq T + \Delta$ one has approximated

$$\mathbf{I}_1^>(t, t') \approx \mathbf{I}_1^>(t'), \quad \mathbf{I}_2^<(t', t) \approx \mathbf{I}_2^<(t'), \quad (4.64)$$

$$\mathbf{I}^\uparrow(t, -i\tau) \approx \mathbf{I}^\uparrow(-i\tau), \quad \mathbf{I}^\uparrow(-i\tau, t) \approx \mathbf{I}^\uparrow(-i\tau), \quad (4.65)$$

which in addition has the numerical advantage, that the matrices $\mathbf{I}_{1,2}^{\gtrless}$ and $\mathbf{I}^{\uparrow/\downarrow}$ can be simply implemented as one-dimensional arrays in time.

For practical use, the series expansion entering Eq. (4.58) must be truncated at a finite $n = n_{\max}$. In addition, the nested commutators of definition (4.62) make the evaluation of the coefficient matrices $C^{(n)}$ numerically expensive, so that one has to restrict oneself to a relatively low $n_{\max} = 3(\pm 1)$ in the actual calculations. However, the resulting error is of the order $\mathcal{O}(\Delta^{n_{\max}+1})$ and is thus negligible for a small time-step Δ . To clarify the origin of the series expansion see also Appendix B.1.

4.5.1. Scheme of the numerical solution of the KKBE

As it has been implemented, the time-stepping algorithm is in detail more advanced than Eqs. (4.56-4.60). For a proper description of the dynamics, the sensitivity of physical quantities to the finite length Δ of the time-step should be reduced as much as possible. In particular, it is essential to ensure low errors in density, energy and energy conservation which govern the upper limit for Δ , see Sect. 6.1 for discussion. To this end, it has been found consistent with the numerically available resources to propagate all Green's function matrices twice in each time-step. Similar to the method used by standard Euler-type integrators, the density matrix and the set of collision integrals $\{\mathbf{I}\} \equiv \{\mathbf{I}_1^>, \mathbf{I}_2^<, \mathbf{I}^\uparrow, \mathbf{I}^\downarrow\}$ —being practically the time-derivatives of the Green's functions in Eqs. (B.9-B.12)—are thereby renewed once during the time-stepping $T \rightarrow T + \Delta$. This procedure facilitates the completion of the present time-step with an effectively more precise second evaluation of the Green's function matrices in $T + \Delta$.

As is also illustrated in the flow chart of Fig. 4.5, the implemented algorithm can then be summarized as follows:

- i. Initialize \mathbf{g}^{\gtrless} and $\mathbf{g}^{\uparrow/\downarrow}$ at $t_0 = 0$ according to Eqs. (4.45-4.46) using the Matsubara Green's function $\mathbf{g}^M(\tau)$. Since it is sufficient to solve $\mathbf{g}^>(t, t')$ for $t > t'$ and $\mathbf{g}^<(t, t')$ for $t' \leq t$, propagate $\mathbf{g}^<$ on the upper triangular time-array plus diagonal, and $\mathbf{g}^>$ on the lower triangular time-array, see Fig. 4.7.
- ii. Start of the loop: Determine the single-particle energy at half of the time-step of length Δ , i.e. $\mathbf{h}^0(T + \Delta/2)$.
- iii. Calculate the density matrix ρ_1 at time T from $\mathbf{g}^<(T)$.
- iv. Compute all necessary self-energies:
 - a) Calculate static Hartree-Fock self-energy $\Sigma^{\text{HF}}[\rho_1]$ using Eq. (4.38) of Sect. 4.3.

- b) Calculate explicitly time-dependent second-order self-energy $\Sigma^{\text{corr}}(t_0 \dots T)$, i.e. all $\Sigma^\star[\mathbf{g}^\star](t_0 \dots T)$ with $\star \equiv \{\gtrless, \lceil/\rceil\}$. These follow from definition (3.58) by replacing the general Green's function by the particular subordinated Green's function.
- v. At time T , calculate all collision integrals for $t, t' \leq T$ from $\mathbf{g}^\star(t_0 \dots T)$ and $\Sigma^{\text{corr}}(t_0 \dots T)$ and obtain the set $\{\mathbf{I}_1\}$.
- vi. Propagate all the Green's functions, $\mathbf{g}^\star(T) \rightarrow \mathbf{g}^\star(T + \Delta)$, using Eqs. (4.56-4.60), $\{\mathbf{I}_1\}$ and $\mathbf{h} = \mathbf{h}^0 + \Sigma^{\text{HF}}$.
- vii. Calculate the density matrix ρ_2 at time $T + \Delta$ with the just obtained $\mathbf{g}^\star(T + \Delta)$, and extend the second-order self-energy to $\Sigma^{\text{corr}}(t_0 \dots T + \Delta)$.
- viii. Again, calculate the collision integrals with extended $\mathbf{g}^\star(t_0 \dots T + \Delta)$ and $\Sigma^{\text{corr}}(t_0 \dots T + \Delta)$. Obtain set $\{\mathbf{I}_2\}$.
- ix. Approximate density matrix ρ and collision integrals $\{\mathbf{I}\}$ by the mean values of the quantities at times T and $T + \Delta$.
- x. Calculate the new Hartree-Fock self-energy $\Sigma^{\text{HF}}[\rho]$.
- xi. Repropagate all Green's functions, $\mathbf{g}^\star(T) \rightarrow \mathbf{g}^\star(T + \Delta)$, using $\{\mathbf{I}\}$ and \mathbf{h} .
- xii. Finally, return to (ii) with T increased by Δ .

For the numerical integrations being involved in the collision terms $\{\mathbf{I}\}$, Eqs. (4.51-4.54), standard formulas similar to Eq. (4.29) in Sect. 4.3 are implemented so far. However, some improved integrators could be used here if they do not essentially slow down the numerics.

4.5.2. Memory allocation for the Green's functions

Due to discretization in time, all the nonequilibrium Green's functions are four-dimensional objects $a[i][j][p_1][p_2]$, where $\{i, j\}$ indicate the matrix and $\{p_1, p_2\}$ represent the time-arguments t_{p_1} and t_{p_2} on the contour. Within numerical representation it is however useful to summarize both matrix indices as well as both time indices into single arrays. This not only leads to notational clarity, but also is advantageous in handing the quantities over to subroutines within the code, e.g. at fixed time-arguments $\{p_1, p_2\}$. While the correlation functions are thus allocated as a single two-dimensional array with

$$g_{ij}^{\gtrless}(t_{p_1}, t_{p_2}) \rightarrow \text{Gt}[i + n_b \cdot j][p_1 + n_\Delta \cdot p_2], \quad (4.66)$$

where for $p_1 \leq p_2$ it contains the lesser and otherwise the greater function, the mixed functions are generated as

$$g_{ij}^{\lceil}(-i\tau_{q_1}, t_{p_2}) \rightarrow \text{Gl}[i + n_b \cdot j][q_1 + M \cdot p_2], \quad (4.67)$$

$$g_{ij}^{\rceil}(t_{p_1}, -i\tau_{q_2}) \rightarrow \text{Gr}[i + n_b \cdot j][p_1 + n_\Delta \cdot q_2]. \quad (4.68)$$

Thereby, it is $i, j \in \{0, \dots, n_b - 1\}$, the real-time indices run from $p_k = 0$ to $p_k = n_\Delta - 1$, and correspondingly the imaginary-time indices start with $q_k = 0$ and end at $q_k = M - 1$. The length of the time-step is then determined to be $\Delta = \frac{1}{n_\Delta - 1} T_f$, where T_f sets the final time for the integration of the Keldysh/Kadanoff-Baym equations. As introduced in Sect. 4.4, n_Δ denotes the total number of time-steps to be propagated. Practically, also the time-dependent self-energies and the collision integrals are implemented similar to the Green's functions.

Moreover—due to the high dimensionality of the objects (4.66-4.68)—it is a good idea to look at the general memory requirements. For a set consisting of $n_b = 15$ basis functions (Hartree-Fock orbitals), a number of $n_\Delta = 200$ time-steps and typical uniform power-mesh parameters $(u, p) = (5, 7)$ so that $M = 2up + 1 = 71$, the matrices require memory of the size

$$\begin{aligned} \mathbf{g}^{\lessgtr}(t, t') : & \quad (n_b^2 n_\Delta^2) \cdot 16 \text{ Bytes} = 144 \text{ MB} , \\ \mathbf{g}^{|\rceil}(t, t') : & \quad (n_b^2 M n_\Delta) \cdot 16 \text{ Bytes} = 51.12 \text{ MB} . \end{aligned}$$

Each matrix element of the Green's functions is thereby represented by an imaginary double-precision number of 2×8 Bytes. Compared with the corresponding real Matsubara Green's function $\mathbf{g}^M(\tau)$ which is a three-dimensional object and occupies $(n_b^2 M) \cdot 8$ Bytes = 127.8 KB only, the size of the quantities in nonequilibrium is therefore much larger—typically about two to three orders of magnitude whereby n_Δ has the main influence. Nevertheless, in the one-dimensional case, this size domain does not cause any problems with the available storage capacities.

4.5.3. Time-dependent energies and energy conservation

The different energies already collected in Sect. 4.3.2 for the thermal equilibrium state, in nonequilibrium take an explicit time-dependence. Thereby, all single-particle energies (potential and kinetic energy) and the Hartree-Fock energy follow from the time-dependent complex density matrix $\rho(t)$ given by the lesser correlation function $\mathbf{g}^<(t, t')$ at equal time-arguments, i.e. more precisely

$$\rho_{ij}(t) = \pm i g_{ij}^<(t, t) . \quad (4.69)$$

As discussed below, the computation of the correlation energy is somewhat more difficult. If the system is not disturbed by some additional time-dependent potential, the total energy and all contributing energies are conserved, the verification of which is an essential test for the numerics and furthermore controls the time-step length Δ . In summary:

- i. **Single-particle energy** with time-dependent matrix $\mathbf{h}^0(t) = \mathbf{t}(t) + \mathbf{v}(t)$:

$$E_{\text{single}}(t) = \Re \text{Tr}\{\mathbf{h}^0(t) \rho(t)\} + \mu N . \quad (4.70)$$

Thereby, $\mathbf{v}(t) = \mathbf{v}^0 + \mathbf{v}_{\text{ext}}(t)$ allows to include an additional time-dependent potential $\mathbf{v}_{\text{ext}}(t)$ besides the static (confinement) part \mathbf{v}^0 .

- ii. **Hartree-Fock energy**, whereby the time-dependence of the density $\rho(t)$ leads to a time-dependent HF self-energy $\Sigma^{\text{HF}}(t)$:

$$E_{\text{HF}}(t) = \Re \frac{1}{2} \text{Tr}\{\Sigma^{\text{HF}}(t) \rho(t)\} . \quad (4.71)$$

- iii. **Correlation energy**: With Ref. [54] one obtains similar to the respective definition in thermodynamic equilibrium (4.44)

$$E_{\text{corr}}(t) = \Im \frac{1}{2} \int_{\mathcal{C}} d\bar{t} \text{Tr}\{\Sigma^{\text{corr}}(t, \bar{t}) \mathbf{g}(\bar{t}, t^+)\} = \Im \frac{1}{2} \text{Tr}\{\mathbf{I}_1^>(t, t)\} , \quad (4.72)$$

where the integral is performed over the full contour and further $\mathbf{g}(t, t') = \theta(t, t') \mathbf{g}^>(t, t') + \theta(t', t) \mathbf{g}^<(t, t')$ denotes the full nonequilibrium Green's function matrix. If one explicitly

writes out the collision term $\mathbf{I}_1^>(t)$ and evaluates Eq. (4.72) for $t = t_0 = 0$, one arrives with the initial conditions $\mathbf{g}^\lceil(-i\tau, 0) = -i\mathbf{g}^M(\tau - \beta)$ and $\Sigma^\lceil(0, -i\tau) = i\Sigma^M(-\tau)$ at

$$\begin{aligned} E_{\text{corr}}(t_0) &= \Im \frac{1}{2} \text{Tr} \{ \mathbf{I}_1^>(0) \} \\ &= \Im \frac{1}{2} \text{Tr} \left\{ \int_0^{t=0} d\bar{t} \dots + \int_0^{t'=0} d\bar{t} \dots - i \int_0^\beta d\bar{\tau} \Sigma^\lceil(t=0, -i\bar{\tau}) \mathbf{g}^\lceil(-i\bar{\tau}, t'=0) \right\} \\ &= \Im \frac{-i}{2} \int_0^\beta d\tau \text{Tr} \{ \Sigma^M(-\tau) \mathbf{g}^M(-\tau - \beta) \}, \end{aligned} \quad (4.73)$$

which is just the known expression (4.44) for the equilibrium state.

- iv. **Field energy:** If $\mathbf{v}_{\text{ext}}(t) \neq 0$ then the total energy $E_{\text{tot}}(t)$ as the sum of (4.70-4.72) in general will change in time and the correctness of the time-propagation can no longer be proven by its conservation. Nevertheless, if the system evolves e.g. under a time-dependent dipole field—this will be subject of investigation in Chap. 6—then one easily can compare the energy change with the work done by the external field. An arbitrary dipole field enters the single-particle Hamiltonian $\mathbf{h}^0(t)$ as

$$\mathbf{v}_{\text{ext}}(t) = \mathcal{E}(t) \mathbf{d}, \quad (4.74)$$

where $\mathcal{E}(t)$ determines the time-dependence of the electric field and \mathbf{d} denotes the dipole matrix $d_{ij} = q_0 \int dx \Phi_i^*(x) x \Phi_j(x)$ with q_0 indicating the particle charge and $\Phi_k(x)$ being the Hartree-Fock orbitals. The work done by this field is then accessible through

$$E_{\text{field}}(t) = -q_0 \int_{t_0}^t d\bar{t} \langle x(\bar{t}) \rangle \partial_{\bar{t}} \mathcal{E}(\bar{t}), \quad (4.75)$$

with constraint $\mathcal{E}(t_0) \equiv 0$ and position expectation value $\langle x(t) \rangle = \frac{1}{q_0} \text{Tr} \{ \mathbf{d} \rho(t) \}$. Of course, expression (4.75) does not contribute to the total energy, but the sum $E_{\text{tot}}(t) + E_{\text{field}}(t)$ will be a constant in time and is therefore a good reference quantity for numerical investigation.

Besides verifying the energy conservation—if any time-dependent potential is absent—it is in particular interesting to separately analyze how the three different terms or integrals entering the collision terms $\mathbf{I}_{1,2}^>$ in Eqs. (4.51,4.52) are contributing to the correlation energy $E_{\text{corr}}(t)$ via Eq. (4.72). Initially, at time t_0 , the first two integrals are zero and, thus, do not contribute, i.e. the correlation energy is determined by $\mathbf{g}^M(\tau)$ only which is consistent with Eq. (4.73). But as t increases both former integrals become non-zero leading to the latter integral contributing less if the total energy is conserved.

As Fig. 4.8 and Fig. 4.9 show for the example of two harmonically confined fermions, the interplay of the three different integrals (red, blue and green lines) is in general not trivial and the contribution of each strongly varies in time although their sum is almost constant (violet curves). Furthermore, as extremely sensitive to the conservation of the correlation energy—clearly more than the length of the time-step—proves the uniform power-mesh on which the quantities \mathbf{g}^M and Σ^M are defined, see especially Fig 4.8. If the grid-parameters (u, p) are chosen inadequately (see curves with $(u, p) = (3, 4)$ and $(3, 5)$, respectively), the total correlation energy itself starts to oscillate with varying period instead of being preserved. In addition, the gray curves of Fig. 4.8 point out that this oscillation is not damped out in time as one could guess from the upper figure. However, for intermediate time-points, around $t = 1.5$ in the lower figure, the gray curve comes quite close to the constant (correct) energy.

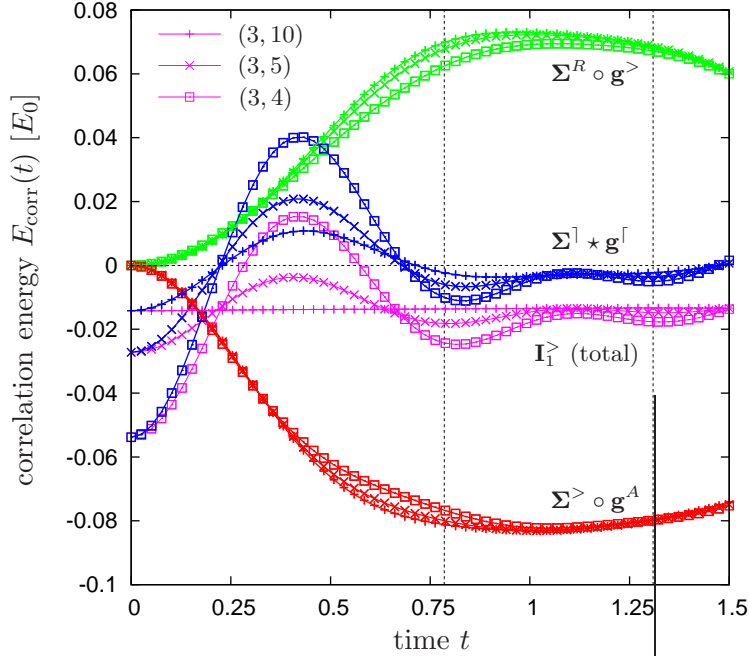


Figure 4.8: Time-evolution of the correlation energy (violet curves) for $N = 2$ trapped fermions with coupling parameter $\lambda = 1$ at quasi zero temperature, $\beta = 50$. The differently colored curves show the contributions from the three individual terms in $\mathbf{I}_1^>(t, t)$. As indicated, different uniform power-mesh (UPM) parameters (u, p) have been used in the computation which has large effects on the preservation of $E_{\text{corr}}(t)$. For $(u, p) = (3, 10)$ the correlation energy is well conserved while for lower p -values the energy is oscillatory. The time is measured in units of the reciprocal confinement frequency Ω^{-1} . Discretization: $n_b = 8$ HFO, $n_\Delta = 60$, $\Delta = 0.025$.

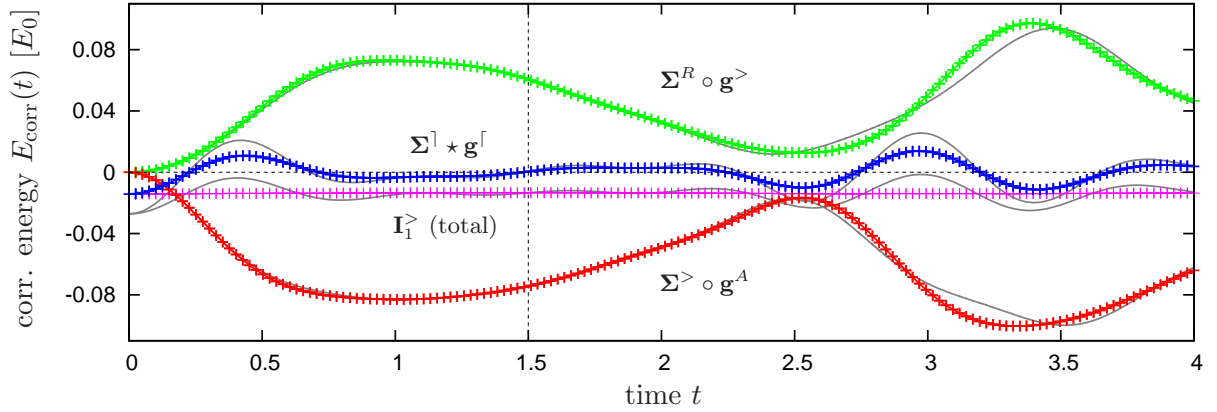


Figure 4.9: Preservation of the correlation energy $E_{\text{corr}}(t)$ (violet curve) with the same UPM parameters $(3, 10)$ as in the upper Fig. 4.8 but for a longer time-propagation. The individual contributions (red, blue and green line) oscillate nontrivially in time. The gray curves in the background indicate the time-dependence for the grid-parameters $(3, 5)$. Discretization: $n_b = 8$ HFO, $n_\Delta = 160$, $\Delta = 0.025$.

As an overall result, one thus can call on the time-dependence of the correlation energy to estimate the numerical quality of the obtained Matsubara Green's function and the corresponding equilibrium state. If $E_{\text{corr}}(t) \neq \text{const.}$ within acceptable bounds, the Matsubara Green's function $\mathbf{g}^M(\tau)$ is certainly not well represented on the uniform power-mesh and will yield physical observables with relatively large errors.

4.5.4. Calculation of retarded and advanced quantities during propagation

In the collision terms given by Eqs. (4.51-4.54), there occur differences of the correlation functions \mathbf{g}^{\gtrless} and the self-energies Σ^{\gtrless} , respectively. As introduced in Sect. 3.1, these quantities shall here again be referred to as the retarded and advanced functions

$$\mathbf{g}^{R/A}(t, t') = \left(\mathbf{g}^{\gtrless}(t, t') - \mathbf{g}^{\lessgtr}(t, t') \right), \quad (4.76)$$

$$\Sigma^{R/A}(t, t') = \left(\Sigma^{\gtrless}(t, t') - \Sigma^{\lessgtr}(t, t') \right), \quad (4.77)$$

although this differs from the conventional definition—compare with Eq. (2.24).

Within the numerics, one has to compute $\mathbf{g}^{R/A}(t, t')$ for different time-arguments t and t' . To simplify this evaluation, it is thereby useful to apply the relation $[\mathbf{g}^{\lessgtr}(t, t')]^\dagger = -\mathbf{g}^{\lessgtr}(t', t)$ (see Sect. 2.2.1) in order to rewrite for $t \neq t'$:

$$\begin{aligned}\mathbf{g}^{R/A}(t, t') &= \mathbf{g}^{\lessgtr}(t, t') - \mathbf{g}^{\lessgtr}(t, t') , \\ &= \mathbf{g}^{\lessgtr}(t, t') + [\mathbf{g}^{\lessgtr}(t', t)]^\dagger .\end{aligned}\tag{4.78}$$

Since the same relation holds for the self-energies, one has in addition

$$\Sigma^{R/A}(t, t') = \Sigma^{\lessgtr}(t, t') + [\Sigma^{\lessgtr}(t', t)]^\dagger .\tag{4.79}$$

At equal times $t = t'$, the situation is even simpler. From the relation between both correlation functions, i.e. $\mathbf{g}^>(t, t) = -i + \mathbf{g}^<(t, t)$, it directly follows that

$$\mathbf{g}^R(t, t) = \mathbf{g}^>(t, t) - \mathbf{g}^<(t, t) = -i ,\tag{4.80}$$

$$\mathbf{g}^A(t, t) = \mathbf{g}^<(t, t) - \mathbf{g}^>(t, t) = i .\tag{4.81}$$

4.5.5. Spectral function and other time-dependent observables

Before proceeding with the next chapter and examining the equilibrium properties of harmonically confined fermions, it is worth summarizing the expressions for other important observables in nonequilibrium besides the energies which have been given in Sect. 4.5.3 of this chapter. With the basis representation of the two-time Green's functions there are accessible (also compare with Sect. 2.3):

- **Spectral function.** The matrix of the spectral function in the (T, ω) -space, where $T = (t_1 + t_2)/2$ is the center of mass time and the frequency ω corresponds to the relative time $t = t_1 - t_2$, is defined by [15]

$$\mathbf{A}(T, \omega) = i \int dt e^{i\omega t} [\mathbf{g}^>(T + t/2, T - t/2) - \mathbf{g}^<(T + t/2, T - t/2)] .\tag{4.82}$$

If any time-dependent potential is absent, the Green's function will only depend on the relative time t , and the spectral function thus will be independent of T . In particular, for a Hartree-Fock Green's function which is characterized by the set of energy eigenvalues $\{\epsilon_k\}$, the spectral information reads

$$\Re A_{kk}(\omega) \propto -\frac{i}{\pi} \int dt e^{i\omega t} \sin(\epsilon_k t) = -i^2 \delta(\omega - \epsilon_k) ,\tag{4.83}$$

i.e. there exist sharp peaks that coincide with the Hartree-Fock energies. If one includes correlation effects in the Keldysh/Kadanoff-Baym equations, typical oscillations in $\mathbf{A}(t_1, t_2)$ with respect to the relative time-scale will be damped corresponding to a broadened one-particle spectrum—this is investigated in Chap. 6.

- **Density.** The density matrix has already been introduced in the preceding section by definition (4.69). Evoking Sect. 2.3, the spatially resolved density follows further from the time-ordered Green's function as ($1 \equiv x, t$)

$$\langle n(1) \rangle = \pm i G(1, 1^+) ,\tag{4.84}$$

and, thus, reads in the HF orbital representation

$$\begin{aligned}\langle n(x, t) \rangle &= \pm i \sum_{kl} \Phi_k^*(x) \Phi_l(x) g_{kl}^<(t, t) \\ &= \pm i \sum_{ijkl} A_{ik}^* A_{jl} \phi_i^*(x) \phi_j(x) g_{kl}^<(t, t),\end{aligned}\quad (4.85)$$

where A_{kl} denote the HF eigenvectors and the wave functions $\phi_i(x)$ are the natural orbitals of the ideal system. Notice that one here sums up both the diagonal and off-diagonal elements of the density matrix $\rho_{kl}(t) = \pm i g_{kl}^<(t, t)$. The time-evolution of the mean particle number can then be calculated according to

$$\begin{aligned}\langle N(t) \rangle &= \pm i \int dx G(xt, xt^+) \\ &= \pm i \sum_{kl} \left(\int dx \Phi_k^*(x) \Phi_l(x) \right) g_{kl}^<(t, t) = \pm i \sum_k g_{kk}^<(t, t),\end{aligned}\quad (4.86)$$

and only depends on the diagonal elements of the lesser correlation function $\mathbf{g}^<(t, t)$.

- **Polarizability.** In linear response, the polarizability $\alpha(\omega)$ is given by the ratio of the induced dipole moment of the *artificial atom* to the electric field that produces this dipole moment,

$$\alpha(\omega) = -\frac{1}{\bar{\mathcal{E}}_0} \int dt e^{i\omega t} \langle d(t) \rangle, \quad (4.87)$$

where $\bar{\mathcal{E}}_0$ gives the mean amplitude of the applied electric field and the time-dependent dipole moment $\langle d(t) \rangle = \pm i \sum_{kl} d_{kl} g_{kl}^<(t, t)$ is computed with the dipole matrix \mathbf{d} as defined in Eq. (4.74). Compare also with Ref. [15].

All other macroscopic expectation values that have been introduced at the end of Chap. 2 (current, Wigner distribution function, etc.) follow in the same manner by inserting the basis representation of the Green's function.

5. Equilibrium properties of artificial atoms

In the preceding chapter, the numerical procedures for studying equilibrium and nonequilibrium have been described in detail and a few examples with respect to the special case of 1D harmonically confined fermions have been quoted. In this chapter, explicit results for the correlated equilibrium state of such trapped fermions are systematically arranged and interpreted on physical grounds. Referring to the Hamiltonian already introduced in Chap. 1 (Sect. 1.2),

$$H = H_1 + \lambda H_{12} = \sum_{i=1}^N \left(-\frac{1}{2} \partial_{x_i}^2 + \frac{1}{2} x_i^2 \right) + \sum_{i < j} \frac{\lambda}{\sqrt{(x_i - x_j)^2 + a^2}}, \quad (5.1)$$

with $V_{\text{ext}}(x_i, t) \equiv 0$ and a pair-interaction potential of Coulomb type, the corresponding equilibrium properties are investigated by the Matsubara Green's function $\mathbf{g}^M(\tau)$ in dependence on particle number, inverse temperature and coupling parameter, i.e. in dependence on the set of parameters $\{N, \beta, \lambda\}$. Fig. 5.1 gives an overview and a classification of the results. In the limit $\lambda \rightarrow 0$ the exact properties of the ideal (noninteracting) system are recovered. Due to the availability of the Hartree-Fock Green's function $\mathbf{g}^0(\tau)$, it is further possible to compare the mean-field result with the correlated computations and, thus, directly extract the influence of the particle collisions on the static properties.

The overall analysis is thereby based on the oscillator wave functions $\phi_n(x) = N_n e^{-x^2/2} H_n(x)$ (N_n accounts for normalization, $H_n(x)$ denotes the Hermite polynomials and $n = 0, 1, 2, \dots$; see also Appendix A) which yield a complete orthonormal basis set and serve as the natural orbitals of the system leading to the required input matrices $h_{ij}^0 = t_{ij} + v_{ij}$ and $w_{ij,kl}$. For their calculation

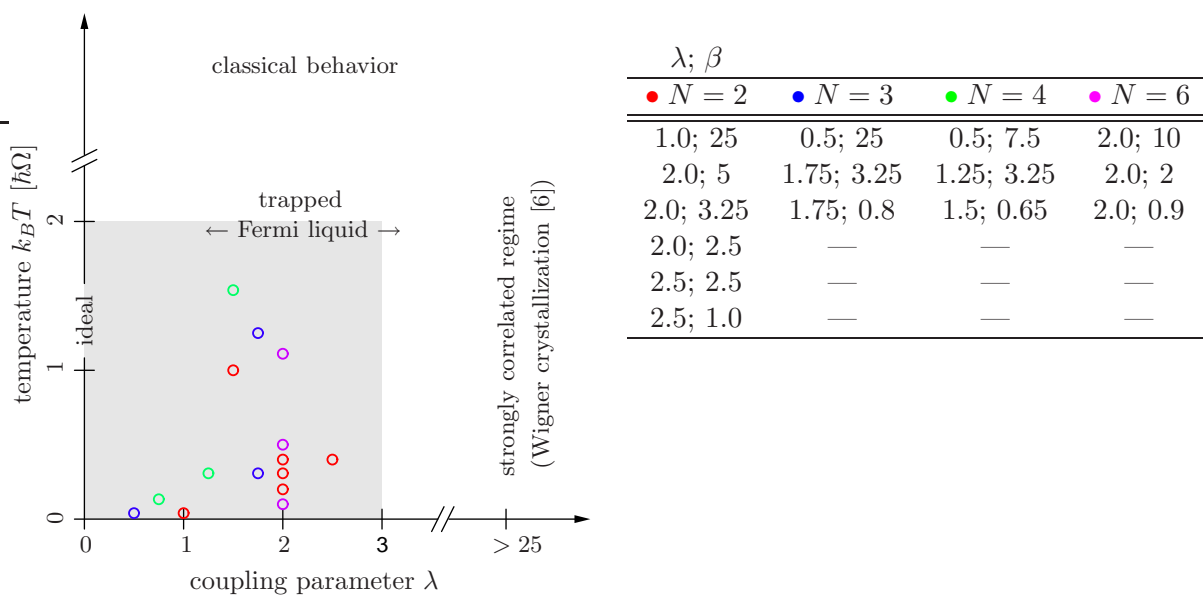


Figure 5.1: Temperature-coupling plane ($k_B T = \beta^{-1}, \lambda$) wherein a fixed point characterizes the N -particle state. The gray rectangle refers to the area of investigation in this chapter. Further, the colored points corresponding to the attached table indicate the particular numerical results as shown in Sect. 5.3.

the reader is referred to Appendix A which derives and summarizes all necessary quantities in the oscillator representation.

The present chapter is now organized as follows. After a brief review of the Hartree-Fock problem and a comparison with standard perturbation theory at quasi zero temperature in the first section, Sect. 5.2 analyzes the correlated Matsubara Green's function in terms of its time-dependent matrix elements. Sect. 5.3 then will focus on the received spatial densities, distribution functions and energies corresponding to the parameter ranges categorized in Fig. 5.1, and furthermore—in Sect. 5.4—some of the results are compared with path integral Monte Carlo simulations. Throughout, the investigations are restricted to small or moderate coupling parameters—only Sect. 5.3.2 discusses some aspects when going beyond a weakly interacting system.

5.1. Comparison with first order perturbation theory

From the Hartree-Fock equations, Eqs. (4.10) in Chap. 4, follow orbital energies and a respective total energy which are renormalized by the interaction treated in mean-field (HF) approximation. For small coupling parameters the total HF energies should thereby be comparable with perturbation theory (PT) results whose context will here be analyzed. If it is $\lambda < 1$, the interaction part of the Hamiltonian (5.1) can be regarded as a small correction to the ideal (noninteracting) system and—being familiar from standard text books on quantum mechanics, e.g. [52] or specifically [62]—the energy correction in first order perturbation theory is given by

$$\Delta E_{\text{PT},N}^{(0)} = \langle E_N^{(0)} | H_{12} | E_N^{(0)} \rangle, \quad (5.2)$$

where H_{12} corresponds to the disturbing part of the full Hamiltonian, $H = H_0 + H_{12}$, taking the form

$$H_{12} = \lambda \sum_{i < j}^N w(x_i - x_j) = \lambda \sum_{i < j}^N \left[\sqrt{(x_i - x_j)^2 + a^2} \right]^{-1}, \quad (5.3)$$

and $|E_N^{(0)}\rangle$ determines the N -particle state of the noninteracting system. Since subject of investigation is a fermionic ensemble, the ideal wave function is antisymmetric and can be formulated as a Slater determinant $S(\{\phi_i(x_j)\})$ of natural single-particle orbitals $\phi_i(x_j)$ which are eigenfunctions to H_0 , i.e. for the ground state at zero temperature it is

$$|E_N^{(0)}\rangle = \frac{1}{\sqrt{N!}} S_N(\{\phi_i(x_j)\}), \quad S_N(\{\phi_i(x_j)\}) = \sum_{\sigma \in \mathcal{P}_N} (-1)^{I(\sigma)} \prod_{j=0}^{N-1} \phi_{\sigma_j}(x_j), \quad (5.4)$$

where the prefactor $1/\sqrt{N!}$ accounts for normalization and $I(\sigma)$ denotes the number of inversions in the permutation σ . For $N = 2$, the Slater determinant simplifies to

$$|E_2^{(0)}\rangle = \frac{1}{\sqrt{2}} S_2(\{\phi_i(x_j)\}) = \frac{1}{\sqrt{2}} [\phi_0(x_1) \phi_1(x_2) - \phi_0(x_2) \phi_1(x_1)], \quad (5.5)$$

and the energy correction $\Delta E_{\text{PT},2}^{(0)}$ is evaluated with (5.3) to be

$$\begin{aligned} \Delta E_{\text{PT},2}^{(0)} &= \langle E_2^{(0)} | H_{12} | E_2^{(0)} \rangle \\ &= \frac{\lambda}{2} \int dx_1 dx_2 S_2^*(\{\phi_i(x_j)\}) w(x_1 - x_2) S_2(\{\phi_i(x_j)\}) \\ &= \frac{\lambda}{2} (w_{00,11} - w_{01,10} - w_{10,01} + w_{11,00}) \\ &= \lambda (w_{00,11} - w_{01,10}). \end{aligned} \quad (5.6)$$

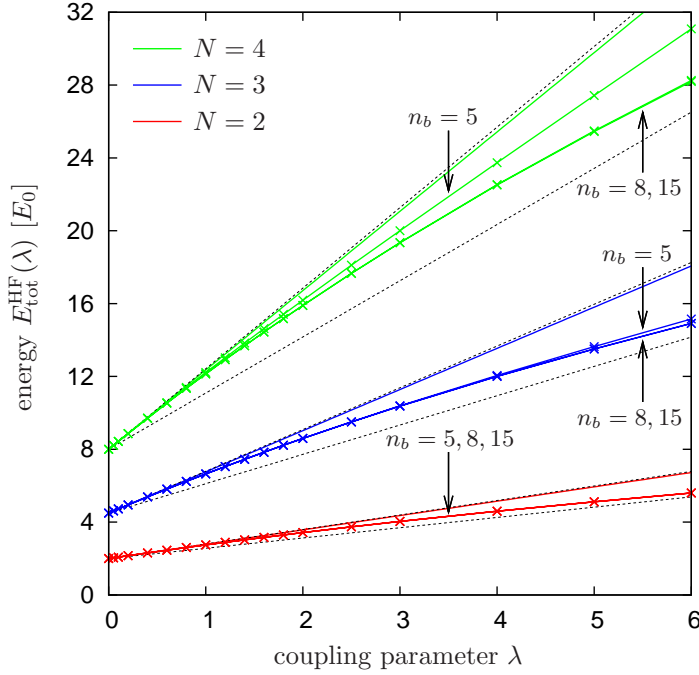


Figure 5.2: Quasi zero temperature ($\beta = 50$) Hartree-Fock energies $E_{\text{tot}}^{\text{HF}}(\lambda)$ for different particle numbers. The HF energies \times are compared with first order perturbation theory in λ (colored straight lines). All colored curves refer to the small parameter $a = 0.1$ —the black dashed lines indicate the perturbative result for $a = 0.01$ (upper line) and $a = 1.0$ (lower line), respectively. n_b indicates the number of basis functions used within the numerical computation.

Thereby, the two-dimensional integrals $\int \dots dx_1 dx_2$ have been identified with the two-particle matrices $w_{ij,kl}$ and their symmetry properties (see Appendix A.2.2) have led to the last equality. For $N \geq 3$, the calculation of the energy correction is difficult because the number of involved terms is scaling with $\frac{N(N-1)}{2} (N!)^2$, which in particular makes the evaluation impossible for large N . However, numerical access is realizable for moderate $N = 3 \dots 5$, where the summation of terms is performed under application of the symmetry properties for $w_{ij,kl}$. As a result, the first order energy correction to be added to the undisturbed energy $E_{0,N}$ is (of course) linear in the coupling λ and the proportionality factor follows as a sum over the quantities $w_{ij,kl}$ which are known since they also enter the Hartree-Fock equations.

For the special case of harmonic confinement and single-occupied orbitals (spin-polarized system), the undisturbed energy is given by $E_{0,N} = \sum_{k=0}^{N-1} (k + \frac{1}{2})$. Fig. 5.2 shows, how this energy now changes in the presence of finite coupling parameters λ , whereby the Hartree-Fock result is compared with the perturbative one for up to $N = 4$ particles. For $\lambda < 1$, both results (colored curves) are in good agreement and from the related Table 5.1 one can extract a deviation of about 1% and less—results for larger N thereby differ more which is explained by the increasing number of interactions $w(x_i - x_j)$ that contribute in H_{12} . Further, the calculations are carried out with a small parameter $a = 0.1$ (in units of the oscillator length x_0) in expression (5.3). The black dashed lines in Fig. 5.2 however correspond to the perturbative result for $a = 1$ and 0.01,

$n_b = 15$:

λ	$N = 2$	$N = 3$	$N = 4$
0.4	2.3087 (2.315)	5.3857 (5.405)	9.7066 (9.743)
1.0	2.7487 (2.788)	6.6480 (6.761)	12.1395 (12.357)
1.4	3.0276 (3.103)	7.4489 (7.666)	13.6846 (14.100)
2.0	3.4259 (3.575)	8.5946 (9.023)	15.8982 (16.715)
2.5	3.7406 (3.969)	9.5024 (10.153)	17.6554 (18.894)
3.0	4.0408 (4.363)	10.3707 (11.284)	19.3396 (21.072)

Table 5.1: Selected Hartree-Fock energies referring to Fig. 5.2. Numbers in brackets indicate the results obtained from first order perturbation theory (PT). At $\lambda = 1.0$, the error of PT is about 1 – 2%, at $\lambda = 3.0$ about 8 – 9%. ($\beta = 50, a = 0.1$).

respectively, and indicate that a pure Coulomb-potential with $a \equiv 0$ is relatively well approximated when using for a about a tenth of x_0 . This is in particular important for comparison with quantum Monte-Carlo (QMC) results in Sect. 5.4 where only simulations with pure Coulomb interaction had been available.

Some additional information is contained in Fig. 5.2: As can be seen in addition, the number of basis functions n_b —being included to solve the Hartree-Fock equations—has only a minor effect on the total Hartree-Fock energy $E_{\text{tot}}^{\text{HF}}$. Especially, for $n_b \gtrsim 8$ there is good convergence which justifies that the restriction to a relatively small basis set is adequate for small to moderate coupling parameters.

As a final remark it is worth mentioning that special symmetry properties of the interaction potential w may lead to a vanishing energy correction as the different terms entering Eq. (5.6) can cancel each other. For example, when one replaces the potential (5.3) according to $w(x_i - x_j) \rightarrow \delta(x_i - x_j)$ by an on-site or contact interaction, the value of $w_{ij,kl}$ does not depend on the order of the four indices—see Appendix A.2.1 for discussion and derivation of the matrix elements. Thus, the perturbative energy correction equals zero balancing the Hartree and Fock contribution. However, this is not just the special property of Eq. (5.3) or Eq. (4.9) in Sect. 4.1 but is a general key feature of contact interacting trapped fermions which is known in the literature [63], and from the expression for the correlation part of the self-energy—see Eq. (4.39) of Sect. 4.3.1—one further concludes that there exist no correlations at all.

5.2. The correlated Matsubara Green's function

The correlated Matsubara Green's function satisfying the Dyson equation (4.20) appears as the matrix $\mathbf{g}^M(\tau)$ whereby each element $g_{ij}^M(\tau)$ is a function of the relative time $\tau = \tau_1 - \tau_2 \in [-\beta, \beta]$ with τ_1 and τ_2 being defined on the imaginary part of the Keldysh-contour. Further, since the Matsubara Green's function and the respective self-energy obey the anti-periodicity property $\mathbf{g}^M(\tau + \beta) = -\mathbf{g}^M(\tau)$ and $\Sigma^M(\tau + \beta) = -\Sigma^M(\tau)$, respectively, it is possible (in Sect. 4.3) to restrict the numerical solution of the Dyson equation to $\tau \in [-\beta, 0]$. On this time interval both the Hartree-Fock and the correlated quantities have been computed by the scheme explained in the previous chapter and their structure shall be briefly described in the following.

In Fig. 5.3 and Fig. 5.4, the diagonal elements of the Green's function $\mathbf{g}^M(\tau)$ and the dynamic self-energy $\Sigma^{\text{corr}}(\tau)$ are shown in dependence on τ . Subject of investigation has thereby been a system of three trapped fermions at temperature $\beta = 2$ and coupling $\lambda = 1.6$.

As can be seen, all matrix elements of the uncorrelated Hartree-Fock Green's function (blue dashed lines) are exponentially decaying according to their definition (4.19) in Sect. 4.2. Due to the different occupations of the HF levels (they obey the exact Fermi distribution $f(\beta, \{\epsilon_i\}, \mu)$) the curves corresponding to the three lowest—and most occupied—states are peaked around $\tau = 0$ and all others are dominating around $\tau = -\beta$. This behavior is dictated by the subtraction of the chemical potential μ in the exponential function $e^{\tau[\epsilon_i - \mu]}$ entering the definition.

The correlated Green's function in full second Born approximation then shows a similar imaginary time-dependence. However, the decaying behavior (see red and green lines in Fig. 5.3) is now renormalized by the particle-particle correlations leading to curves with in general lower slopes $\partial_\tau \mathbf{g}^M(\tau)$. As it can be extracted especially from Fig. 5.3 (b) showing the logarithm of $\mathbf{g}^M(\tau)$, the time-dependence differs from a pure exponential function as it is obtained for the HF case. In total, the correlated Green's function is thereby mostly modified around the end-points of the τ -interval. In the same way as the Green's function then behaves the dynamic self-energy $\Sigma^{\text{corr}}(\tau)$ (Fig. 5.4) which however does not appear in the mean-field (HF) treatment.

Moreover, the off-diagonal elements of the correlated quantities are in general non-zero and—showing similar time-dependences—influence the system properties. Only due their typically

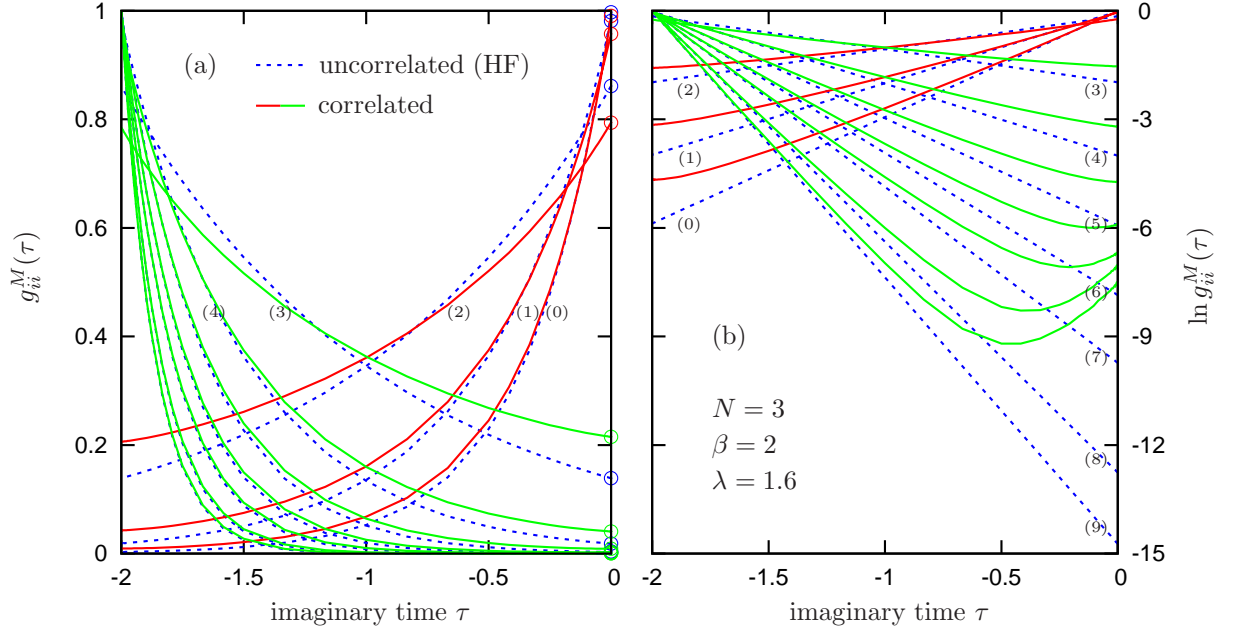
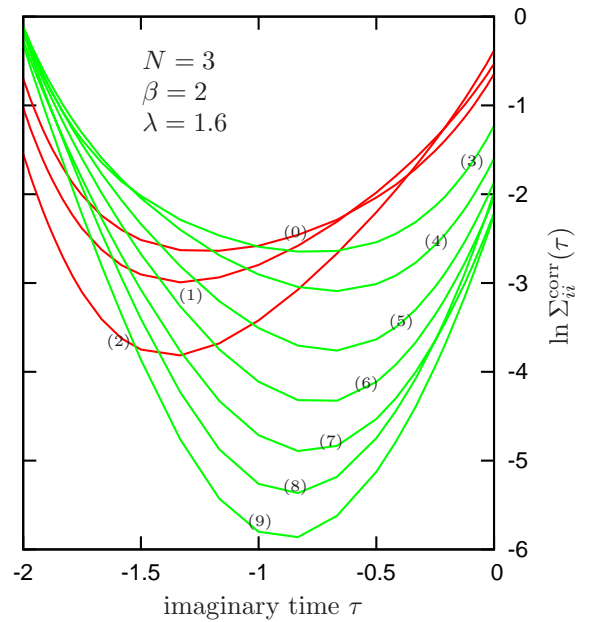


Figure 5.3: (a) Diagonal elements of the uncorrelated (HF) and correlated (HF + 2nd Born) Matsubara Green's function matrix $\mathbf{g}^M(\tau)$ for $N = 3$ trapped fermions. System parameters are as indicated within the figure and the numbers in brackets state the Hartree-Fock levels i . Only for clarity the curves for the correlated GF have been differently inked depending on the occupation of the HF levels. The circles \circ further denote the diagonal elements of the density matrix according to $\rho_{ii} \equiv g_{ii}^M(0^-)$. Applied uniform power-mesh: $(u, p) = (3, 9)$. (b) Logarithm of the Matsubara Green's function as shown in Fig. (a). The Hartree-Fock GF (blue dashed curves) is thereby a pure exponential function.

Figure 5.4: Logarithm of the dynamic self-energy $\Sigma^{\text{corr}}(\tau)$ in dependence on the imaginary time-argument τ . Shown are only the diagonal matrix elements of Σ^{corr} with $i = j$ which are peaked at the boundaries $\tau = -\beta$ and $\tau = 0$ similar to the Matsubara Green's function. The system parameters, the indexing of the curves and the color scheme are as in Fig. 5.3.



small contribution in comparison with the diagonal terms they are not shown in the figures.

Besides the full time-dependence of the quantities which e.g. is necessary to compute the correlation energy according to Eq. (4.44), also the limit $\tau \rightarrow 0^-$ is of interest since it directly corresponds to the density matrix, i.e.

$$\rho_{ij} = \lim_{\tau \rightarrow 0^-} g_{ij}^M(\tau) \equiv g_{ij}^M(0^-), \quad (5.7)$$

in the static Hartree-Fock (mean-field) basis. As shown in Fig. 5.3 (a) for the diagonal elements, the density matrix has clearly changed due to the inclusion of correlation effects. More precisely, the average occupation numbers ρ_{ii} of the lowest HF orbitals are decreased accompanied with an increased excitation of the higher states. This has of course essential influence on the macroscopic density and the different energy contributions. The latter aspect is reflected in Table 5.2 where the result for the correlated Matsubara Green's function (MGF) indicates an increase in the single-particle energy (kin. + pot. energy) compared with the HF result. However, this does not necessarily mean that also the total energy increases since the correlation energy in general yields a negative correction and the HF energy may change as well. For a more detailed discussion on this topic the reader is referred to the numerical results presented in Sect. 5.4.

5.2.1. Effective potential in coordinate space

For the correlated thermodynamic equilibrium state it is possible to compute an effective single-particle potential $\Omega^{\text{eff}}(x)$ which besides a mean-field also takes correlation effects into account. This effective potential can thereby be written in the form $\Omega^{\text{eff}}(x) = \Omega^0(x) + \delta\Omega(x)$, where the single-particle or confinement potential $\Omega^0(x)$ is modified by a correction term $\delta\Omega(x)$ induced by the particle interactions. The Matsubara self-energy $\Sigma^M(\tau)$ entering the Dyson equation then acts as the reference quantity from which an expression for $\delta\Omega(x)$ can be derived—especially the dynamic part is responsible for the correction beyond mean-field approximation.

Transferring the Matsubara self-energy $\Sigma^M(\tau)$ back into its space-time coordinate representation, i.e. reinserting sets of Hartree-Fock orbitals $\Phi_m(x) = \sum_n A_{mn} \phi_n(x)$, yields the quantity $\Sigma^M(x_1, x_2; t_0 - i\tau)$ which in terms of the center of mass coordinate $x = (x_1 + x_2)/2$ can be understood as the contribution $\delta\Omega(x)$ to the effective potential. However, $\Sigma^M(x; t_0 - i\tau)$ still depends on the relative time-argument τ , so that one, in addition, has to integrate over the imaginary part of the contour. This leads to

$$\begin{aligned} \delta\Omega^{\text{eff}}(x) &= \int_0^\beta d\tau \Sigma^M(x_1, x_2; t_0 - i\tau) \Big|_{x_1=x_2=x} \\ &= \int_0^\beta d\tau \sum_{kl} \Phi_k(x_1) \Phi_l^*(x_2) \Sigma_{kl}^M(\tau) \Big|_{x_1=x_2=x}, \end{aligned} \quad (5.8)$$

where in particular, one can distinguish the following two contributions:

energies	HF	MGF	difference
total energy	8.13170	8.18712	+0.05542
kinetic energy	1.72627	1.83574	+0.10946
potential energy	3.26826	3.36142	+0.09316
kin. + pot. energy	4.99453	5.13060	+0.13607
HF energy	3.13717	3.27437	+0.13721
correlation energy	—	-0.217855	—

Table 5.2: Different energy contributions (in E_0) as obtained from the solution of the Dyson equation for $N = 3$ trapped fermions. System parameters: $\beta = 2$ and $\lambda = 1.6$.

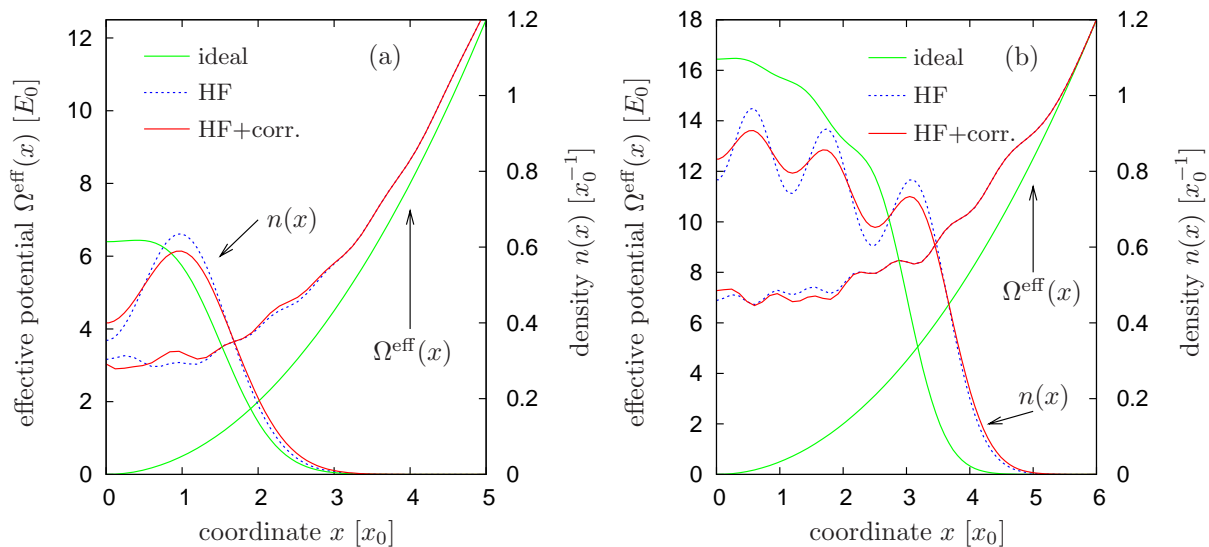


Figure 5.5: Effective potential $\Omega^{\text{eff}}(x)$ as it is obtained for $N = 2$ trapped fermions at $(\beta, \lambda) = (2.5, 2.0)$ (a) and $N = 6$ fermions at $(2.0, 2.0)$ (b). The contribution of the dynamic self-energy to the effective potential is small and the oscillations avoid a straightforward explanation of the density change $n^{\text{HF}}(x) \leftrightarrow n^{\text{HF+corr}}(x)$. The oscillations of $\Omega^{\text{eff}}(x)$ thereby indicate errors due to the limitation to a finite Hartree-Fock basis ($n_b = 14$). The density is given in units of the inverse oscillator length x_0 .

i. Hartree-Fock correction to the potential:

$$\delta\Omega^{\text{HF}}(x) = \sum_{kl} \Phi_k(x) \Phi_l^*(x) \Sigma_{kl}^{\text{HF}}. \quad (5.9)$$

ii. Correlation induced correction:

$$\delta\Omega^{\text{corr}}(x) = - \sum_{kl} \Phi_k(x) \Phi_l^*(x) \int_0^\beta d\tau \Sigma_{kl}^{\text{corr}}(-\tau). \quad (5.10)$$

The numerical analysis of $\Omega^{\text{eff}}(x)$ is somewhat difficult since the spatially resolved self-energy expression $\Sigma^M(x_1, x_2)$ turns out to be very sensitive to the size of the HF basis and appears as quite oscillatory. The number of used HF orbitals n_b has thereby much more influence on $\Sigma^M(x_1, x_2)$ than it has e.g. on spatial density or total energy which are quantities additionally averaged over the generalized density matrix $\mathbf{g}^M(\tau)$. From this follows that $\Omega^{\text{eff}}(x)$ is only well converged when using a large number of HF orbitals—however, numerical simulations of such size are not directly available.

Fig. 5.5 shows how the parabolic confinement potential $\Omega^0(x) = x^2/2$ is modified due the presence of the Hartree-Fock mean-field (blue dashed line) and the additional correlation contribution (red line) for different numbers of particles in the trap. The HF contributions in Figs. (a) and (b)—apart from the oscillatory behavior—indicate a more flat potential in the trap center (in comparison with $\Omega^0(x)$) which is consistent with the resulting density profile and typical HF energy level spacings of $\Delta\epsilon < 1$ (cf. Sect. 4.1.1). Furthermore, the correspondence of the correlation induced change of the effective potential to the density change is not that clear due to the oscillations. Thus, a simple physical interpretation of the red curves including the correlation contributions $\delta\Omega^{\text{corr}}(x)$ is not possible.

When investigating systems with a smaller coupling parameter, the errors in $\delta\Omega^{\text{eff}}(x)$ typically decrease—however, $\delta\Omega^{\text{corr}}(x)$ then appears as a very small correction being difficult to analyze.

5.3. Density profile, distribution function and energies

In this section, the equilibrium state of 1D harmonically confined fermions—interacting according to (5.1)—is investigated in dependence on particle number N , inverse temperature $\beta = (k_B T)^{-1}$ and coupling parameter λ . The observables to be shown are thereby obtained from numerical data for the matrices $\mathbf{g}^M(\tau)$, $\mathbf{\Sigma}^M(\tau)$ and \mathbf{h}^0 , which are the three main quantities entering the Dyson equation (4.20). More precisely, the distribution function $f(\epsilon_k - \mu)$ and the spatially resolved particle density $n(x)$ follow from the density matrix $\rho_{kl} = g_{kl}^M(0^-)$ according to

$$f(\epsilon_k - \mu) = \rho_{kk} , \quad n(x) = \sum_{kl} \Phi_k(x) \Phi_l^*(x) \rho_{kl} . \quad (5.11)$$

where $\Phi_k(x)$ are the HF orbitals. The energy of the system is then computed according to the formulas (4.41-4.44) in Sect. 4.3.2. The results to be presented in this section can further be divided into two classes:

- **Zero temperature limit.**

In the limit $\beta \rightarrow \infty$, the quantum ground state of the interacting N -particle system is obtained with a minimum total energy. Although the numerical procedure requires a finite value of β , this ground state is well realized when the temperature is sufficiently low excluding any thermal excitation processes, i.e. in particular $\beta \gg \hbar\Omega$ (typically $\beta \gtrsim 25 \hbar\Omega$) for a trapped ensemble with bound states separated by energy gaps of the order of $\hbar\Omega$.

Moreover, for $\lambda \rightarrow 0$ one exactly recovers the properties of the noninteracting system, which has been explored e.g. by Gleisberg *et al.* [64] or Vignolo and Minguzzi [65]. To give an impression how the ideal density profile looks like, it is referred to Fig. 5.6 (a).

- **Properties at finite temperatures.**

At finite temperatures, the interplay of the thermal motion of the quantum particles and the repulsive interactions determines the equilibrium state of the trapped ensemble. Especially, particle-particle correlations will affect the macroscopic observables in this regime.

Again, for $\lambda \rightarrow 0$ the corresponding properties of the ideal system are obtained—Fig. 5.6 (b) for instance shows the density profile for $N = 4$ fermions at different temperatures which agree with the grand canonical results stated in the work of Akdeniz *et al.* [66], which is based on both exact and semi-classical grounds.

As already mentioned in the beginning of this chapter—remember Fig. 5.1—the results to be shown lie in a parameter range of $\lambda \in [0, 3]$ and correspond to temperatures $k_B T / \hbar\Omega \in [0, 2]$. For particle numbers of $N = 2, 3, 4, 6$ the sequent Figures 5.7 to 5.11 now show the spatial density profile $n(x)$ and the respective distribution function $f(\epsilon_i - \mu)$ in terms of the HF orbital energies ϵ_i . Thereby, the correlated result, indicated throughout as n_M and f_M , respectively, is compared with the one obtained in Hartree-Fock approximation (n_0, f_0). In addition, the equilibrium behavior of the noninteracting system is given by n_{ideal} and f_{ideal} . Bear in mind, that the small parameter has been chosen to $a = 0.1$ and, further, that the results include all four (direct *and* exchange) self-energy diagrams in their numerical computation, i.e. presented are results in full second Born approximation. For a different discussion, see Sect. 5.3.2.

Apriori, the physics shall be described for the most simple case of two interacting fermions. As can be seen from Fig. 5.7 (a) for quasi zero temperature and $\lambda = 1$, the ideal particle density is altered by the repulsive interaction leading to a broadened profile whereby the probability to find a single fermion in the trap center decreases. In comparison with the HF profile (blue dashed curve) the influence of the correlations (red curve) is negligibly small and, further, the

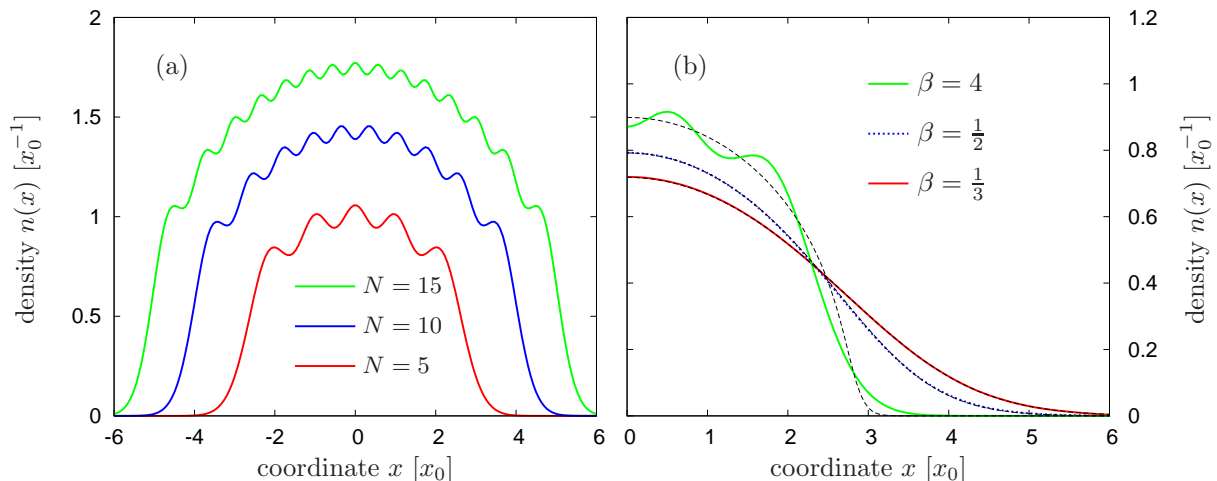


Figure 5.6: (a) Exact particle density $n(x)$ at quasi zero temperature $\beta = 50$ for different numbers of (ideal) noninteracting fermions as obtained from the Matsubara Green's function. $n(x)$ is symmetric about the trap center. (b) Particle density for $N = 4$ ideal fermions at different finite temperatures. The black dashed curves indicate the results obtained from a semi-classical LDA¹ (local density approximation) calculation, where in the limit $\beta \rightarrow \infty$ the density profile is given by inverted parabolas [66].

corresponding distribution functions (Fig. 5.8 (a)) are practically identical showing a sharp Fermi edge in terms of the discrete renormalized HF energies. As the temperature as well as the coupling parameter increase one notices (see Figs. (b) to (f)) that the profile gets further enlarged and in particular the difference between the Hartree-Fock and the correlated result becomes more obvious. The correlation effects thereby lead to a maximum around $x = 1$ which is not that pronounced than in HF approximation. In addition, the distribution function changes from an exact Fermi distribution (in the HF case) to a modified distribution, where the average occupations of energetically lower lying orbitals is reduced and particles are scattered into higher states due to collisions, i.e. more spectral weight is found above the Fermi energy [63]—this is the point already exemplified at the end of Sect. 5.2.

If one further increases the temperature to about $k_B T \approx \hbar\Omega$, i.e. to the order of the energy level spacings, one obtains—according to Fig. (e)—a density profile which is nearly constant in the center trap region and slopes down to zero for $x > 1$. In particular, the influence of the correlations is thereby reduced in the sense that only a slight broadening occurs.

In principle, a similar dependence on temperature and coupling parameter is also found for larger particle numbers. However, some more features are analyzable here. Besides that the density profile spreads out due to adding of particles to the trap—consequently accompanied by a widened distribution function—the density starts clearly to oscillate in the inner trap region for low to moderate temperatures (see also Fig. 5.6 (a)). Such oscillations are in the literature, e.g. [63, 67], usually referred to as Friedel oscillations [68] and are strongly affected by repulsive or attractive interactions. As can be seen from Figs. 5.9 to 5.11, both the HF and the correlated result essentially modifies this oscillatory behavior of the density in comparison with the ideal profile, whereby the correlations in general lead to a damping of the amplitude.

¹In an LDA description, the spatial density of ideal harmonically trapped fermions is given by [66]

$$n(x, \beta, \mu) = \frac{1}{2\pi} \int dp \frac{1}{e^{\beta[H(p,x) - \mu]} + 1} = -\frac{1}{\sqrt{2\pi\beta}} \text{Li}_{1/2}(-\exp(\beta[\mu - x^2/2])), \quad (5.12)$$

where $H(p, x) = (p^2 + x^2)/2$ denotes the classical Hamilton function, $\text{Li}_n(z) = \sum_{k=1}^{\infty} z^k/k^n$ is the polylogarithm function and the chemical potential follows from normalization of the distribution function.

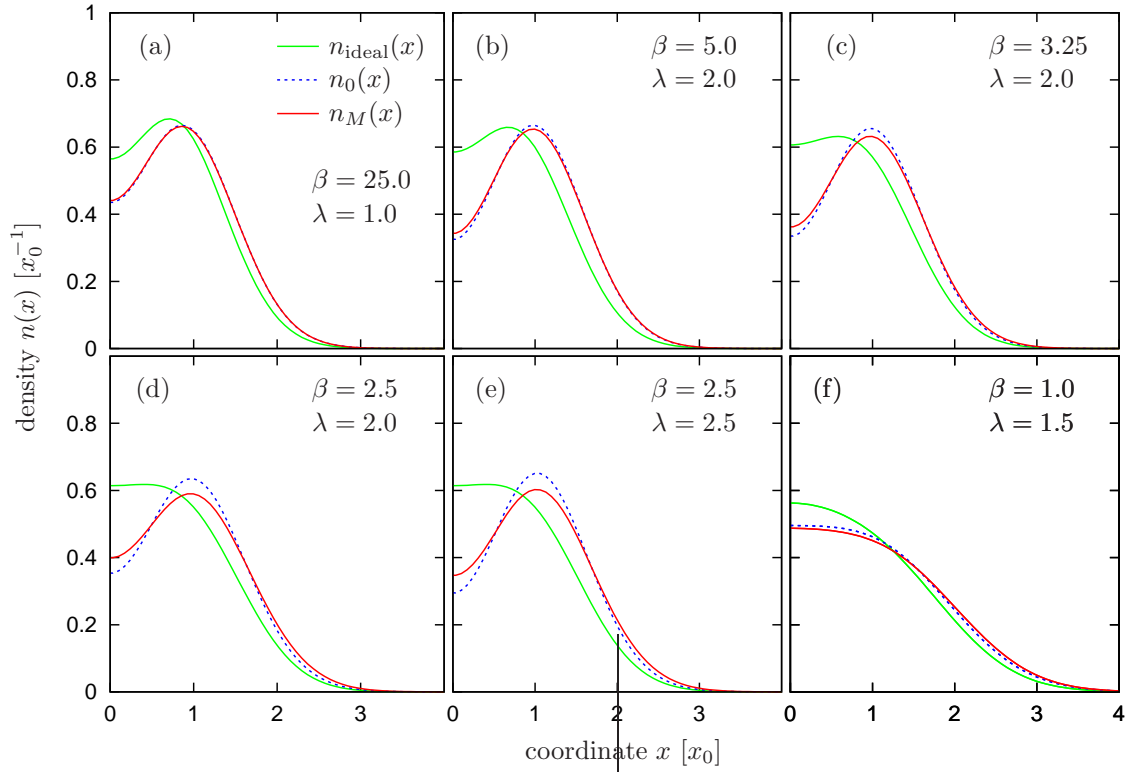


Figure 5.7: Spatial density profile $n(x)$ for $N = 2$ fermions for different parameters (β, λ) . $n_0(x)$ denotes the density profile in Hartree-Fock and $n_M(x)$ in second Born approximation, respectively.

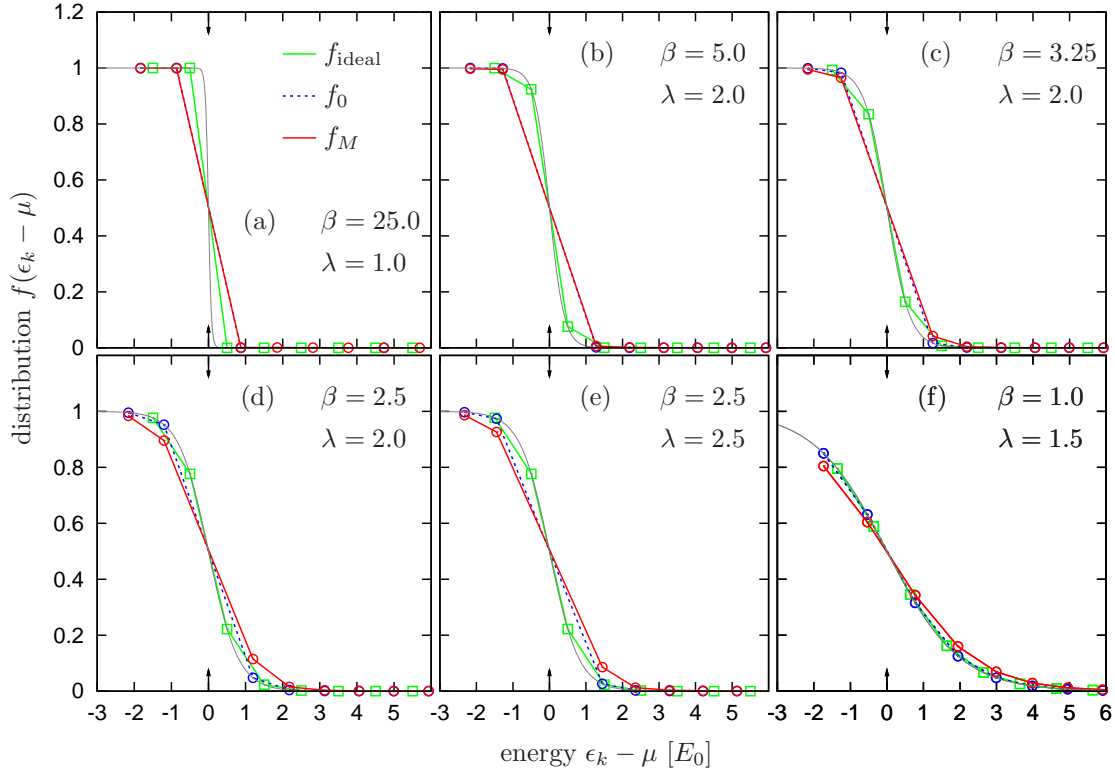


Figure 5.8: Distribution function $f(\epsilon_k - \mu)$ corresponding to Fig. 5.7, $N = 2$. f_0 gives the Hartree-Fock result and f_M indicates the second Born approximation. The symbols \square denote the energies ϵ_k^0 of the ideal system. The Hartree-Fock renormalized energies ϵ_k are indicated by \circ .

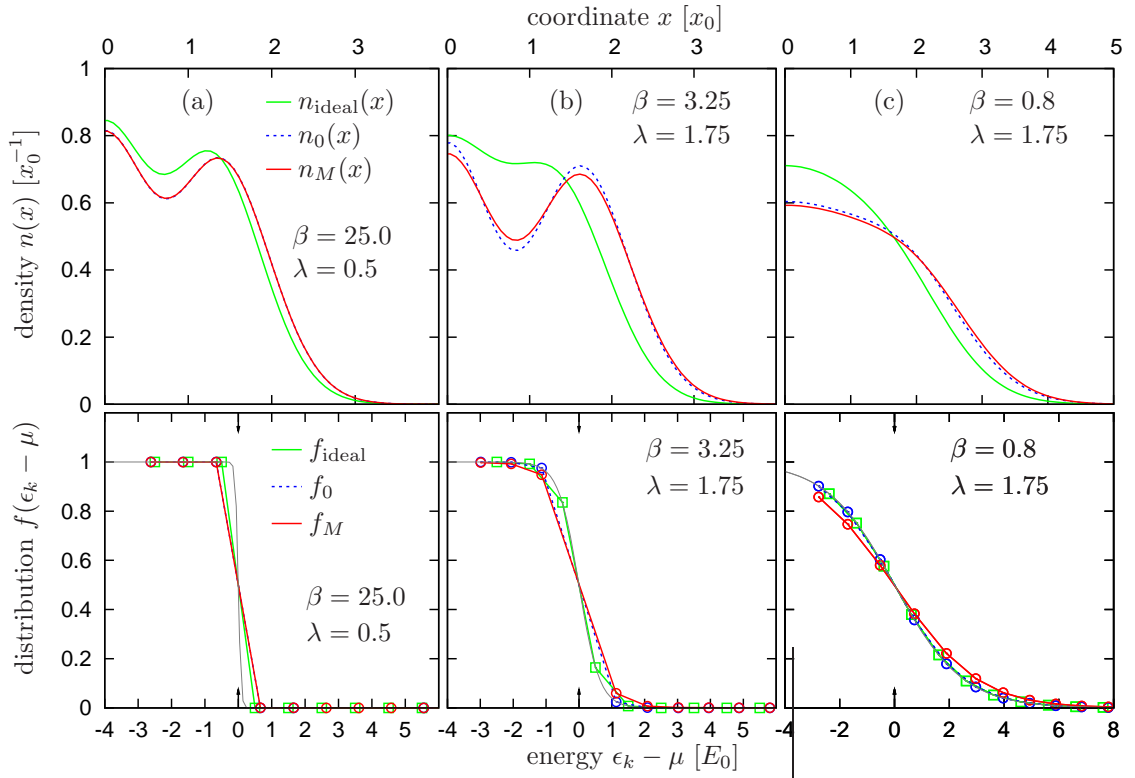


Figure 5.9: Spatial density profile $n(x)$ and distribution function $f(\epsilon_k - \mu)$ for $N = 3$ fermions. Notation as in Figs. 5.7 and 5.8.

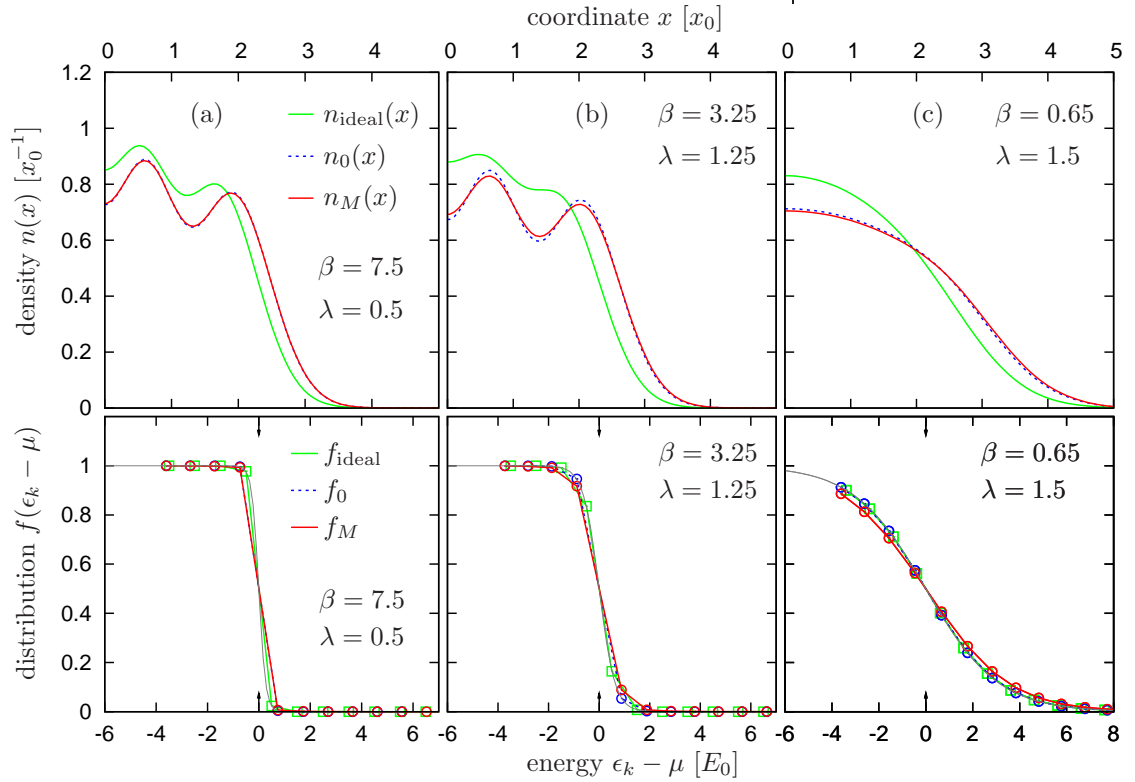


Figure 5.10: Spatial density profile $n(x)$ and distribution function $f(\epsilon_k - \mu)$ for $N = 4$ fermions. Notation as in Figs. 5.7 and 5.8.

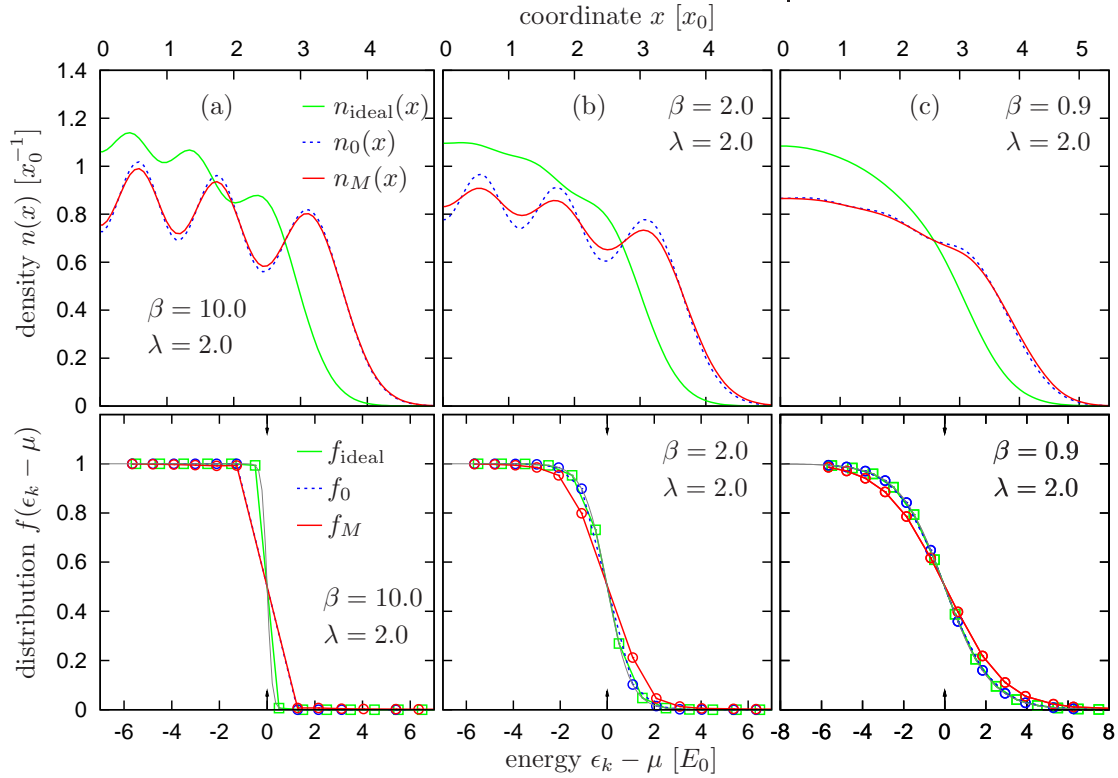


Figure 5.11: Spatial density profile $n(x)$ and distribution function $f(\epsilon_k - \mu)$ for $N = 6$ fermions. The Friedel oscillations of the inner particle density are strongly affected by the interaction in general and by correlation effects in particular for moderate temperatures $\beta \approx 2$. Notation as in Figs. 5.7 and 5.8.

In summary, correlations play an important role for the particle density for temperatures around $\beta \approx 2$, while for lower and higher temperatures the profile turns out to be less sensitive. The general trend in dependence on λ is thereby that—as one would expect—the correlation effects generally increase for higher coupling parameters.

To conclude this section, it is worth investigating the different energies contributing to the total energy of the trapped ensemble. Besides the single-particle energy which splits into the potential and the kinetic part there appear in mean-field approximation the Hartree-Fock energy, and in addition—if collisions are included in the Matsubara Green’s function—the correlation energy contributes as well.

In contrast to the ideal system where from the virial theorem potential and kinetic energy follow to be identical in the parabolic confinement, the presence of an additional repulsive interaction with $\lambda \neq 0$ leads to the potential energy being always larger than the kinetic energy. This can be verified by Tables 5.3 and 5.4 which list the energy contributions for $N = 2$ and $N = 6$ interacting fermions, respectively. The energies are thereby subdivided into the result obtained from the uncorrelated (HF) Green’s function and the correlated Matsubara Green’s function (MGF). For coupling parameters $\lambda \gtrsim 2$, the single-particle energy and the HF energy typically approach the same order of magnitude, and both generally increase when including correlation effects. The latter behavior is thereby well explained by the particle collisions which stimulate the motion of the particles in the trap and lead—besides increasing the kinetic energy—to a deformation of the the mean-field potential.

Furthermore, the correlation energy is small compared with the other contributions and in particular appears as a negative correction to the HF energy. One thereby roughly approximates an amount of less than 10% of the total energy per particle. How the total energy finally changes

energies	$\lambda = 2.0$			$\lambda = 2.5$		
	HF	MGF	difference	HF	MGF	difference
total energy	3.77187	3.85262	+0.080750	3.52293	3.60382	+0.080899
kin. energy	0.76442	0.79823	+0.033806	0.78878	0.84106	+0.052284
pot. energy	1.50612	1.57487	+0.068751	1.43119	1.50167	+0.070482
kin. + pot. energy	2.27055	2.29450	+0.023955	2.21997	2.27853	+0.058566
HF energy	1.50132	1.69691	+0.195584	1.30296	1.45781	+0.154851
correlation energy	—	-0.13879	—	—	-0.13252	—

Table 5.3: Different energy contributions corresponding to the densities of $N = 2$ trapped fermions shown in Fig. 5.7 (d) and (e), respectively. The inverse temperature is $\beta = 2.5$.

when particle collisions are included in the computation of the equilibrium state strongly depends on the negative value of the correlation energy (see also Fig. 5.12 and discussion).

Moreover, for the special case of $N = 3$ interacting fermions in the trap, the energies have been investigated in dependence on the temperature $k_B T = \beta^{-1}$. Fig. 5.12 indicates the interplay of the different contributions.

For $k_B T \rightarrow 0$, the HF and the MGF result are nearly identical. However, the correlation energy is non-zero leading to a small deviation in the HF energies and, thus, also the total energy is slightly smaller for the correlated result. For temperatures $k_B T > 0.25$ both results begin to differ essentially more due to an increased importance of correlation effects. Consequently, E_{corr} starts to become more negative and—as one would expect—there is (apart from E_{corr}) most difference in the kinetic energy E_{kin} . In particular, the total energy is now larger for the correlated case. Further, the potential and kinetic energy, i.e. the whole single-particle energy, generally increase with temperature. For $k_B T > 1.5$, the correlation energy as well as the Hartree-Fock energy then seem to saturate and the total energy per particle approaches its classical limit of $E_{\text{tot}} \propto k_B T$. In summary, one can establish that the correlations—treated in

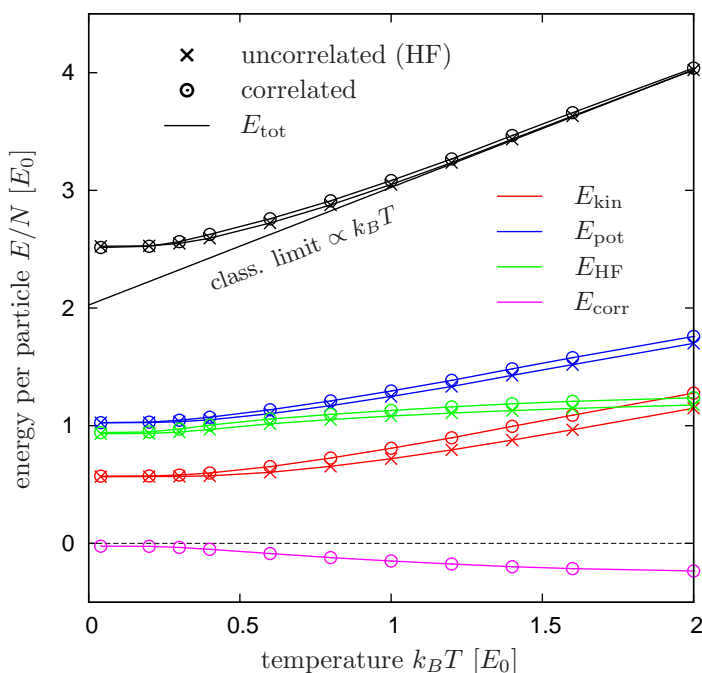


Figure 5.12: Temperature-dependence of the different energy contributions and the total energy for $N = 3$ fermions. All energies are displayed in units of $E_0 = \hbar\Omega$ per particle. The crosses \times denote the result for the Hartree-Fock Green's function and the circles \circ indicate the energies obtained from the correlated Matsubara Green's function. The coupling parameter has been chosen to $\lambda = 1.5$. As the temperature increases the total energy approaches its classical limit of $E_{\text{tot}} \propto k_B T$ (black straight line).

$(\beta = 2.0, \lambda = 2.0)$	HF	MGF	difference
total energy	36.4719	36.4705	-0.001396
kinetic energy	5.97484	6.1405	+0.165681
potential energy	14.0440	14.2088	+0.164771
kin. + pot. energy	20.0189	20.2018	+0.182962
HF energy	16.4531	16.7764	+0.323325
correlation energy	—	-0.507682	—

Table 5.4: Energy contributions for the system of $N = 6$ trapped fermions. The results correspond to the density and distribution function shown in Fig. 5.11 (b).

second Born approximation—do mainly redistribute the different energy contributions and there is a minor but nevertheless not negligible effect on the total energy of the particle ensemble.

5.3.1. Computations without exchange

As stated in Sect. 4.4 explaining the program structure, the numerical procedure allows in equilibrium and nonequilibrium to "turn off" the exchange contributions to the self-energies—evoke the diagrammatic summation shown in Fig. 3.2, Sect. 3.3.1. This means that in first order only a Hartree calculation and in second order a correlated calculation without implying any exchange processes is performed. To do so, one of course will end up with different results for the macroscopic observables since the exchange potential by entering Eqs. (4.38) and (4.39) essentially affect them. In addition, one should not ignore that these results do not directly apply to physical fermions as e.g. electrons, specific atoms or other spin-half particles, because, when the particles are interacting, the exchange potential is an indispensable key feature which actually cannot be neglected. In this sense these results will be unphysical or at least inadequately approximated. Nevertheless, it is interesting to compare both results, i.e. when including *and* neglecting the exchange contributions, respectively.

Since the exchange potential—considering fermions only—is subtracted from the (direct) Hartree potential in a mean-field treatment (note that a similar structure is found in the higher order self-energy expressions), the corrections to the noninteracting part of the Hamiltonian induced by the interaction are in general much larger when neglecting exchange processes. Therefore, the equilibrium Green's function should yield e.g. a higher total energy and a different particle density. Further, one also will be limited to a smaller range of coupling parameters manageable by the numerics since the iterative procedure solving the Dyson equation not necessarily does still converge: Empirically, $\lambda < 1$ is required for convergence within acceptable bounds and CPU time.

While Fig. 5.13 (a) now shows the spatial density for $N = 4$ particles when the exchange potential is neglected, Fig. (b) gives the full result where all exchange diagrams have been included. Both figures refer to the same coupling parameter of $\lambda = 0.6$ and to the same temperature of $\beta = 4.0$. As one sees, the profiles extremely differ from each other, and correspondingly the obtained total energies do not agree. In the figure to the right, the exchange effects thereby leads to a stronger localization of the fermions which is a direct consequence of the Pauli exclusion principle not taken into account for the interaction between the particles in Fig. (a). In contrast, when exchange effects are being neglected, the influence of the correlations is much more pronounced—leading to an almost smooth density profile.

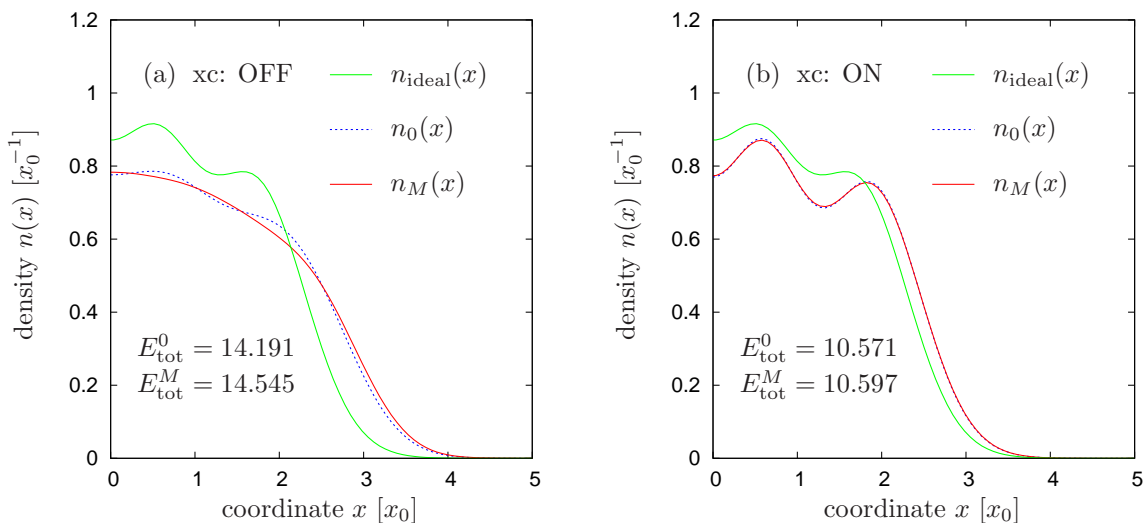


Figure 5.13: Influence of exchange effects on the particle density $n(x)$. System parameters: $N = 4$ confined fermions, $\beta = 4.0$ and $\lambda = 0.6$. (a) Density profile neglecting exchange processes (xc: OFF), (b) including exchange (xc: ON). Each figure thereby displays the HF result $n_0(x)$ as well as the correlated result $n_M(x)$ and the corresponding total energy. The green lines indicate the ideal density profile $n_{\text{ideal}}(x)$.

5.3.2. Strongly coupled fermions in thermal equilibrium

The series of numerical results shown above is associated with a weakly interacting system according to coupling parameters $\lambda \in [0, 3]$, and the thermal equilibrium states show a Fermi liquid behavior. The question that now arises is if one can drive a numerical procedure solving the Dyson equation also for larger couplings and, thus, investigate trapped fermions in a strongly correlated regime [69]. In the limit $\lambda \rightarrow \infty$, Wigner crystallization—as e.g. found for two-dimensional mesoscopic electron systems in Ref. [6]—should then be observable in combination with thermal and quantum melting processes.

As already mentioned in connection with the exchange potential in the previous subsection, Sect. 5.3.1, the problems considering large λ -values lie in the convergence properties of the self-consistent procedures. Even for two particles, the numerical scheme thereby gets into difficulties when correlation effects lead to a strong modification of the HF Green’s function which serves as reference state in the iterative procedure—recall the role of $\mathbf{g}^0(\tau)$ in Sect. 4.3. As this is generally the case for an increased λ , results for stronger coupled fermions are not directly accessible. However, if the coupling is large enough, the fermions will be spatially well separated and the overlap of their respective wave functions becomes small. Consequently, also correlation effects should be reduced at sufficiently low temperatures, so that moreover convergence should be realizable.

The problem which remains is that the Hartree-Fock method according to the Roothaan-Hall equations (4.10) must give a reasonable mean-field result. In the regime of large coupling parameters, the low number of provided oscillator wave functions can make the algorithm unstable. Further, the quality of the result might be questionable due to the fact that these basis states become inappropriate when the parabolic potential is highly deformed by the mean-field corrections. However, in some cases correct convergence has been obtained by permitting a very large number of iterations—empirically several hundreds in contrast to the regime of low λ , where good convergence is typically obtained within 10 to 20 iterations.

For quasi zero temperature $\beta = 25$, Fig. 5.14 shows results for the particle density of three fermions in the parabolic confinement whereby the coupling parameters are in an intermediate

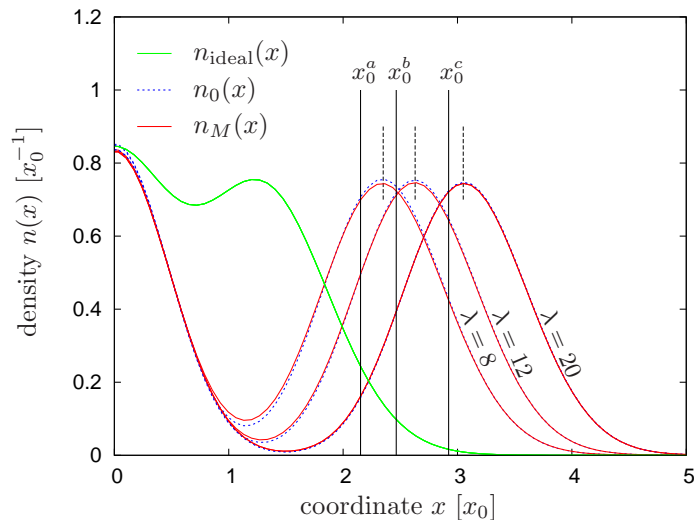


Figure 5.14: $N = 3$ strongly correlated fermions at quasi zero temperature $\beta = 25$. The coupling parameters are a: $\lambda = 8$, b: $\lambda = 12$ and c: $\lambda = 20$. The formation of a Wigner chain is observed for $\lambda > 20$ where the overlap between the Gaussian peaks vanishes. The solid vertical lines denote the corresponding classical equilibrium positions obtained by minimizing Eq. (5.13). In contrast, the green line shows the density profile of the noninteracting system. Notation as in Figs. 5.7 and 5.8.

range of $\lambda = 8, 12, 20$. For the case of $\lambda = 20$, one notices that the overlap of regions attributable to a single particle has almost disappeared giving rise to Wigner crystal behavior. In a one-dimensional situation, however, a crystal-like structure is not formed but a Wigner *chain* of localized fermions, where for $N = 3$ a single particle is sitting in the trap center and two adjacent particles are situated at a fixed distance characterized by the maxima of the Gaussian peaks. This distance should thereby relate to ground state results originating from a classical or semi-classical treatment [69, 70], where the N -particle problem of harmonically confined particles in d dimensions can (for $\lambda \rightarrow \infty$) be reduced to a superposition of $N \cdot d$ uncoupled harmonic oscillators $\phi_i(R_i)$ with transformed space coordinates, $x_i \rightarrow R_i$. More precisely, in the strong coupling limit, $\lambda \rightarrow \infty$, such distances should coincide with the classical equilibrium positions $\mathbf{x}_{0,\lambda}$ of the particles obtained by minimizing the total potential energy

$$V_\lambda(\mathbf{x}) = V_\lambda(x_1, \dots, x_N) = \sum_{i=1}^N \frac{1}{2} x_i^2 + \sum_{i < j} \frac{\lambda}{\sqrt{(x_i - x_j)^2 + a^2}}, \quad (5.13)$$

i.e. requiring $\nabla V_\lambda(\mathbf{x}_{0,\lambda}) \equiv 0$. The solid vertical lines shown in Fig. 5.14 indicate these equilibrium positions for the investigated values of the coupling parameter. In order to prove the correctness of the results one now can verify that:

- i. As λ increases, the maximum of the peak approaches the classical equilibrium position—due to an exchange induced repulsion the peak is generally situated at coordinates $x \geq x_{0,\lambda}$.
- ii. Since the overlap in the density vanishes, each separated Gaussian or Gaussian-like peak becomes normalized to one in agreement with an occupation by a single particle only.
- iii. Within the energy spectrum $\{\epsilon_k\}$ as obtained from the HF equations (4.10), the lowest energy level ϵ_0 , corresponding to the particle situated in the trap center, is followed by two almost identical energies $\epsilon_{1,2}$ (they slightly differ due to exchange) which describe the states of both adjacent fermions which become identical for $\lambda \rightarrow \infty$.
- iv. Moreover, the influence of correlation effects on the equilibrium density decreases for larger couplings λ and tends towards zero for vanishing overlap.

In conclusion, one can show that the correlated Matsubara Green's function is also accessible in a strongly correlated regime—at least for quasi zero temperature as demonstrated by Fig.

5.14. To what extent also quantum melting processes (when λ is decreased) or thermal melting processes of the Wigner chain (when the temperature is increased at fixed λ) can be observed stays unresolved. However, this goes far beyond the topic of the present work and is thus left for future investigations.

5.4. Comparison with PIMC simulations

Besides the quantum statistical description—which is used in the present work—an alternative way is to consider the many-particle system on microscopic grounds. In this context, there exist efficient quantum Monte Carlo (QMC) techniques that allow one to numerically simulate correlated quantum systems from *first principles*. Such simulations, as in particular the path integral Monte Carlo (PIMC) method, are thereby extremely successful describing the system's static properties in thermodynamic equilibrium and, furthermore, have wide ranges of applicability. For the main ideas of Monte Carlo algorithms and PIMC simulations it is referred to e.g. Ref. [13] (and references therein), which besides a discussion of the classical counterpart of PIMC also covers aspects on modeling the system evolution by quantum molecular dynamics (QMD).

The present section is now devoted to the comparison of the Green's function results concerning the system (5.1) with the corresponding results of path integral Monte Carlo simulations. The reference quantity is thereby the total energy E_{tot} of the interacting N -particle system which changes in dependence on particle number, coupling parameter and temperature.

As it has been implemented, the Matsubara Green's function is however based on a grand canonical ensemble averaging, while PIMC simulations typically include temperature effects on a canonical footing. Thus one must be aware of fundamental differences which originate from the use of unequal ensembles. This is in particular important when considering a finite mesoscopic system where in a grand canonical approach fluctuations—due low particle numbers—are in general large leading to different observables compared with the canonical ensemble. This is for example verified by considering an ideal system of N noninteracting fermions in a harmonic trap. The respective partition functions Z_N and the total energy are given by:

- **Canonical ensemble (CE):**

In terms of a recursion relationship, see e.g. Tran *et al.* [71], it is for fermions

$$Z_N^{\text{CE}}(\beta) = \frac{1}{N} \sum_{n=1}^N (-1)^{n+1} Z_1^{\text{CE}}(n\beta) Z_{N-n}^{\text{CE}}(\beta), \quad Z_0^{\text{CE}}(\beta) \equiv 1, \quad (5.14)$$

where for the one-dimensional harmonic oscillator one has

$$Z_1^{\text{CE}}(\beta) = \frac{\exp(-\beta/2)}{1 - \exp(-\beta)}, \quad (5.15)$$

with dimensionless inverse temperature β corresponding to units of $(\hbar\Omega)^{-1}$. The total energy then follows from

$$E_{\text{tot}}^{\text{CE}} = -\frac{\partial \ln Z_N^{\text{CE}}(\beta)}{\partial \beta}. \quad (5.16)$$

- **Grand canonical ensemble (GCE):**

The grand canonical partition function is given by

$$Z_N^{\text{GCE}}(\beta, \mu) = \prod_{n=0}^{\infty} [1 + \exp(-\beta(\epsilon_n - \mu))], \quad \epsilon_n = n + \frac{1}{2}, \quad (5.17)$$

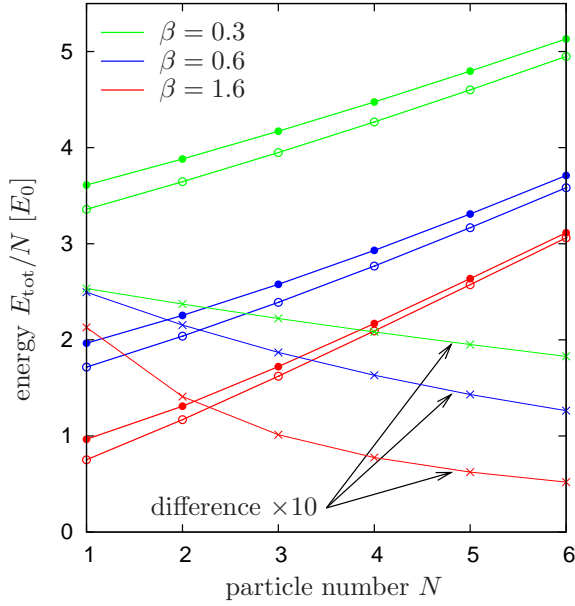


Figure 5.15: Total energy per particle for different numbers of ideal trapped fermions in the canonical \circ and the grand canonical \bullet ensemble for three different temperatures. The crosses \times indicate the difference $E_{\text{tot}}^{\text{CE}} - E_{\text{tot}}^{\text{GCE}}$ stretched by a factor of $\times 10$. In the limit of macroscopic particle numbers ($N \rightarrow 10^{23}$) both ensembles will yield the same energies due to negligible amount of fluctuations.

where the chemical potential μ is obtained from the particle number constraint

$$N = \sum_{n=0}^{\infty} [\exp(\beta(\epsilon_n - \mu)) + 1]^{-1}. \quad (5.18)$$

The expression for the total energy then reads

$$E_{\text{tot}}^{\text{GCE}} = -\frac{\partial \ln Z_N^{\text{GCE}}(\beta, \mu)}{\partial \beta} + N\mu. \quad (5.19)$$

Using Eqs. (5.14) to (5.19), the total energies of the ideal system can easily be calculated in both ensembles, and Fig. 5.15 shows results for the particle number N ranging from one to six trapped fermions with the total energy measured in units of $E_0 = \hbar\Omega$ per particle. At finite temperatures $\beta < 2$, the energies differ by 5 – 30% of the oscillator energy level spacing $\Delta\epsilon = \hbar\Omega$ where in general the grand canonical result yields a larger energy—the larger the temperatures for a fixed particle number the higher is thereby the discrepancy $E_{\text{tot}}^{\text{CE}} - E_{\text{tot}}^{\text{GCE}}$. In the limit $k_B T \rightarrow 0$ as well as for a macroscopic number of particles, both ensembles should however yield the same results—the corresponding tendencies can be extracted from the figure. In the mesoscopic range and at moderate temperatures the differences are however not negligible and must be taken into account when comparing the Green’s function result with path integral Monte Carlo.

Besides the different statistical ensembles which are in use, one in addition has to note the following. Since in both methods different interaction potentials are being applied, i.e.

$$w^{\text{PIMC}}(x_1, x_2) = \frac{\lambda}{|x_1 - x_2|}, \quad w^{\text{MGF}}(x_1, x_2) = \frac{\lambda}{\sqrt{(x_1 - x_2)^2 + a^2}}, \quad (5.20)$$

one has to be sure of implications onto the total energy of the system. In the limit $a \rightarrow 0$, both types of interactions are identical but for finite parameters a the second potential in (5.20), $w^{\text{MGF}}(x_1, x_2)$, behaves not Coulomb-like when $(x_1 - x_2) \rightarrow 0$, see also Appendix A.2.2. To this

$N = 3:$				
β	λ	$E_{\text{tot}}^{\text{MGF}}$	$E_{\text{tot}}^{\text{MGF}}/N$	$E_{\text{tot}}^{\text{PIMC}}/N$
2	0.0	4.948529 (4.94853)	1.64951 (1.64951)	[1.5671]
2	0.3	5.612797	1.87093	1.8287 ± 0.021
2	0.6	6.246417	2.08214	1.9749 ± 0.011
2	0.9	6.854232	2.28474	2.1908 ± 0.004
2	1.2	7.438393	2.47946	2.3878 ± 0.004
2	1.5	7.9979	2.66597	2.5769 ± 0.004
0.5	0.0	8.586392 (8.66328)	2.86213 (2.88776)	[2.68903]
0.5	0.5	9.793043	3.26435	3.0582 ± 0.012
0.5	1.0	10.881657	3.62722	3.4067 ± 0.010
0.5	1.5	11.882	3.96067	3.7194 ± 0.011
1/3	0.0	10.935541 (11.5393)	3.64518 (3.84643)	[3.62798]
1/3	0.5	12.192298	4.06410	3.9729 ± 0.026
1/3	0.75	12.772601	4.25753	4.1679 ± 0.025
1/3	1.0	13.322936	4.44098	4.3214 ± 0.019
1/3	1.5	14.343853	4.78128	4.6525 ± 0.011
1/3	2.0	—	—	4.9622 ± 0.020
$N = 4:$				
β	λ	$E_{\text{tot}}^{\text{MGF}}$	$E_{\text{tot}}^{\text{MGF}}/N$	$E_{\text{tot}}^{\text{PIMC}}/N$
2	0.0	8.451725 (8.45173)	2.11293 (2.11293)	[2.05066]
2	0.5	10.551249	2.63781	2.8 ± 0.12
2	1.0	12.505237	3.12631	3.0375 ± 0.008
2	1.5	14.339205	3.58480	3.5077 ± 0.007
2	2.0	—	—	3.9385 ± 0.005
0.5	0.0	12.770624 (12.9029)	3.19266 (3.22573)	[3.04829]
0.5	0.5	14.979172	3.74479	3.5763 ± 0.033
0.5	1.0	16.998877	4.24972	4.0884 ± 0.021
0.5	1.5	18.863749	4.71594	4.5442 ± 0.028
0.5	2.0	—	—	4.9794 ± 0.017
$N = 6:$				
β	λ	$E_{\text{tot}}^{\text{MGF}}$	$E_{\text{tot}}^{\text{MGF}}/N$	$E_{\text{tot}}^{\text{PIMC}}/N$
4/3	0.0	18.965186 (18.9653)	3.16086 (3.16088)	[3.09851]
4/3	0.5	23.927851	3.98798	—
4/3	1.0	28.566666	4.76111	4.7866 ± 0.022
4/3	1.5	32.939067	5.48984	5.4132 ± 0.022
4/3	2.0	—	—	6.073 ± 0.027
0.5	0.0	23.472723 (23.811)	3.91212 (3.9685)	[3.82578]
0.5	0.5	28.526543	4.75442	4.7258 ± 0.093
0.5	1.0	33.182059	5.53034	5.4112 ± 0.004
0.5	1.5	37.529182	6.25486	6.1892 ± 0.029
0.5	2.0	—	—	6.8795 ± 0.017

Table 5.5: Comparison of total energies $E_{\text{tot}}(N, \beta, \lambda)$ as obtained from the Matsubara Green's function (MGF) with path integral Monte Carlo (PIMC) simulations. Numbers in brackets correspond to analytical results for $\lambda \equiv 0$ as computed from Eqs. (5.16) and (5.19): [...] = canonical ensemble, (...) = grand canonical ensemble. Energies are displayed in units of $E_0 = \hbar\Omega$ and β is given in units of E_0^{-1} .

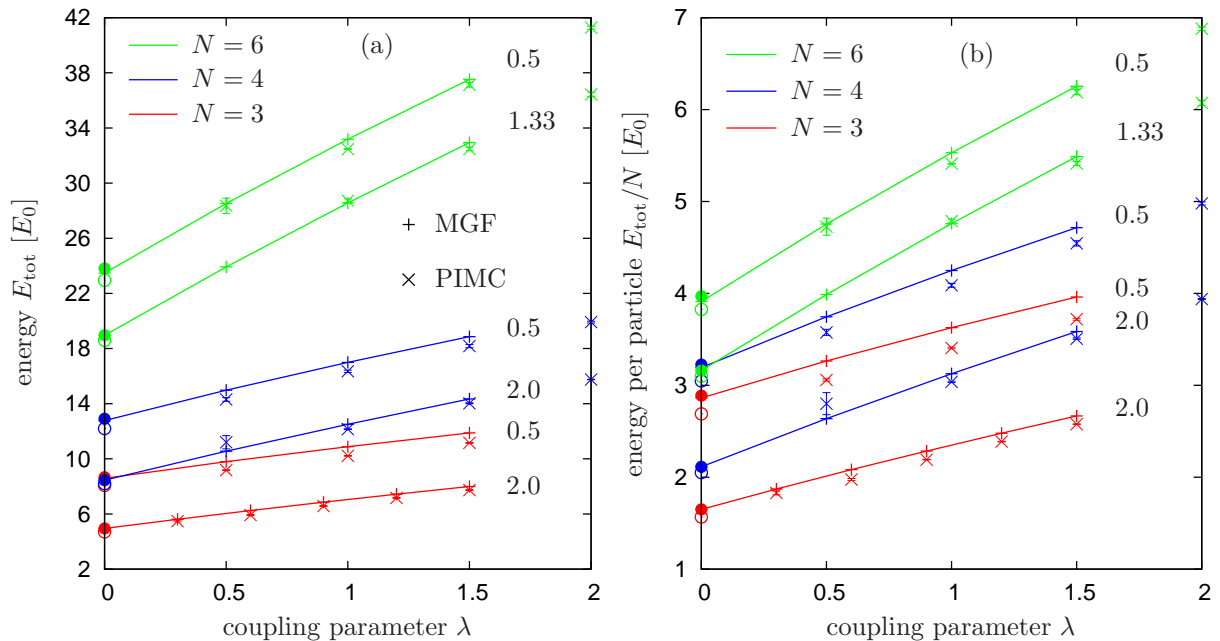


Figure 5.16: Comparison of energies with path integral Monte Carlo simulations for different particle numbers. (a) Total energy $E_{\text{tot}}(N, \beta, \lambda)$ and (b) total energy per particle $E_{\text{tot}}(N, \beta, \lambda)/N$. $+$: energies obtained from the Matsubara Green’s function, \times : energies from PIMC including error bars. The values within the figures indicate the inverse temperature β . For $\lambda \equiv 0$, \circ denotes the analytical result for the canonical ensemble while \bullet is connected with the grand canonical ensemble. For collection of the numerical data see Table 5.5. Lines connect the Green’s function results and are a guide to the energy.

end, the parameter a must be chosen thoroughly and in particular sufficiently small so that the total energy as obtained from the Matsubara Green’s function remains almost constant by variation of a , i.e. $\partial E_{\text{tot}}^{\text{MGF}}/\partial a \approx 0$. It turns out that a value of $a \lesssim 0.1$ is thereby adequate when a weakly interacting system—according to a low value of λ —is considered. This is furthermore consistent with the perturbation theory results discussed in Sect. 5.1 where from Fig. 5.2 one has estimated hardly any discrepancies between the pure and the approximate Coulomb potential when a decreases below a tenth of the characteristic confinement length x_0 .

Now, consider Fig. 5.16 which shows the comparison of the numerical results for the Matsubara equilibrium state and the path integral Monte Carlo (PIMC) simulation¹. The left hand panel thereby shows the total energy in dependence on the coupling parameter for different particle numbers and different temperatures—the right hand panel displays the respective total energy per particle. Throughout, the small parameter is set fixed to be $a = 0.1$. For the collection of the numerical data it is referred to Table 5.5.

Overall, the comparison demonstrates a relatively good agreement of the results originating from both methods. The behavior of the total energy in dependence on the coupling parameter is practically identical, whereby for all configurations (N, β) the slope $\partial E_{\text{tot}}/\partial \lambda$ slightly changes to lower values when λ is increased, i.e. the total energy is not directly proportional to the coupling parameter. However, the influence of the different statistics being used evident and especially apparent when considering the energy per particle $E_{\text{tot}}(\lambda)/N$. Here, one clearly sees—besides a qualitatively equal behavior—that the PIMC result is generally smaller than the energy obtained from the Green’s function, and for larger N at fixed temperatures both results converge. Further, for $\lambda \rightarrow 0$, both results converge to their respective ideal results (indicated by the filled and

¹The PIMC data have been provided by A. Filinov (Research group of M. Bonitz, Institut für Theoretische Physik und Astrophysik, University of Kiel).

unfilled circles) as they are discussed in Fig. 5.15—for $\lambda \equiv 0$ however, here no Monte Carlo results are available.

In conclusion one might think of adding a temperature and particle number depending offset to the path integral Monte Carlo result leading to curves that practically coincide. This is in particular motivated by the fact that it is generally possible to convert between the different statistical ensembles—at least most easily for the ideal case of noninteracting particles.

For completeness, one should furthermore notice that the Green's function results for $\beta = 0.5$ are linked with some errors (compare with the exact values in Table 5.5) that originate from the limited number of basis functions which are manageable by the numerical procedure. However, these errors do not exceed an amount of $\Delta E_{\text{tot}} \approx 0.5 \hbar \Omega$ for the total energy.

6. Nonequilibrium behavior

As the previous chapter has examined the thermodynamic equilibrium state of fermionic ensembles trapped in a parabolic potential, the present chapter is now devoted to the analysis of time-dependent processes in nonequilibrium. Starting from the precomputed (un)correlated equilibrium Green's function $\mathbf{g}^M(\tau)$, the system governing the Hamiltonian (5.1) is now propagated in real-time according to the Keldysh/Kadanoff-Baym equations presented in numerical detail at the end of Chap. 4 (Sect. 4.5).

Without any disturbing time-dependent potential $V_{\text{ext}}(x_i, t)$, the two-time propagation of the Green's function thereby allows for a systematical test for the equilibrium state being stationary. Besides the correlation energy which has already been focused on in Sect. 4.5.3, the total energy and the spatial density are important quantities for examination. This is demonstrated in the first part of this chapter together with an overview of the Green's functions in nonequilibrium and a brief discussion on the complexity of the numerical computations.

Thereafter, the system behavior is examined under direct influence of a time-dependent and temporally bounded dipole field. An example is a *laser pulse* the occurrence of which will drive the interacting quantum system similar to a forced harmonic oscillator with linear coupling. Advantageously, the Green's function technique thereby permits an analysis beyond the linear response regime including excitations of arbitrary form. Numerically, the strength of the laser excitation is however limited by the finite number of Hartree-Fock orbitals (HFO) included in the computations—see Sect. 6.2. Nevertheless, there are different situations analyzable: Varying the field parameters, one observes either (near) resonant excitations or an off-resonant behavior where the thermodynamic initial state is recovered after the pulse has passed the trapped Fermi liquid. Exactly in this context, one furthermore recovers the importance of the so-called *Kohn theorem* [46] in combination with conserving approximations. As the Kohn theorem states that the center of mass oscillation (COM, Kohn or sloshing mode) of a harmonically confined many-body system is independent of the pair-interaction, it is not obvious that this also holds for an approximate treatment of the interaction. However, it turns out that the Kadanoff-Baym criteria (A) and (B) as given in Sect. 3.1 are sufficient to preserve the Kohn mode [72]. A corresponding numerical analysis is given in Sect. 6.3.

6.1. The nonequilibrium Green's functions $\mathbf{g}^\star(t, t')$, $\star \equiv \{\gtrless, \rfloor/\rfloor\}$

When the correlated thermodynamic equilibrium state—characterized through the Matsubara Green's function $\mathbf{g}^M(\tau)$ in the direct time space—is propagated in real-time according to the set of Keldysh/Kadanoff-Baym equations (4.47-4.50) in Sect. 4.5, there additionally appear the greater and lesser correlation functions $\mathbf{g}^{\gtrless}(t_1, t_2)$ and the mixed functions $\mathbf{g}^{\rfloor}(t_1, \tau_2)$ and $\mathbf{g}^{\rfloor}(\tau_1, t_2)$ obeying the initial conditions given in Eqs. (4.45) and (4.46). While the former greater and lesser functions carry the statistical and dynamical information and furthermore enter the dynamical memory kernels—recall the real-time integrations contained in the collision terms (4.51) and (4.52) at the beginning of Sect. 4.5—both latter functions account for the correct evolution of the initial correlations. Thus, the mixed functions are only necessary if the system description includes correlation effects. Otherwise, as e.g. in Hartree-Fock approximation, it is fully sufficient to prepare the correlation functions \mathbf{g}^{\gtrless} with the initial conditions mentioned above and only to

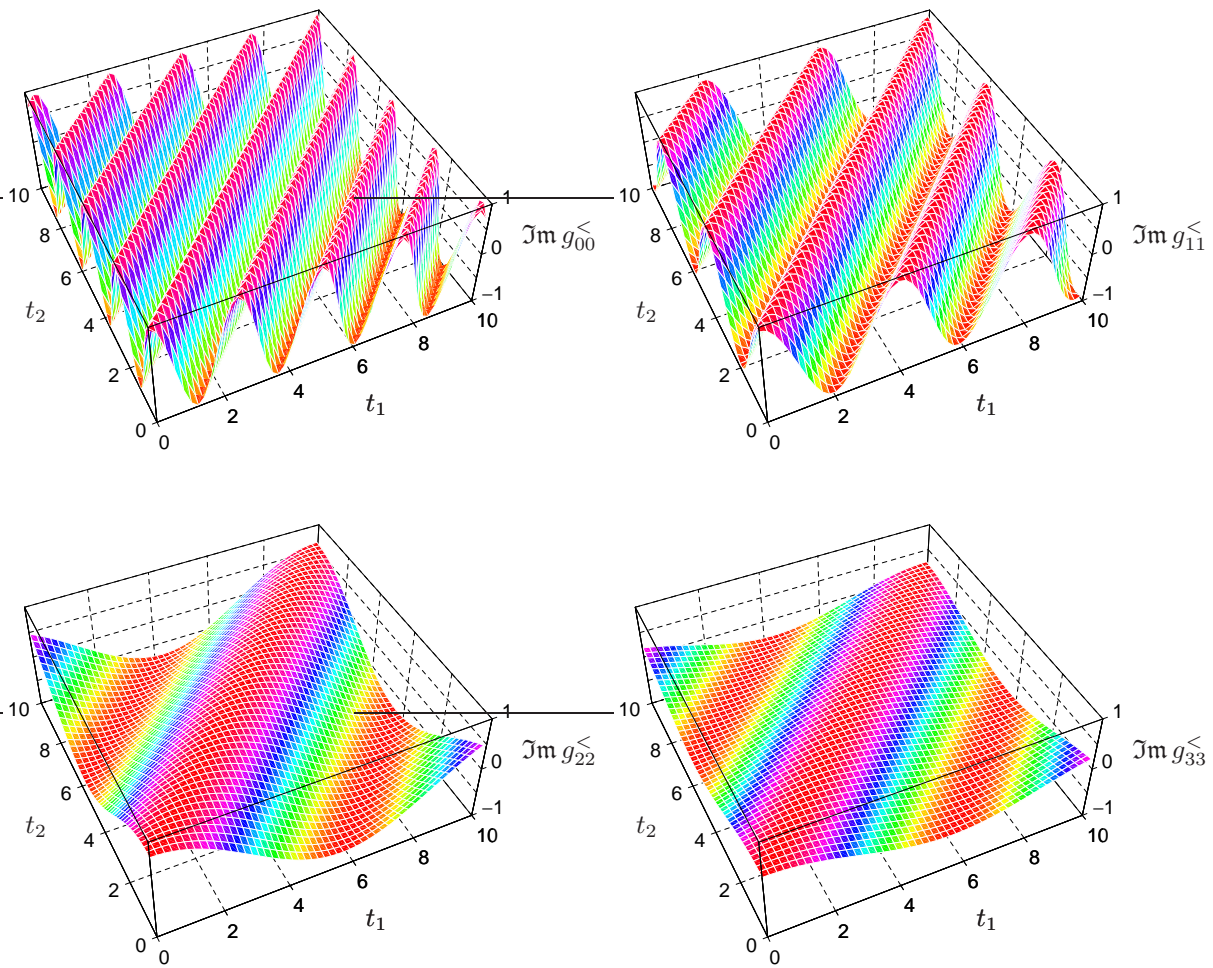


Figure 6.1: Time-evolution of the lesser correlation function $\mathbf{g}^<(t_1, t_2)$ for $N = 3$ trapped fermions in Hartree-Fock approximation. Displayed is the imaginary part of the diagonal elements $g_{ii}^<(t_1, t_2)$ with $i \leq 3$. $t_{1,2}$ are measured in units of Ω^{-1} . System parameters: The inverse temperature is $\beta = 1.5$ and the coupling parameter reads $\lambda = 0.5$. Here, and in the remainder of this chapter, $a = 0.1$ —cf. Eq. (5.1).

solve their respective equations of motion, Eqs. (4.47) and (4.48).

However, if correlations are present, the information provided by $\mathbf{g}^{1/\Gamma}$ is in general required at all times $t_{1,2} \geq t_0$. This has been demonstrated in Sect. 4.5.3 in combination with the discussion of the correlation energy.

Due to the huge amount of information contained in the nonequilibrium Green's function matrices, it is useful—for illustrative purposes—to focus on the lesser correlation function $\mathbf{g}^<(t_1, t_2)$ and its temporal behavior in the two-time plane. Further, most closely related to the physical properties of the many-body system is the imaginary part of the lesser correlation function, since at equal times $t_1 = t_2$ one arrives at the density matrix (remember Eq. (4.69)). Therefore, the quantity $\Im \mathbf{g}^<(t_1, t_2)$ shall be investigated in the following. For a more comprehensive demonstration of the correlation functions it is referred to e.g. Ref. [13].

Figures 6.1 and 6.2 show the diagonal elements $\Im g_{kk}^<(t_1, t_2)$ for the time-propagation of $N = 3$ trapped fermions in Hartree-Fock and in second Born approximation, respectively. Initially, at time $t_0 = 0$, the system is in thermodynamic equilibrium ($\beta = 1.5$), and for $t_{1,2} > t_0$ there is no external field acting upon the particle ensemble. Comparing the contents of the different plots,

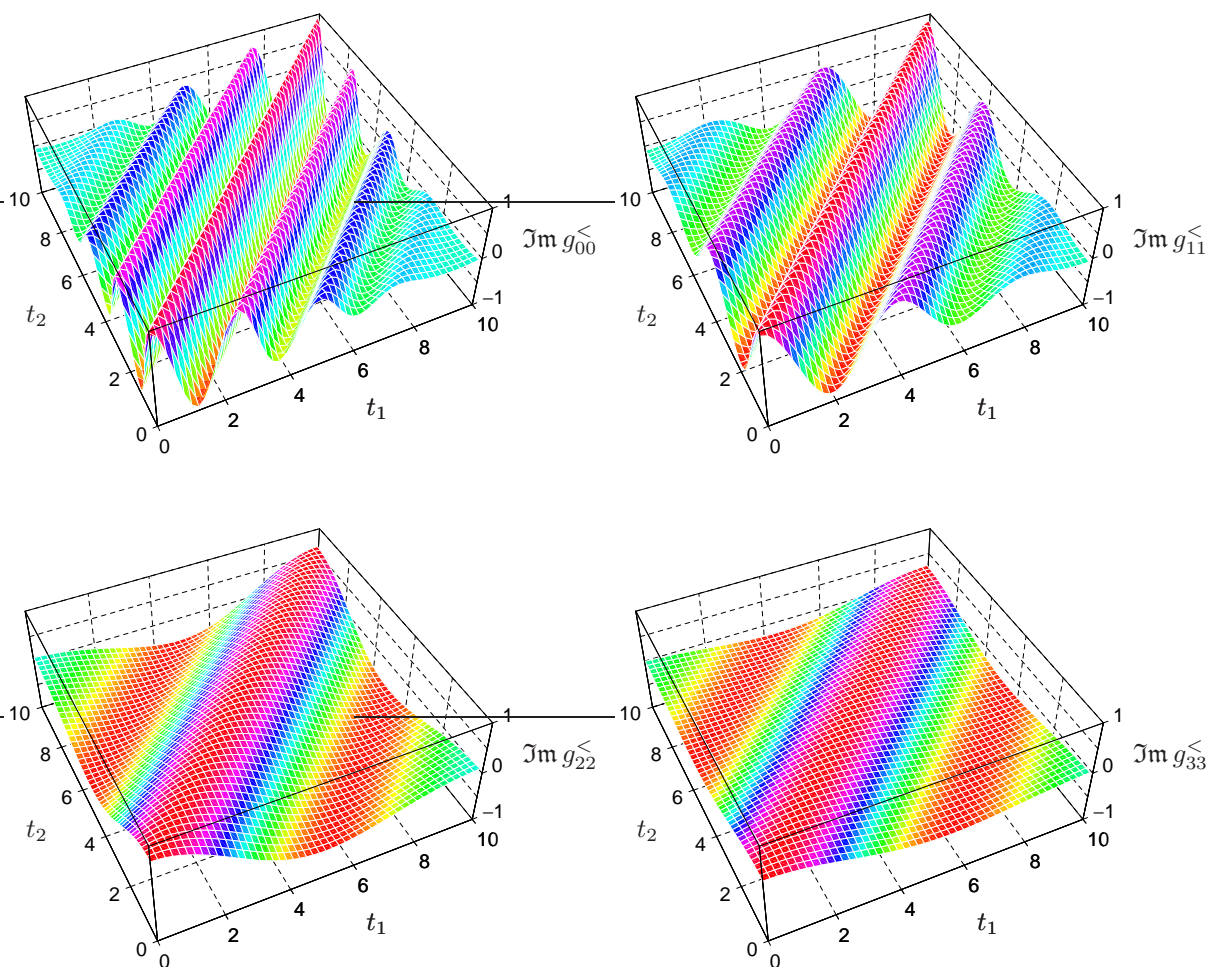


Figure 6.2: Time-evolution of the lesser correlation function $\mathbf{g}^<(t_1, t_2)$ for $N = 3$ trapped fermions in second Born approximation, i.e. including correlations. As in Fig. 6.1, the particular figures show the imaginary part of the diagonal elements $g_{ii}^<(t_1, t_2)$ with $i \leq 3$. $t_{1,2}$ are measured in units of Ω^{-1} . System parameters: $\beta = 1.5$, $\lambda = 0.5$.

one notices:

- i. On the time diagonal, all matrix elements are constant yielding the occupation probabilities of the respective HF orbitals, i.e.

$$n_k(t) = \rho_{kk}(t) = \pm i g_{kk}^<(t, t), \quad (6.1)$$

where ρ denotes the density matrix which, in this case, does not change in time. The set of values $\{n_k(t)\}$ further gives the time-evolution of the distribution function $f(\epsilon_k - \mu, t)$.

- ii. In Hartree-Fock approximation (Fig. 6.1), the correlation functions $g_{kk}^<(t_1, t_2)$ perform each an undamped oscillation perpendicular to the time diagonal. The frequencies of these oscillations thereby correspond directly to the HF renormalized one-particle energies ϵ_k of the harmonic confinement. As one conveniently subtracts the chemical potential μ in the single-particle energy $h^0(x, t)$ —look back on Eq. (4.16) in Sect. 4.1.2—the oscillation frequency decreases when considering higher HF levels k . For states which are located energetically above the chemical potential this trend is reversed.

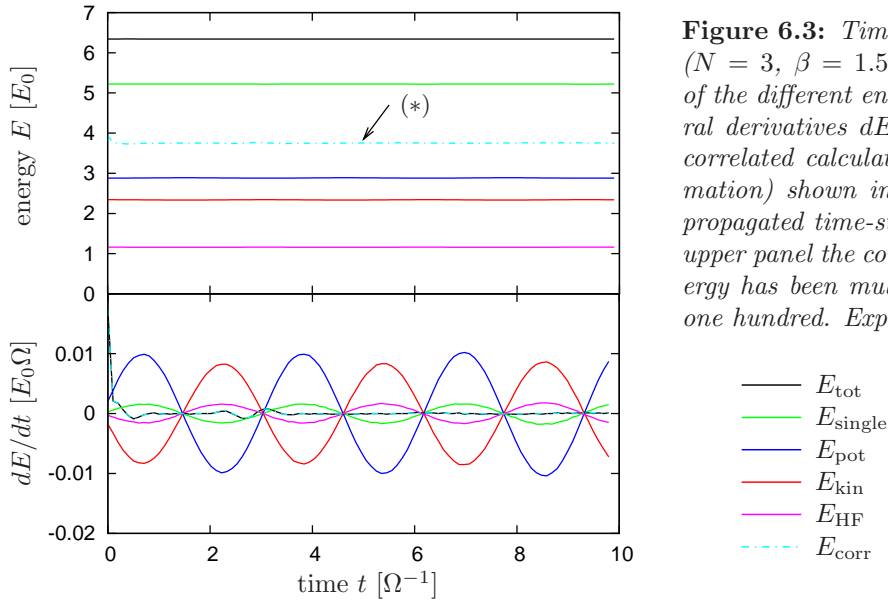


Figure 6.3: Time-propagation in equilibrium ($N = 3$, $\beta = 1.5$, $\lambda = 0.5$): Time-evolution of the different energies $E(t)$ and their temporal derivatives $dE(t)/dt$ corresponding to the correlated calculations (second Born approximation) shown in Fig. 6.2. The number of propagated time-steps is $n_\Delta = 100$. (*) In the upper panel the correlation part of the total energy has been multiplied by a factor of minus one hundred. Explanation of the curves:

— E_{tot}
— E_{single}
— E_{pot}
— E_{kin}
— E_{HF}
- - - E_{corr}

Furthermore, the oscillatory behavior of $g_{kk}^<(t_1, t_2)$ in second Born approximation (Fig. 6.2) is different. Due to included particle collisions, the one-particle energy spectrum is no longer composed of sharp peaks but exhibits an *energy broadening* of the Hartree-Fock states corresponding to a finite lifetime of these quasi-particle states. This generally leads to damping of the oscillations of $g_{kk}^<(t_1, t_2)$.

- iii. Apart from the diagonal elements of the lesser correlation function, the off-diagonal elements $\mathbf{g}_{kl}^<(t_1, t_2)$ with $k \neq l$ (which are not shown in the figures) are physically connected with the transition probabilities between the Hartree-Fock orbitals k and l .

Moreover, as mentioned in the introduction of this chapter, the numerical results for the Green's functions must come through various tests of accuracy. Besides the stationarity of the spatial density profile analyzable according to Eq. (4.85), the energy conservation serves as an essential test for the correctness of the numerical time-stepping procedure, and allows to decide—in particular by looking at the correlation energy—if the two-time plane is adequately discretized via n_Δ . The different energies are thereby computed according to the formulas given in Sect. 4.5.3. Besides the single-particle energy E_{single} , consisting of the kinetic and potential energy, there occurs the mean-field contribution (the Hartree-Fock energy E_{HF}), and if the computations are carried out in second Born approximation one has additionally the correlation energy E_{corr} . All together then add up to the total energy of the many-body system.

Fig. 6.3 displays the time-dependence of the different energies for the evolution of the equilibrium state analyzed in terms of the correlation function in Fig. 6.2, i.e. in full second Born approximation. As expected, all energy contributions are essentially constant. However, the derivatives $dE(t)/dt$ deviate from zero because of numerical reasons. Particularly, the derivatives of the kinetic (red curve) and the potential energy (blue curve) oscillate in time whereby the respective frequency coincides with the double trap frequency. This reveals a negligible oscillation of the system within the trap, as the behavior of $dE_{\text{tot}}(t)/dt$ confirms that the overall energy is well conserved. Further, the slight decrease of the correlation energy at the beginning of the time-propagation is related to small errors in the precomputed equilibrium state. Additionally, notice that for finite couplings $\lambda > 0$ it is $E_{\text{kin}} \neq E_{\text{pot}}$, i.e. the virial theorem does not hold due to the presence of the HF mean-field that spatially modifies the parabolic potential.

6.1.1. Numerical costs

While the numerical procedure leading to the equilibrium Matsubara Green's function can be formulated as a self-consistency problem which offers an iterative solution scheme (this is described at large in Sect. 4.3), the situation is completely different for the time-propagation of the Green's function matrices. Here, one directly has to integrate the equations of motions—the real-time KKBE—and, consequently, the demand for computing time is different.

First of all, the required CPU time generally scales as n_Δ^2 , where n_Δ denotes the total number of time steps to be propagated. This behavior is related to the integrations entering the collision terms which have to be performed on the expanding square $\mathcal{S} = [t_0, t_1] \times [t_0, t_2]$, see Fig. 4.7 in Sect. 4.5. As both times t_1 and t_2 increase, a larger number of grid points lead to more time-consuming integrations. Further, the number of integrations and most other operations (e.g. the computation of the self-energy—see below) is directly proportional to the number of matrix elements involved in the computations, i.e. in addition one attains a n_b^2 -dependence in the required computing time. The number of basis functions n_b , thus, has large influence and quickly slows down the algorithm speed. The time-stepping itself, i.e. the part of the algorithm which actually performs the time-step, $\mathbf{g}(T) \rightarrow \mathbf{g}(T + \Delta)$, according to Eqs. (4.56) to (4.60) is thereby relatively simple and allows for a fast processing.

Moreover, the evaluation of the dynamic self-energy $\Sigma^{\text{corr}}(t_1, t_2)$ as functional of the actual Green's function $\mathbf{g}(t_1, t_2)$ requires most CPU time, since each matrix element $\Sigma_{ij}^{\text{corr}}(t_1, t_2)$ is computed from a six-fold sum over the product of two tensors $w_{ij,kl}$ and three Green's functions matrix elements $g_{ij}(t_1, t_2)$ —remember Eq. (3.58) of Sect. 3.3.1. However, some minor improvements simplify the self-energy sub-routines within the code: Rearranging the nested sums in a clever way allows to estimate the contributions arising from inner summations. Consequently, if these contributions are small one may skip the respective summations.

In total, typical computing times for correlated calculations which lead to an adequate system description easily exceed several hours on a single processor. The implementation of self-energy approximations beyond diagrammatic second order are therefore hardly manageable or lead at least to severe numerical efforts.

In Hartree-Fock approximation, the time-evolution of the initial state is of course much simpler, since the self-energy $\Sigma(t_1, t_2) = \Sigma^{\text{HF}} \delta_C(t_1 - t_2)$ is local in time and, consequently, the collision integrals do not have to be computed as they are zero. Numerical results are therefore rapidly accessed.

6.2. Nonequilibrium situations

While the previous section has demonstrated the time-propagation in equilibrium, this section will now focus on nonequilibrium situations where the "mesoscopic Fermi liquid" is affected by an external perturbation. Going beyond the linear response regime where the quantum system is simply forced by a strongly localized *kick* of the form $V_0 \delta(t)$, one may choose to study the particle dynamics under the influence of an electric dipole field which enters the second-quantized Hamiltonian (see e.g. Eq. (4.1)) as the external potential

$$V_{\text{ext}}(x, t) = \mathcal{E}(t) d = q_0 \mathcal{E}(t) x, \quad (6.2)$$

and, therefore, allows for an arbitrary time-dependence in the electric field strength $\mathcal{E}(t)$. The quantity $d = q_0 x$ in Eq. (6.2) indicates the dipole moment with q_0 being the particle charge. Translated into the HF orbital (HFO) representation the single-particle Hamiltonian $\mathbf{h}^0(t)$ then includes the term $\mathbf{v}_{\text{ext}}(t) = \mathcal{E}(t) \mathbf{d}$, where \mathbf{d} is the dipole matrix as defined in Sect. 4.5.3.

However, due to the bounded time interval manageable by the numerical propagation of the initial state, one is in the actual calculation restricted to a temporally limited area concerning

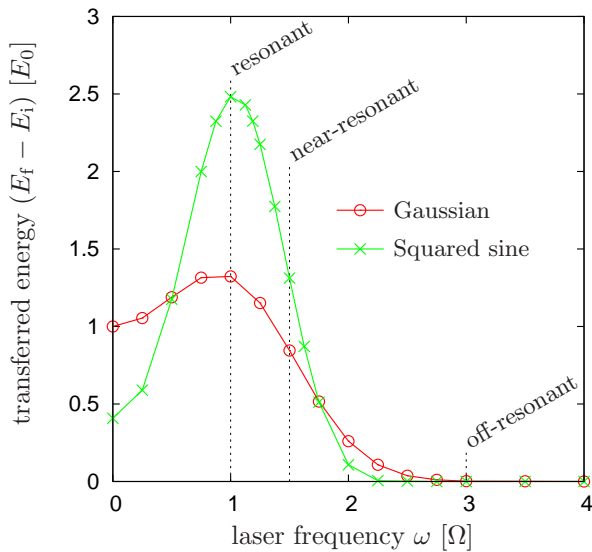


Figure 6.4: Frequency-dependence of the transferred energy for a Gaussian and a squared sine laser pulse acting upon $N = 4$ trapped fermions. Both pulses have identical amplitudes \mathcal{E}_0 and are approximately of the same temporal width. System parameters: The coupling parameter reads $\lambda = 1.5$ and the inverse temperature is $\beta = 25$.

the time-dependent electric field. Thus, it is a good idea to look at pulsed fields or, so to say, *laser pulses* which, besides by an amplitude \mathcal{E}_0 and a modulation frequency ω , are characterized by an envelope function $F(t)$, i.e. the electric field takes the form $\mathcal{E}(t) = \mathcal{E}_0 F(t) \cos(\omega t)$. For the special case of $F(t) = \delta(t)$, one then recovers excitations in linear response.

Numerically implemented are so far two different pulse shapes. The first and most common one, which is widely in use in laser experiments and in the theoretical description of short-time laser physics [73], has a Gaussian envelope,

$$\mathcal{E}(t) = e^{-\frac{(t-t_0)^2}{2\Delta t^2}} \cos(\omega(t-t_0) + \delta), \quad (6.3)$$

where t_0 localizes the pulse in time and Δt characterizes its temporal width. Further, one might add a parameter δ in the cosine term assigning a particular phase to the field modulation. Besides (6.3), another conventional pulse that has been included in the code shows a squared sine envelope, and further permits an analytical rewriting in terms of three cosine contributions—for definition and an overview to even more sophisticated pulses see Appendix C.

Applying the dipole field (6.2) within the KKBE, the interacting many-body system finally evolves—according to the particular self-energy approximation with or without correlations—under the influence of the so-called renormalized *Rabi energy* $\Xi(t) = \mathcal{E}(t) \mathbf{d} + \Sigma^{\text{HF}}(t)$ [12], which occurs as the sum of the external and the mean-field energy and is local in time. The field $\Xi(t)$ then in general will change the system’s total energy as it drives transitions between the different Hartree-Fock orbitals. However, due to the special case of harmonic confinement, only *interband* transitions ($k \leftrightarrow l$) with $k \neq l$ can occur, i.e. any *intra-band* accelerations are interdicted by the structure of the dipole matrix which also in its HF representation has vanishing diagonal elements $d_{kk}^{\text{HFO}} \equiv 0$ for all levels k —compare with Appendix A.1. Moreover, notice that the constraint $l = k \pm 1$ is valid for the ideal system but generally does not hold in the HFO representation.

Hartree-Fock calculations for $N = 4$ fermions, Fig. 6.4, show the energy transfer given as the difference between the final total energy, E_f , and the total energy E_i which the system had initially, before the dipole excitation. If one varies the laser frequency, one can distinguish three characteristic situations for the excitation kinetics:

- **Resonant.** When the laser frequency ω coincides with the trap frequency Ω , the time-dependent Rabi energy $\Xi(t)$ is most strongly coupled to the natural motion of the N -particle system in the trap and, consequently, the largest amount of energy is transferred.

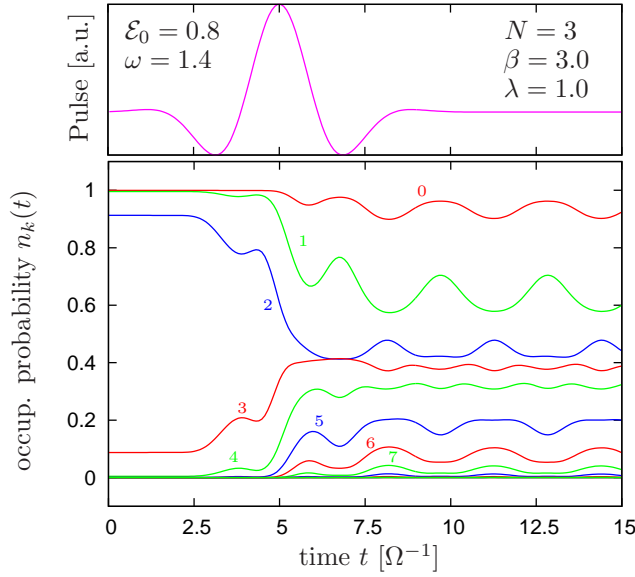


Figure 6.5: Time-dependent occupation probabilities $n_k(t)$ for $N = 3$ interacting fermions in the trap—HF calculation. The temperature, the coupling and field parameter are as indicated within the figure. The Gaussian pulse shown qualitatively in the upper panel is centered at $t_0 = 5$ with a duration of $\Delta t^2 = 1.5$. The amplitude \mathcal{E}_0 is measured in units of $\frac{\hbar\Omega}{q_0 x_0}$ and the laser frequency is given in multiples of Ω . The colored numbers in the lower panel indicate the corresponding HF orbital index k .

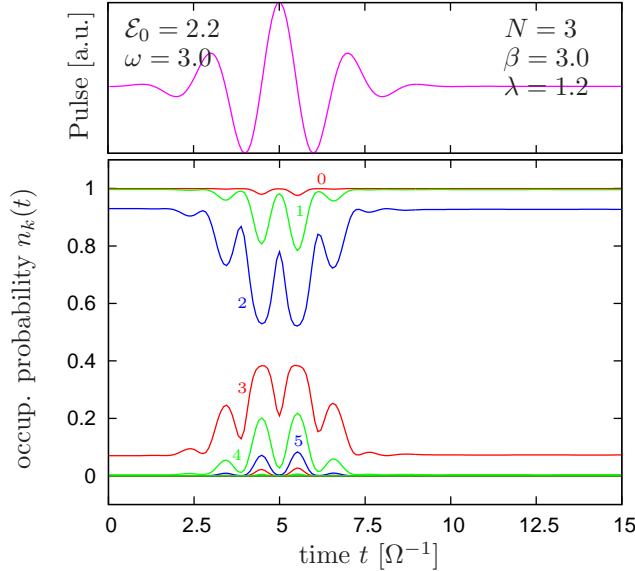


Figure 6.6: Same as in Fig. 6.5 above, but for an off-resonant situation with an increased laser frequency ω and a much larger field amplitude \mathcal{E}_0 . Notice that, further, the coupling parameter has changed leading to a slightly different initial distribution $\{n_k(0)\}$.

- **Near-resonant.** If both frequencies are put (slightly) out of tune, the coupling of the dipole field to the many-body system decreases. However, due to the spectral width of the laser pulse, there is still field energy absorbed from the particle ensemble.
- **Off-resonant.** For $\omega \gg \Omega$, there exists only a minimal coupling where practically no net energy transfer occurs—compare also with Fig. 6.6 showing the time-dependent occupation probabilities of the Hartree-Fock orbitals.

Additionally, one can extract from Fig. 6.4, that the system response may differ between laser pulses of identical amplitude \mathcal{E}_0 and equal temporal duration Δt . This is explained by different spectral widths $\Delta\omega$, which independently of amplitude and duration characterize any pulsed laser field—see also Appendix C.

Moreover, the excitation kinetics can be well understood from the HFO occupation probabilities $n_k(t)$ accessible via Eq. (6.1). For two different dipole excitations concerning an ensemble of three interacting fermions described at mean-field level, these are shown in Fig. 6.5 and Fig. 6.6,

respectively. Similar to solutions of semiconductor Keldysh/Kadanoff-Baym equations (see e.g. Kwong *et al.* [43] or textbooks like [40]), where one observes transitions between the valance and the conduction band, one here can directly extract the multilevel dynamics. Asbeforementioned, this implies the restriction to the interband transitions. In Fig. 6.5, the laser frequency is near the resonance. As a consequence, the laser field drives collective excitations of fermions into energetically higher HF levels. The transitions between the levels occur thereby instantaneously, and of course will change the total energy of the confined system. Further, temporally after the pulse, the appearing oscillations in $n_k(t)$ indicate that the system is no longer in an equilibrium state but that there exist time-dependent superpositions of HF levels. Fig. 6.6 covers the case of off-resonant laser excitation, where the modulation frequency is by a factor of three larger than the trap frequency. Nevertheless, the Gaussian-shaped pulse forces transitions between the various HF orbitals and, intermediately, leads to intensified occupations of higher lying states. After the laser pulse has passed, the system is however exactly reestablished in its initial state, i.e. the final state populations equal $n_k(t = 0)$. In terms of the density response one can state that the dipole field induces a vibration of the system initially at rest which is finally completely damped out.

While the occupation numbers $n_k(t)$ follow from the information of $\mathbf{g}(t_1, t_2)$ on the time diagonal only, it is also a good idea to study the Green's function in the whole two-time domain. Resulting from computations in full second Born approximation, Fig. 6.7 displays the function $\mathbf{g}^<(t_1, t_2)$ under the influence of a laser pulse which is centered at the time point $t_{1,2} = 5$. The system and field parameters are thereby chosen according to Fig. 6.4, i.e. in particular it is $\beta = 3.0$ and $\lambda = 1.0$. As discussed in Sect. 6.1, the off-diagonal oscillations of the correlation function are damped due to particle collisions. However, these oscillations are now further altered by the interplay of the external dipole field and the time-dependent (HF) mean-field, i.e. by the Rabi energy $\Xi(t)$, and additionally by binary correlations. Along the diagonal one then recovers again the decrease ($i < 3$) and the build-up ($i \geq 3$) of the fermion population. For $i \geq 3$, where initially less occupied or empty orbitals become populated, $\mathbf{g}^<(t_1, t_2)$ starts meanwhile to oscillate corresponding to the construction of the correlated energy spectrum.

Furthermore, the corresponding spectral function $\mathbf{A}(t_1, t_2)$ is shown in Fig. 6.8. As one can see, the energy spectrum is clearly modified when the dipole field is switched on. Lower Hartree-Fock orbitals are thereby affected less due to screening by surrounding fermions. States located near the chemical potential and above ($i \geq 3$) however show a strongly distorted oscillatory behavior which gives rise to an essential change in the realized (renormalized) one-particle energies. Apart from the confined system considered here, $\mathbf{A}(\omega)$ thus allows—in great detail—to study e.g. field ionization processes in many-body systems with continuum states.

In addition, one can conclude from Fig. 6.7 and Fig. 6.8 that, if correlation effects lead to Green's functions rapidly decaying perpendicular to the time diagonal, one actually may improve the time-propagation scheme. Instead of steadily expanding the square $\mathcal{S} = [t_0, t_1] \times [t_0, t_2]$, one may integrate the Keldysh/Kadanoff-Baym equations more efficiently on a strip along the time diagonal [74]. The respective width $\Delta\theta$ will then directly correspond to the mean lifetime of all quasi-particle states $|\Phi_k\rangle$ with $k = 0, \dots, n_b - 1$.

6.3. Kohn mode in a quantum many-body system

In the previous sections, one has studied the system response under influence of a laser field in dipole approximation. Here, the aim is to particularly examine the energy and what temporally happens with the density profile $n(x, t)$ during such a laser excitation.

Fig. 6.9 gives—for the case of $N = 3$ confined fermions in Hartree-Fock approximation—the time-evolution of the different energies during a near-resonant dipole excitation. While the (HF)

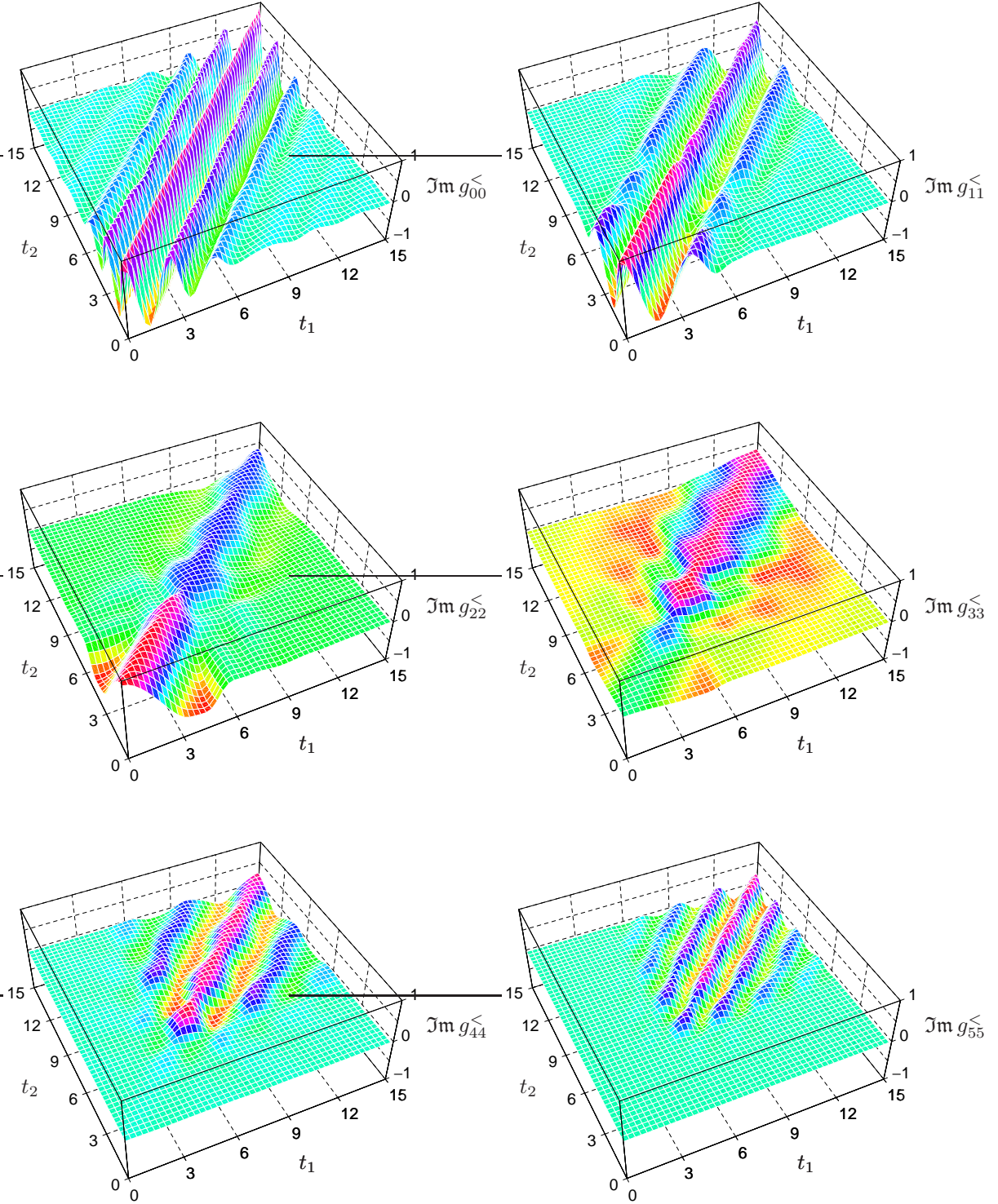


Figure 6.7: Nonequilibrium time-propagation in second Born approximation: $N = 3$ harmonically confined fermions under the influence of a laser pulse centered at $t = 5$. Displayed is the two-time evolution of the imaginary part of the lesser correlation functions $g_{ii}^{<}(t_1, t_2)$ with $i \leq 5$. All times are measured in units of the reciprocal confinement frequency Ω . System parameters: $\beta = 3.0$ and $\lambda = 1.0$. The field parameters coincide with the ones given in Fig. 6.5.

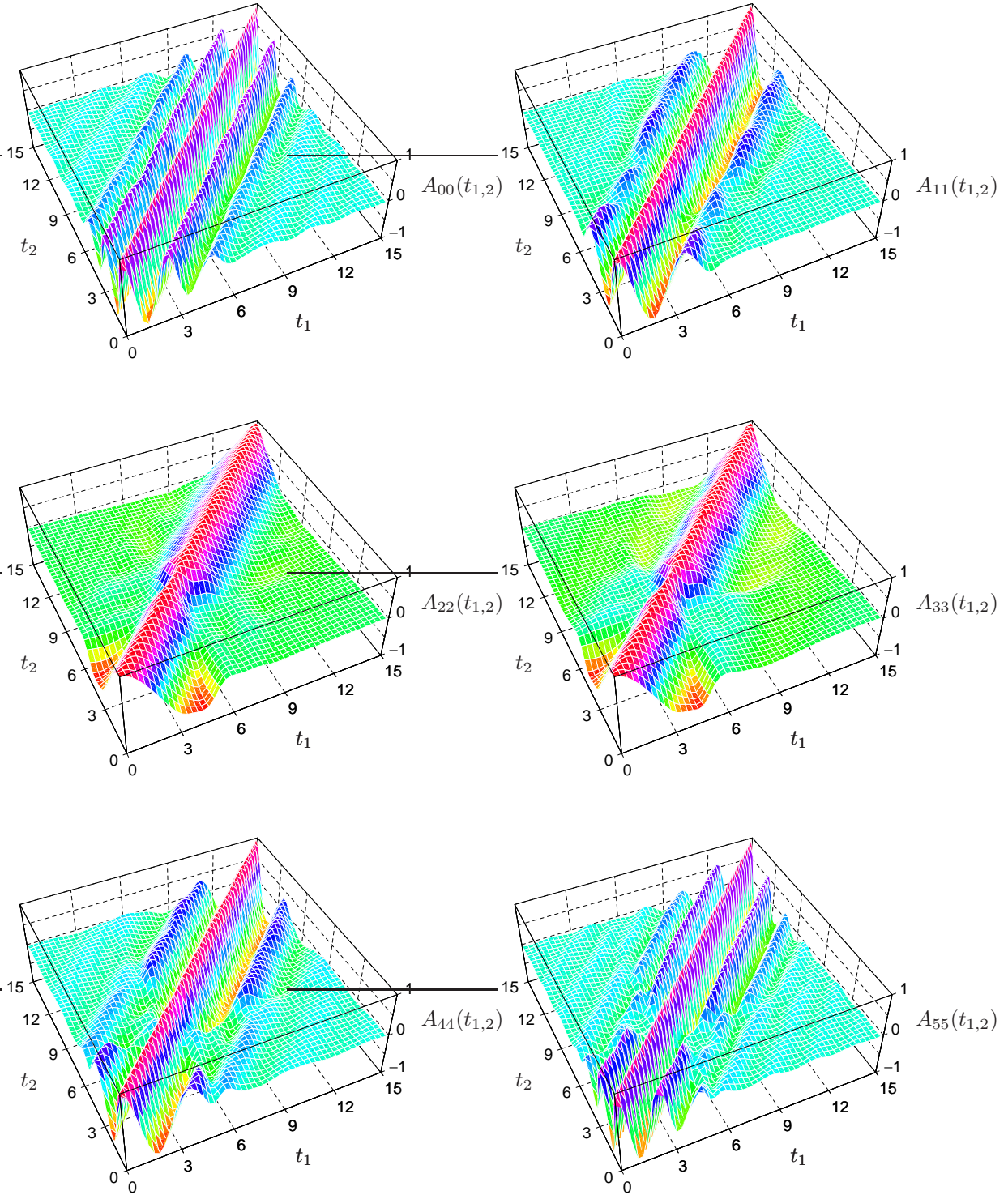


Figure 6.8: Nonequilibrium spectral function $A_{ii}(t_1, t_2)$ with $i \leq 5$, corresponding to Fig. 6.7. $N = 3$ trapped fermions under the influence of a laser pulse centered at $t = 5$. All times are measured in units of the reciprocal confinement frequency Ω . The system and field parameters are as in Fig. 6.7.

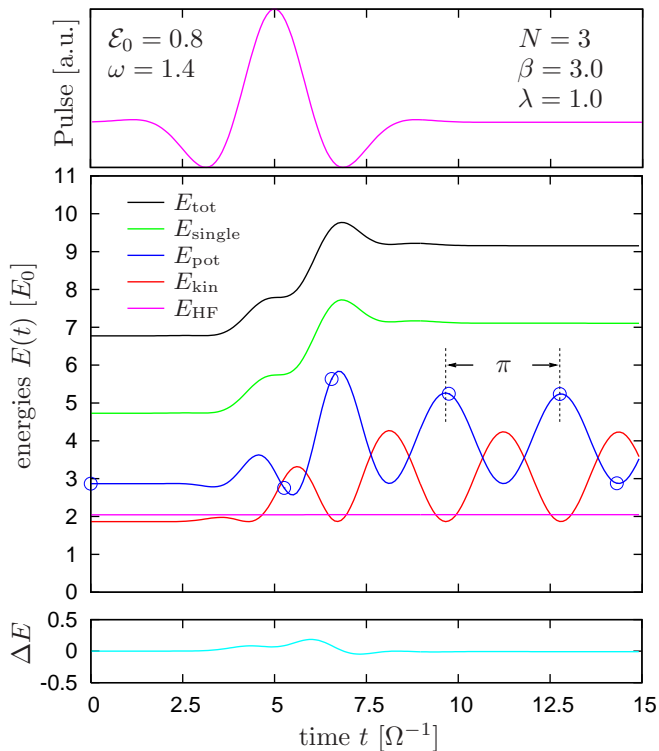


Figure 6.9: $N = 3$ trapped fermions in Hartree-Fock approximation, $\lambda = 1.0$: Time-evolution of the different energies during dipole excitation according to Eqs. (6.2) and (6.3). The upper panel qualitatively shows the pulse amplitude $\mathcal{E}(t)$. The numerical error ΔE in the lower panel is computed from Eq. (6.4). After the pulse the kinetic and potential energy oscillate 180° out of phase while all other contributions are constant. The period is exactly π which corresponds to an oscillation with exactly the double trap frequency Ω . The number of propagated time-steps is $n_\Delta = 175$. The circles \circ indicate the time points analyzed for the density in Fig. 6.10. For all pulse parameters see equally Fig. 6.10.

mean-field energy stays essentially constant, the kinetic and potential energy both increase and characteristically start to oscillate in time, whereby the respective sum, $E_{\text{single}}(t)$, does no longer change when the pulse has passed. Further, the increase of the total energy clearly indicates that the laser pulse (shown qualitatively in the upper panel) has excited the trapped Fermi liquid.

The quantity ΔE , shown in the lower panel of Fig. 6.9, is a measure of the numerical error by comparison of the work done by the dipole field (cf. Eq. (4.75) of Sect. 4.5.3) with the time-evolution of the total energy, i.e. more precisely

$$\Delta E = [E_{\text{tot}}(t) - E_{\text{tot}}(0)] + E_{\text{field}}(t), \quad (6.4)$$

where $E_{\text{tot}}(0)$ denotes the initial total energy of the system in equilibrium—bear in mind that $E_{\text{field}}(t)$ is by definition negative. As the plot shows, ΔE is relatively small compared to the total energy of the trapped particle ensemble. Moreover, this error can be further reduced by simply making the length of the time-step smaller, i.e. by increasing n_Δ .

Turning back to the oscillations of the kinetic and potential energy, one ascertains that both are sinusoidal with a phase difference of 180° and a time period of exactly π . The corresponding frequency is thus equal to the double trap frequency Ω , from which one concludes that the laser field induces the performance of a harmonic oscillation of the trapped ensemble. That this is true, becomes obvious when separating the exact N -particle Hamiltonian of Eq. (5.1), including the dipole field (6.2), into the center of mass (COM) coordinate, $R = \frac{1}{N} \sum_k x_k$, and a number of $(N - 1)$ relative coordinates, r_i . In dimensionless coordinates one then arrives at

$$H(t) = H_{\text{com}}(t) + H_{\text{rel}}, \quad (6.5)$$

$$H_{\text{com}}(t) = \frac{1}{2} (-\partial_R^2 + R^2) + \mathcal{E}(t) R, \quad (6.6)$$

$$H_{\text{rel}} = \sum_{i=1}^{N-1} \frac{1}{2} (-\partial_{r_i}^2 + r_i^2) + \sum_{i < j} w(r_i - r_j), \quad (6.7)$$

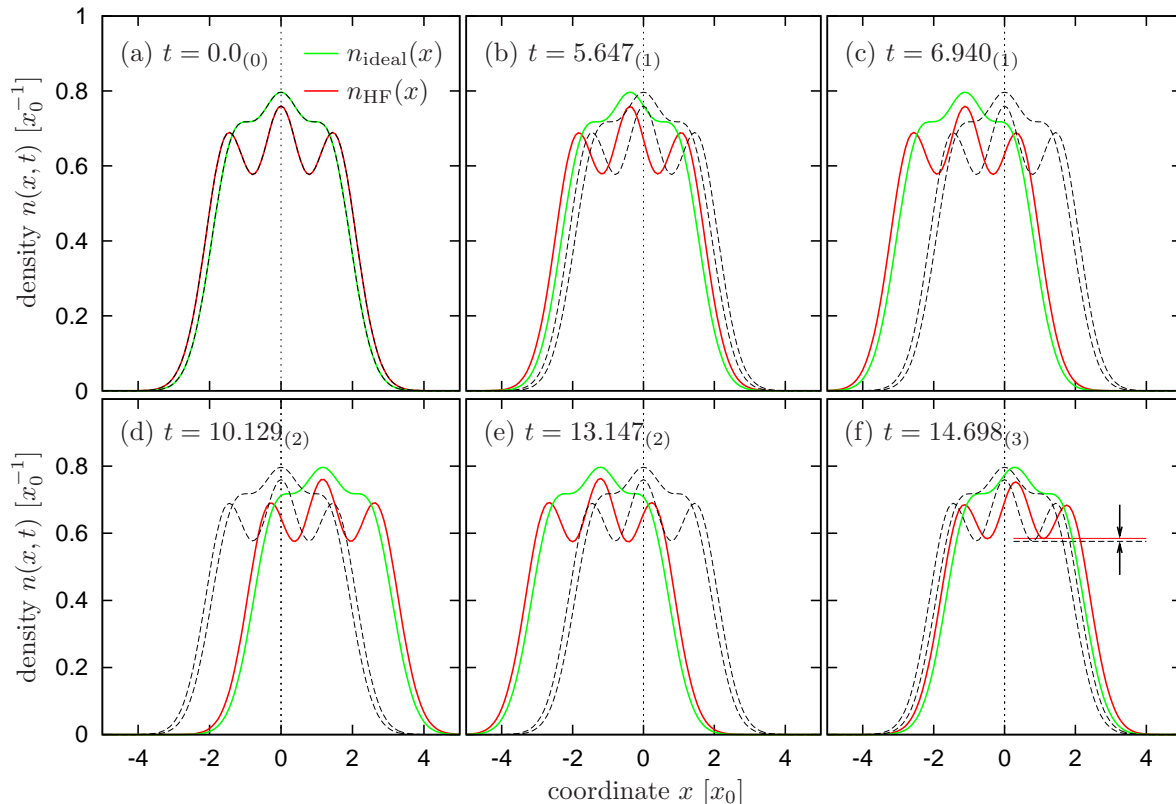


Figure 6.10: Nonequilibrium density $n(x, t)$ for $N = 3$ trapped fermions at different points t in time (compare with Fig. 6.9). The green lines indicate the density of the noninteracting system and the red curves give the HF result with $\lambda = 1$. The temperature is chosen to $\beta = 3.0$. (a-f) During dipole excitation the initial (static) density profile becomes translated—corresponding to the excitation of the Kohn (COM) mode—but do not change shape. The numbers in brackets count the oscillation periods. (f) Small errors especially in the local minima and maxima are due to the finite basis constructed from $n_b = 14$ HF orbitals. Pulse parameter: Gaussian envelope centered at $t = 5.0$, amplitude $\mathcal{E}_0 = 0.8$ and width $\Delta t^2 = 1.5$ —near resonant situation with laser frequency $\omega = 1.4$.

where both contributions $H_{\text{com}}(t)$ and H_{rel} commute, i.e. $[H_{\text{com}}, H_{\text{rel}}]_- = 0$, and the quantity $\mathcal{E}(t)$ now combines electric field and dipole moment, i.e. is measured in multiples of $\frac{\hbar\Omega}{q_0 x_0}$. Since the dipole field now enters Eq. (6.6) only, the laser pulse unambiguously excites the center of mass (or sloshing) mode which occurs exactly at the trap frequency Ω —kinetic and potential energy oscillate consequently with 2Ω as in the case of a single particle.

Moreover, as the particle interaction only appears in the relative Hamiltonian, Eq. (6.7), one notices that the center of mass motion of the system is not affected by any pair-interaction potential $w(x_i - x_j)$, and, consequently, that the density profile—following temporally the COM—has to be rigidly translated in space. This is exactly the statement of the well-known *Kohn theorem* [5, 46] for harmonically confined many-body systems, and, for this reason, the center of mass oscillation is also known as the *Kohn mode* in the literature.

However, in contrast to the consideration of the exact Hamiltonian (6.5), one in the present work has been restricted to apply essential approximations to the pair-interaction w . In this point of view, it is not obvious that the approximate treatment of the interaction leads directly to the fulfillment of the Kohn theorem as a separation into COM and relative coordinates can in general not be realized. Fortunately, there is a way out: It has recently been proven by

Bonitz *et al.* [72], that any bosonic or fermionic approximation of many-body theory which preserves density and momentum does satisfy the Kohn theorem. To present explicit details of this proof would go beyond the scope of this work, but the most important essence is that the demand of density and momentum conservation is just the consequence of the Kadanoff-Baym criteria (A) and (B) formulated in Sect. 3.1. As the approximations applied here generally obey these criteria, the question if one should correctly preserve the Kohn mode is answered in the affirmative.

A numerical verification gives Fig. 6.10, which, for the ideal system of $N = 3$ trapped fermions and for the respective interacting system in Hartree-Fock approximation, shows the spatial density profile at different times $t \geq 0$. The specific values of t thereby relate to the times marked in the potential energy of Fig. 6.9. Without doubts, the Kohn theorem is well satisfied, and—induced by the dipole field—the density is rigidly oscillating at the trap frequency Ω , i.e. $n(x, t) = n(x - R(t), 0)$, where $R(t)$ denotes the time-dependence of the center of mass variable. Small errors which accumulate are thereby clearly attributed to the finite number of basis functions used in the computations.

In conclusion, the time-dependent density profile $n(x, t)$ —being rigidly translated according to the Kohn mode—has turned out to be a much more severe test on the numerical quality than just particle number or energy conservation. Combining temporal and spatial information, the examination of the density response is in particular useful when going beyond the mean-field level and describing the correlated dynamics in second Born approximation which is, according to Ref. [72], also in agreement with the Kohn theorem.

7. Conclusion and outlook

In the present work, one has investigated *artificial atoms* [8]—interacting confined quantum many-body systems of strongly inhomogeneous density—using the technique of nonequilibrium Green’s functions (NEGF) [14]. More precisely, one has numerically solved the kinetic equations for the NEGF—the Keldysh/Kadanoff-Baym equations (KKBE) [14, 22]—on a correlated level which has been obtained by applying a (Φ -derivable) conserving many-body approximation [54] to the interparticle interaction. One has thereby employed both imaginary- and real-time Green’s functions in order to work on the full Schwinger/Keldysh time-contour [22] (see Fig. 2.1) which—besides the physically related real time axis—has an additional imaginary branch ranging from an initial time t_0 to the imaginary coordinate $t_0 - i\beta$, where β denotes the inverse temperature that enters the grand canonical density operator $\frac{1}{Z}e^{-\beta[H-\mu N]}$. The imaginary-time Green’s function has then allowed one to compute the correlated thermodynamic equilibrium (initial) state of the artificial atom [20], including most of its physical properties, and the extension of this Green’s function into the real time domain has led to the time-evolution of the correlated initial state under an arbitrary nonequilibrium situation dictated by a time-dependent many-body Hamiltonian $H(t)$, with $t \geq t_0$.

Whereas the numerical code, discussed in Chap. 4, has allowed for a straightforward implementation of the Keldysh-contour [15, 51, 60], it has been much more intricate to include the space variables of the one-particle Green’s function $G(1, 2)$, $1 = (x_1, t_1)$, when applying the technique of NEGF to spatially inhomogeneous systems. To this end, it has been found highly useful to expand the Green’s functions and all other quantities entering the KKBE in terms of (mean-field) Hartree-Fock orbitals (HFO) [16]. These one-particle orbitals have been separately obtained from a self-consistent Hartree-Fock (SCHF) [59] calculation which has been performed as a preliminary. Besides the fact that the Green’s functions, therewith, have transformed into time-dependent matrices, the HFO representation has revealed additional advantages for the solution of the Keldysh/Kadanoff-Baym equations, the numerical algorithm of which is subdivided into two parts: First, the determination of the correlated thermodynamic equilibrium state, and, second, the time-propagation of this state under nonequilibrium conditions. Regarding the former, the SCHF procedure has given direct access to the imaginary-time (Matsubara) Green’s function on the uncorrelated Hartree-Fock level, which then has been used as reference quantity to iteratively solve the equilibrium part of the KKBE (the self-consistent Dyson equation) including effects of particle collisions—throughout, correlations have thereby included in second Born approximation [14]. Concerning the latter, the HFO representation of the Green’s functions has led to an essentially simpler propagation scheme for the correlated quantum many-body system, since the time-evolution now involves time-dependent matrices instead of functions that depend on two space-time coordinates 1 and 2.

Turning back to the artificial atoms, the functionality of the numerical algorithm has been demonstrated by its application to a representative model system, Chap. 5. At the example of a one-dimensional quantum dot (assumed to be realized by a parabolic potential) confining a small number of spin-polarized fermions (interacting via Coulomb repulsion) one has studied the Green’s functions in equilibrium and nonequilibrium. From the Matsubara Green’s function one has computed the spatial equilibrium density at Hartree-Fock and second Born level in

dependence on particle number, $N \leq 6$, inverse temperature¹, $\beta/\beta_0 > 1/2$, and relative interaction strength², $\lambda < 3$. It has turned out that the Hartree-Fock approximation already gives adequate results and that improvements, induced by correlations, lead to deviations from the HF result in substance for moderate temperatures, $\beta/\beta_0 \approx 2$. Aside from the density profile, one has examined what happens to the equilibrium distribution function—expressed in terms of the Hartree-Fock orbital energies—when correlations effects are "turned on", and, in addition, the total energy of the "trapped Fermi liquid" has been calculated in dependence on (N, β, λ) . Regarding the total energies, a comparison with path integral Monte Carlo (PIMC) simulations [13] has revealed good agreements apart from evident deviations that originate from the use of different statistical ensembles. Further, the time-evolution of the initial state has offered important implications for the equilibrium properties: Besides verifying the macroscopic conservation laws (incorporated via the conserving many-body approximations), the temporal behavior of the correlation energy has allowed one, in detail, to estimate the numerical accuracy of the Matsubara Green's function and, thus, the quality of the equilibrium state including the related macrophysical observables.

Aside from equilibrium, it has been demonstrated that the two-time propagation of the Green's function can be successfully used to study the system (initially in thermodynamic equilibrium) under nonequilibrium conditions, Chap. 6. As an example, one has looked at the time-evolution of the artificial atom—as is specified above—under a time-dependent pulsed laser field in dipole approximation, and has analyzed the correlated quantum dynamics imprinted by the Rabi energy which combines the dipole field and the HF mean-field into an overall effective potential. In parallel, the time-dependent occupation probabilities of the Hartree-Fock orbitals have clearly allowed for a distinction of different excitation regimes as there are (near-)resonant and off-resonant situations depending on the ratio of the laser frequency to the confinement frequency of the parabolic trap. Rather briefly, one has also touched the spectral function which, as a matter of principle, gives access to the renormalized one-particle spectrum, if correlations and dipole field are present, respectively. Beyond this scope, the density response of the chosen artificial atom to the dipole excitation has been found extremely useful to prove the correctness of the algorithm and to estimate the numerical accuracy. This is because the Kohn theorem [5, 46] predicts for an interacting harmonically confined system (when treated *exactly*), that, during dipole excitation, the density temporally retains its shape over the whole coordinate space and is rigidly translated according to the motion of a single particle in a driven harmonic oscillator (center of mass mode). Further, as this statement also holds within a (Φ -derivable) conserving many-body approximation [72], the corresponding verification by means of the numerically obtained density has turned out to be a very sensitive test for the code—essentially more sensitive than just energy conservation or fulfillment of the continuity equation.

Furthermore, regarding the specific artificial atom the investigation of which is striven for, there exist only little restrictions as long as the applied many-body approximation leads to acceptable macroscopic observables. More crucial limitations of the present approach are due to the numerics itself: The key point is the number of basis functions (Hartree-Fock orbitals) which determines the dimension of the matrices (Sect. 3.3) and, thus, directly assigns the complexity of the numerical computations. As one is generally forced to provide a sufficiently large number of Hartree-Fock orbitals to ensure the convergence of macroscopic quantities, the calculations can rapidly become sophisticated. In addition, the addressed convergence with the number of basis functions does implicitly and not slightly depend on particle number, temperature and relative interaction strength. With this in mind, the presented nonequilibrium Green's function approach to artificial atoms is applicable to small and mesoscopic quantum systems at zero and

¹ $\beta_0 = (\hbar\Omega)^{-1}$, where Ω denotes the confinement frequency.

²Corresponding to the separation $H = H_1 + \lambda H_{12}$ of the Hamiltonian (see Sect. 1.2).

low temperatures, but becomes clearly unfeasible in the thermodynamic limit, $N \rightarrow \infty$.

In conclusion, despite of these general limitations, the description of confined quantum systems using the technique of NEGF has turned out to be a very reliable method for examining the system properties in thermodynamic equilibrium and in nonequilibrium with special attentions to strong external fields the incorporation of which allows for an unperturbative treatment. Moreover, as the corresponding algorithm has been established on a very general level, the application to a variety of other quantum systems is straightforward. For that purpose, one simply needs to provide the relevant input quantities—primarily the matrices (one- and two-electron integrals) $h_{ij}^0(t) = t_{ij} + v_{ij}(t)$ and $w_{ij,kl}$, see Sect. 4.4 and definitions (3.36) and (3.48)—within an adequate natural orbital representation.

Outlook:

Subject of ongoing work is to apply the Keldysh/Kadanoff-Baym approach also to other artificial quantum systems—for instance, to electrons in double quantum dots or to systems with an even more sophisticated confinement. In particular, the aim is to extend the presented method to the two-dimensional case which is of essentially more relevance in actual research, and, unambiguously, will clear up the limitations of the numerical algorithm as the corresponding computations are expected to be much more intricate³. In addition, the question arises how efficiently inhomogeneous systems of interacting bosons can be analyzed by using the presented technique of nonequilibrium Green's functions. So far, this question stays unresolved since actual calculations have been performed on fermionic systems only⁴.

Concerning rather technical issues, it is further a good idea to test many-body approximations other than the second Born approximation—e.g. the *GW* method⁵. In addition, one is free to insert specific model self-energies in order to study the implications for the system's total energy, its temporal conservation or other macroscopic observables.

Beyond this scope, one may also think of generalizing the approach towards quantum systems, which allow for ionization or transport processes and in which the particle number is not necessarily constant in time. Finally, also the systematical inclusion of spin degrees of freedom into the numerical code may be a point of consideration—in particular, when aiming at applying magnetic fields.

³Practically, in 2D, the Hartree-Fock orbitals will take an additional quantum number accounting for the degree of freedom in y -direction, i.e. $\Phi_m(x) \rightarrow \Phi_{m,l}(x,y)$. Consequently, the size of the basis $\{\Phi_{m,l}(x,y)\}$ increases quadratically with the number n_b of realized quantum numbers; $m, l = 0, 1, \dots, n_b - 1$. Under a special symmetry, e.g. using polar coordinates, this trend may be of course weakened.

⁴However, as the Keldysh/Kadanoff-Baym equations equally apply to Fermi and Bose systems, the generalization to bosons is, in principle, straightforward.

⁵This Φ -derivable approximation incorporates a dynamically screened interaction [49, 14].

A. Matrix elements in oscillator representation

A.1. Kinetic/potential energy and dipole moment

To derive expressions for the kinetic and potential energy in the harmonic oscillator representation, one starts from the noninteracting Hamiltonian in dimensionless coordinates, i.e. from $h^0(x) = \frac{1}{2} \frac{\partial^2}{\partial x^2} + \frac{1}{2} x^2$ as given in the introduction (Sect. 1.2)—the characteristic length scale reads $x_0 = \sqrt{\hbar/(m\Omega)}$ and energies are measured in multiples of $\hbar\Omega$. Solutions of the stationary Schrödinger equation, $h^0(x) \phi_n(x) = \epsilon_n \phi_n(x)$, are the familiar oscillator wave functions [52]

$$\phi_n(x) = \frac{1}{\sqrt{2^n n! \sqrt{\pi}}} e^{-\frac{x^2}{2}} H_n(x), \quad n = 0, 1, 2, \dots, \quad (\text{A.1})$$

with energy eigenvalues $\epsilon_n = n + \frac{1}{2}$. Thus, it is $h_{kl}^0 = (k + \frac{1}{2}) \delta_{kl}$ with $k, l = 0, 1, 2, \dots$. The Hermite polynomials $H_n(x)$ appearing in (A.1) are defined by

$$H_n(x) = (-1)^n e^{x^2} \frac{d^n}{dx^n} \left(e^{-x^2} \right), \quad n \in \mathbb{N}, \quad (\text{A.2})$$

and fulfill the recursion relation $H_{n+1}(x) = 2x H_n(x) - 2n H_{n-1}(x)$. The potential energy matrix \mathbf{v} is then obtained from the integrals

$$v_{kl} = \frac{1}{2} \int_{-\infty}^{+\infty} dx \phi_k^*(x) x^2 \phi_l(x) \quad (\text{A.3})$$

$$= \frac{1}{2 \sqrt{2^{k+l} k! l! \pi}} \int_{-\infty}^{+\infty} dx \exp(-x^2) H_k(x) x^2 H_l(x) \quad (\text{A.4})$$

$$= \frac{1}{4 \sqrt{2^{k+l} k! l! \pi}} \int_{-\infty}^{+\infty} dx \exp(-x^2) H_k(x) \left[\frac{1}{2} H_2(x) + H_0(x) \right] H_l(x)$$

$$= \frac{1}{4 \sqrt{2^{k+l} k! l! \pi}} \left(\frac{2^{s_1} k! 2! l! \sqrt{\pi}}{2 (s_1 - k)! (s_1 - 2)! (s_1 - l)!} t_1 + \frac{2^{s_2} k! 0! l! \sqrt{\pi}}{(s_2 - k)! (s_2 - 0)! (s_2 - l)!} t_2 \right)$$

$$= \frac{1}{4} \sqrt{\frac{k! l!}{2^{k+l}}} \left(\frac{2^{s_1} t_1}{(s_1 - k)! (s_1 - 2)! (s_1 - l)!} + \frac{2^{s_2} t_2}{(s_2 - k)! s_2! (s_2 - l)!} \right)$$

$$= \frac{1}{4} \sqrt{\frac{k! l!}{2^{k+l}}} \left(\frac{1}{(s_1 - k)! (s_1 - 2)! (s_1 - l)!} + \frac{1}{2 (s_1 - 1 - k)! (s_1 - 1)! (s_1 - 1 - l)!} \right) 2^{s_1} t_1$$

$$= \frac{1}{4} \sqrt{\frac{k! l!}{2^{k+l}}} \left(\frac{(s_1 - 1)}{(s_1 - k)! (s_1 - 1)! (s_1 - l)!} + \frac{1/2 (s_1 - k) (s_1 - l)}{(s_1 - k)! (s_1 - 1)! (s_1 - l)!} \right) 2^{s_1} t_1$$

$$= \sqrt{\frac{k! l!}{2^{k+l}}} \frac{2^{s_1} t_1 [(s_1 - 1) + 1/2 (s_1 - k) (s_1 - l)]}{4 (s_1 - k)! (s_1 - 1)! (s_1 - l)!}$$

$$= \frac{\sqrt{k! l!} [(k + l) - (k - l)^2/4 + 1]}{4 (s_1 - k)! (s_1 - 1)! (s_1 - l)!} t_1$$

$$= \begin{cases} \frac{\sqrt{k! l!} [(k + l) - (k - l)^2/4 + 1]}{4 (s - k)! (s - 1)! (s - l)!}, & s = (k + l)/2 + 1 \in \mathbb{Z} \\ 0, & \text{otherwise} \end{cases}, \quad (\text{A.5})$$

A. Matrix elements in oscillator representation

where one has introduced $s_1 = \frac{1}{2}(k + 2 + l)$, $s_2 = \frac{1}{2}(k + l)$ with $s_2 = s_1 - 1$, and defined the quantities $t_{1,2}$ which equal one if and only if $s_{1,2} \in \mathbb{Z}$ and otherwise zero. Furthermore, one has expanded x^2 in terms of Hermite polynomials to evaluate (A.4), i.e.

$$x^2 = \frac{1}{4} H_2(x) + \frac{1}{2} H_0(x), \quad H_0(x) = 1, \quad H_1(x) = 2x, \quad H_2(x) = 4x^2 - 2. \quad (\text{A.6})$$

For the spatial integrations, it is convenient to use the identity given e.g. in Ref. [75, 69]: With $s = \frac{1}{2}(a + b + c)$ it is

$$\int_{-\infty}^{+\infty} dx \exp(-x^2) H_a(x) H_b(x) H_c(x) = \begin{cases} \frac{2^s a! b! c! \sqrt{\pi}}{(s-a)!(s-b)!(s-c)!}, & s \in \mathbb{Z} \\ 0, & \text{otherwise} \end{cases}. \quad (\text{A.7})$$

Here and in the expressions above, it means $(-n)! := 0$ for every $n \in \mathbb{N}$. With the potential energy, the matrix elements of the kinetic energy then easily follow from the full Hamiltonian as $\mathbf{t} = \mathbf{h}^0 - \mathbf{v}$.

Moreover, the matrix elements corresponding to the dipole moment are simple to evaluate within the oscillator representation. Using expressions (A.6) and (A.7) one obtains

$$\frac{d_{kl}}{q_0} = \int dx \phi_k^*(x) x \phi_l(x) = N_{kl} \int dx e^{-x^2} H_k(x) x H_l(x) = \sqrt{\frac{l}{2}} \delta_{k+1,l} + \sqrt{\frac{k}{2}} \delta_{k,l+1}, \quad (\text{A.8})$$

where q_0 denotes the particle charge, N_{kl} accounts for normalization, and one finds non-zero entries only on the secondary diagonals.

A.2. Matrix elements of pair-interaction potentials

A.2.1. Contact interaction

One of the most simple types of pair-interaction is the so called on-site or contact interaction, where the potential is assumed to be of the local form $w(x, x') = \frac{\alpha}{x_0} \delta(x - x')$. Here, α denotes the interaction strength and its sign decides if the potential is repulsive or attractive. Further, x_0 is the characteristic confinement length as given in A.1. The calculation of the corresponding matrix elements is straightforward—with the indices arranged as in Eq. (3.48) or Eq. (4.5), one obtains

$$w_{ij,kl} = \frac{\alpha}{x_0} \iint dx dx' \phi_i^*(x) \phi_k^*(x') \delta(x - x') \phi_j(x) \phi_l(x') \quad (\text{A.9})$$

$$= \frac{\alpha N_{ijkl}}{x_0} \int dx \exp(-2x^2) H_i(x) H_k(x) H_j(x) H_l(x) \quad (\text{A.10})$$

$$= \frac{\alpha N_{ijkl}}{\sqrt{2} x_0} \int dy \exp(-y^2) H_i(y/\sqrt{2}) H_k(y/\sqrt{2}) H_j(y/\sqrt{2}) H_l(y/\sqrt{2})$$

$$= \frac{\alpha N_{ijkl}}{\sqrt{2} x_0} \int dy \exp(-y^2) \sum_{\gamma} c_{\gamma} H_{\gamma}(y)$$

$$= \frac{\alpha N_{ijkl}}{\sqrt{2} x_0} \sum_{\gamma} c_{\gamma} \int_{-\infty}^{+\infty} dy \exp(-y^2) H_{\gamma}(y) H_0(y) \quad [1 \equiv H_0(y)]$$

$$= \frac{\alpha N_{ijkl}}{\sqrt{2} x_0} \sum_{\gamma} \frac{c_{\gamma}}{N_0 N_{\gamma}} \delta_{\gamma 0} = \frac{\alpha N_{ijkl}}{\sqrt{2} x_0} \frac{c_0}{N_0^2} = \frac{\alpha N_{ijkl}}{x_0} \sqrt{\frac{\pi}{2}} c_0, \quad (\text{A.11})$$

where $N_m = (\sqrt{2^m m! \sqrt{\pi}})^{-1}$ and $N_{ijkl} = N_i N_j N_k N_l$. The remaining problem concerning (A.11) is to determine the expansion coefficient c_0 which parametrically depends on all four indices, i.e. $c_0 = c_0^{(ijkl)}$. However, c_0 only accounts for the constant terms in the four-fold product of Hermite polynomials and, thus, can easily be accessed via the following recursion relation,

$$c_0^{(ijkl)} = a_i a_j a_k a_l, \quad a_n = -2(n-1)a_{n-2}, \quad a_0 = 1, \quad a_1 = 0, \quad (\text{A.12})$$

One finally arrives at

$$w_{ij,kl} = \frac{\alpha}{\sqrt{\pi} x_0} \frac{a_i a_j a_k a_l}{\sqrt{2^{i+j+k+l+1} i! j! k! l!}}, \quad (\text{A.13})$$

whereby a different arrangement of the indices does not change the value of $w_{ij,kl}$.

At the end of Sect. 5.1, one has briefly discussed the implications of $w_{ij,kl}$ on the Hartree-Fock and the correlation energy. As in the respective self-energies, Eqs. (3.57) and (3.58) in Sect. 3.3.1, enter the combinations of matrix elements

$$\Sigma^{\text{HF}} : \quad w_{kl,ij} \pm w_{kj,il}, \quad (\text{A.14})$$

$$\Sigma^{\text{corr,B}} : \quad w_{ik,ms} (w_{lj,rn} \pm w_{nj,rl}), \quad (\text{A.15})$$

with $\pm =$ (bosons/fermions), one directly concludes that for contact-interacting fermions (confined in a one-dimensional parabolic trap) $\Sigma^{\text{HF}} = \Sigma^{\text{corr,B}} = 0$, i.e. the system behaves exactly as the ideal one.

A.2.2. Coulomb

To evaluate the matrix elements for the 1D Coulomb potential, $w(x, x') = \frac{\alpha}{x_0} \frac{1}{|x-x'|}$, one has to overcome the problem of the singularity at $|r| = |x-x'| = 0$ which leads to divergent integrals. The most natural way of preventing the discontinuity, is to introduce a small parameter a replacing $|r| \rightarrow \sqrt{r^2 + a^2}$. This eliminates the singularity and yields a harmonic behavior around $r = 0$ as shown in Fig. A.1. The corresponding matrix elements are accessible through

$$\begin{aligned} w_{ab,cd} &= \iint dx dx' \phi_a^*(x) \phi_c^*(x') W(x, x') \phi_b(x) \phi_d(x') \\ &= \alpha N_{abcd} \iint dx dx' \frac{H_a(x) H_b(x) H_c(x') H_d(x')}{x_0 \sqrt{r^2 + a^2}} e^{-x^2 - x'^2} \\ &= \frac{\alpha N_{abcd}}{x_0} \iint dR dr \frac{e^{-2R^2 - r^2/2}}{\sqrt{r^2 + a^2}} H_a(R + r/2) H_b(R + r/2) H_c(R - r/2) H_d(R - r/2) \\ &= \frac{\alpha N_{abcd}}{x_0} \iint dR dr \frac{e^{-2R^2 - r^2/2}}{\sqrt{r^2 + a^2}} H_{abcd}(R, r), \end{aligned} \quad (\text{A.16})$$

where $N_{abcd}^{-1} = \pi \sqrt{2^{a+b+c+d} a! b! c! d!}$ accounts for normalization and one further has introduced center-of-mass and relative coordinates, $r = x - x'$ and $R = (x + x')/2$. In (A.16), the products of Hermite polynomials at positions $R \pm r/2$ can then be rewritten in the form

$$H_{abcd}(R, r) = \sum_{ij} C_{ij}^{(abcd)} R^i r^j, \quad (\text{A.17})$$

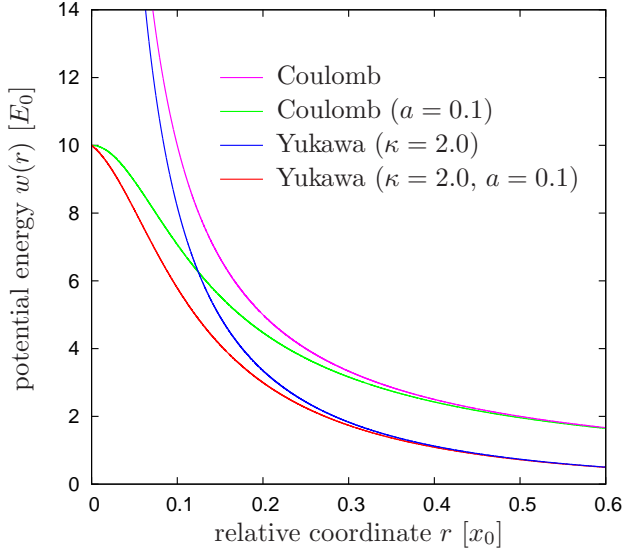


Figure A.1: Pure Coulomb and pure Yukawa potential $w(r)$ in comparison with their approximate forms containing the replacement $|r| \rightarrow \sqrt{r^2 + a^2}$. Parameters are chosen as indicated within the figure. For the modified Coulomb potential it is in particular $\partial_r w(r)|_{r=0} = 0$.

where the coefficients C_{ij} follow from the relation

$$H_n \left(R \pm \frac{r}{2} \right) = \sum_{2k \leq n} \sum_{l=0}^{n-2k} \frac{(-1)^k 2^{n-2k} n!}{k! l! (n-2k-l)!} R^{n-2k-l} \left(\pm \frac{r}{2} \right)^l. \quad (\text{A.18})$$

Combining Eqs. (A.16) and (A.17), one finds that

$$\begin{aligned} w_{ab,cd} &= \frac{\alpha N_{abcd}}{x_0} \sum_{ij} C_{ij}^{(abcd)} \int_{-\infty}^{\infty} dR \exp(-2R^2) R^i \int_{-\infty}^{\infty} dr \frac{r^j \exp(-r^2/2)}{\sqrt{r^2 + a^2}} \\ &= \frac{\alpha N_{abcd}}{x_0} \sum_{ij} C_{ij}^{(abcd)} \alpha_i \beta_j, \end{aligned} \quad (\text{A.19})$$

where the integrations over R and r are summarized in expressions α_i and β_j , respectively. These can separately be calculated using the analytical result

$$\alpha_n = \int_{-\infty}^{\infty} dR \exp(-2R^2) R^n = 2^{-\frac{3+n}{2}} (1 + (-1)^n) \Gamma \left(\frac{1+n}{2} \right), \quad (\text{A.20})$$

and

$$\beta_n = \int_{-\infty}^{\infty} dr \frac{r^n \exp(-r^2/2)}{\sqrt{r^2 + a^2}} = \begin{cases} \sqrt{\pi} \prod_{k=0}^{\frac{n}{2}-1} (2k+1) U \left(\frac{1}{2}, 1 - \frac{n}{2}, \frac{a^2}{2} \right) & , n \text{ even} \\ 0 & , n \text{ odd} \end{cases}, \quad (\text{A.21})$$

where U denotes the confluent hypergeometric function, defined by the integral

$$U(a, b, z) = \frac{1}{\Gamma(a)} \int_0^{\infty} dt e^{-zt} t^{a-1} (1+t)^{b-a-1}. \quad (\text{A.22})$$

As obtainable from (A.16), the interaction matrices in particular obey the symmetries

$$w_{ab,cd} = w_{ba,cd} = w_{ab,dc} = w_{ba,dc} = w_{cd,ab}. \quad (\text{A.23})$$

A.2.3. Yukawa

For Yukawa interacting particles, the pair-interaction potential takes the form

$$w(x, x') = \frac{\alpha}{x_0 |x - x'|} \exp(-\kappa |x - x'|) , \quad (\text{A.24})$$

where the additional exponential function shields the long-range $1/|r|$ behavior with a screening constant κ . See Fig. A.1 for a comparison with the Coulomb interaction. Since the Yukawa potential is also singular at $r = |x - x'| = 0$, one again can replace $|r|$ by $\sqrt{r^2 + a^2}$ in the denominator of (A.24). The strategy to determine the matrix elements is then analogous to the Coulomb case, i.e. one uses center-of mass and relative coordinates (R, r) to write

$$w_{ab,cd} = \frac{\alpha N_{abcd}}{x_0} \sum_{ij} C_{ij}^{(abcd)} \int_{-\infty}^{\infty} dR e^{-2R^2} R^i \int_{-\infty}^{\infty} dr \frac{r^j e^{-\frac{r^2}{2} - \kappa|r|}}{\sqrt{r^2 + a^2}} , \quad (\text{A.25})$$

where the coefficients $C^{(abcd)}$ are the same as in Eq. (A.17). However, while the first integration over dR equals expression (A.20), the second integral is involved and has in general to be computed numerically.

B. Time-propagation of the Green's functions

B.1. Time-stepping $\mathbf{g}^*(T) \rightarrow \mathbf{g}^*(T + \Delta)$, $\star \equiv \{\gtrless, \lceil/\rceil\}$

In the following, the Keldysh/Kadanoff-Baym equations in the form of Eqs. (4.47-4.50) in Chap. 4 are integrated for a small time step of length Δ , [15]. That is the quantities

$$\begin{aligned} \mathbf{g}^>(T + \Delta, t'), & \quad \mathbf{g}^<(t, T + \Delta), \\ \mathbf{g}^\lceil(T + \Delta, -i\tau'), & \quad \mathbf{g}^\lceil(-i\tau, T + \Delta), \end{aligned} \quad (\text{B.1})$$

are calculated while the Green's functions are assumed to be fully known for $t, t' \leq T$. If the time step Δ is small enough, one is allowed to approximate $\mathbf{h}(t) \approx \bar{\mathbf{h}}$ by its value at $T + \frac{\Delta}{2}$, and for $T \leq t \leq T + \Delta$ one may assume

$$\begin{aligned} \mathbf{I}_1^>(t, t') &\approx \mathbf{I}_1^>(t'), & \mathbf{I}_2^<(t', t) &\approx \mathbf{I}_2^<(t'), \\ \mathbf{I}^\lceil(t, -i\tau) &\approx \mathbf{I}^\lceil(-i\tau), & \mathbf{I}^\lceil(-i\tau, t) &\approx \mathbf{I}^\lceil(-i\tau). \end{aligned} \quad (\text{B.2})$$

Furthermore, as shown in Ref. [15], the time-stepping is essentially simplified by introducing the time-evolution operator

$$U(t) = \exp(-i\bar{\mathbf{h}}t), \quad (\text{B.3})$$

and defining new Green's function matrices $\tilde{\mathbf{g}}^{\gtrless}(t, t')$, $\tilde{\mathbf{g}}^\lceil(-i\tau, t')$ and $\tilde{\mathbf{g}}^\lceil(t, -i\tau')$ by

$$\mathbf{g}^{\gtrless}(t, t') = U(t) \tilde{\mathbf{g}}^{\gtrless}(t, t') U^\dagger(t'), \quad (\text{B.4})$$

$$\mathbf{g}^\lceil(t, -i\tau') = U(t) \tilde{\mathbf{g}}^\lceil(t, -i\tau'), \quad (\text{B.5})$$

$$\mathbf{g}^\lceil(-i\tau, t') = \tilde{\mathbf{g}}^\lceil(-i\tau, t') U^\dagger(t'). \quad (\text{B.6})$$

To obtain the equations of motion for these functions, one substitutes them into the general equations of motions (4.47-4.50) using the identities

$$i \partial_t \left\{ U(t) \tilde{\mathbf{g}}^>(t, t') U^\dagger(t') \right\} = -i^2 \bar{\mathbf{h}} U(t) \tilde{\mathbf{g}}^>(t, t') U^\dagger(t') + i U(t) \partial_t \tilde{\mathbf{g}}^>(t, t') U^\dagger(t'), \quad (\text{B.7})$$

$$-i \partial_t \left\{ U(t') \tilde{\mathbf{g}}^<(t', t) U^\dagger(t) \right\} = -i U(t') [\partial_t \tilde{\mathbf{g}}^<(t', t)] U^\dagger(t) - i^2 U(t') \tilde{\mathbf{g}}^<(t', t) \bar{\mathbf{h}} U^\dagger(t),$$

for the greater and lesser functions, and

$$-i \partial_t \left\{ \tilde{\mathbf{g}}^\lceil(-i\tau, t) U^\dagger(t) \right\} = -i \left[\partial_t \tilde{\mathbf{g}}^\lceil(-i\tau, t) \right] U^\dagger(t) - i^2 \tilde{\mathbf{g}}^\lceil(-i\tau, t) \bar{\mathbf{h}} U^\dagger(t), \quad (\text{B.8})$$

$$i \partial_t \left\{ U(t) \tilde{\mathbf{g}}^\lceil(t, -i\tau') \right\} = -i^2 \bar{\mathbf{h}} U(t) \tilde{\mathbf{g}}^\lceil(t, -i\tau') + U(t) \partial_t \tilde{\mathbf{g}}^\lceil(t, -i\tau'),$$

for the mixed functions. Thereby, terms on the r.h.s. of the Keldysh/Kadanoff-Baym equations cancel yielding after multiplication with time-evolution operators from the left and (or) right:

$$i \partial_t \tilde{\mathbf{g}}^>(t, t') = U^\dagger(t) \mathbf{I}_1^>(t, t') U(t'), \quad (\text{B.9})$$

$$-i \partial_t \tilde{\mathbf{g}}^<(t', t) = U^\dagger(t') \mathbf{I}_2^<(t', t) U(t), \quad (\text{B.10})$$

$$i \partial_t \tilde{\mathbf{g}}^\lceil(t, -i\tau') = e^{i\bar{\mathbf{h}}t} \mathbf{I}^\lceil(t, -i\tau') = U^\dagger(t) \mathbf{I}^\lceil(t, -i\tau'), \quad (\text{B.11})$$

$$-i \partial_t \tilde{\mathbf{g}}^\lceil(-i\tau, t) = \mathbf{I}^\lceil(-i\tau, t) e^{-i\bar{\mathbf{h}}t} = \mathbf{I}^\lceil(-i\tau, t) U(t). \quad (\text{B.12})$$

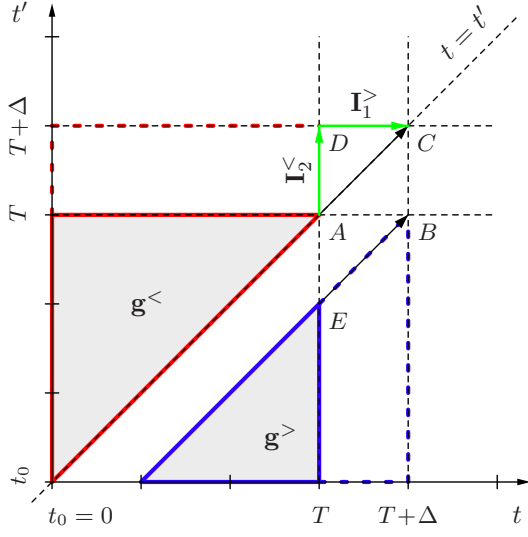


Figure B.1: 1.) Details for the time-stepping of the lesser correlation function on the time-diagonal $t = t'$: To propagate $\mathbf{g}^<$ from point A to point C one effectively has to follow the path \overline{ADC} using the respective collision integrals $\mathbf{I}_2^<$ and $\mathbf{I}_1^>$. 2.) Actually, a similar scheme could be applied to propagate $\mathbf{g}^>$ from point E to B . However, it is much simpler to start with $\mathbf{g}^<$ at A on the diagonal propagating it to B and afterward to use the symmetry properties to get the corresponding $\mathbf{g}^>$.

Note, that Eqs. (B.9) and (B.10) are restricted to $t \neq t'$ only. The equation of motion for $\tilde{\mathbf{g}}^<(t, t')$ on the time diagonal $t = t'$ is somewhat more complicated. As shown in Fig. (B.1), both types of collision integrals, $\mathbf{I}_1^>$ and $\mathbf{I}_2^>$, are needed to propagate the lesser correlation function from point $A = (T, T)$ via $D = (T, T + \Delta)$ to point $C = (T + \Delta, T + \Delta)$. Thus, the r.h.s. of the equation of motion for $\tilde{\mathbf{g}}^<(t, t)$ reads

$$i \partial_t \tilde{\mathbf{g}}^<(t, t) = U^\dagger(t) \mathbf{I}_{12}^< U(t), \quad (\text{B.13})$$

where, with the symmetry of (4.55) and $t, t' = \text{const.}$ in the interval $[T, T + \Delta]$, it is

$$\mathbf{I}_{12}^< \approx \mathbf{I}_1^<(t, t') - \mathbf{I}_2^<(t, t') = -[\mathbf{I}_1^>(t', t)]^\dagger - \mathbf{I}_2^<(t, t'). \quad (\text{B.14})$$

Once the equations of motion (B.9-B.13) are known, one can directly evaluate the original Green's functions in $T + \Delta$. Thereby, it is useful to have predefined the operator

$$V(\Delta) = \frac{1}{\hbar} (1 - \exp(-i \bar{\mathbf{h}} \Delta)). \quad (\text{B.15})$$

i. Calculate expression $\mathbf{g}^>(T + \Delta, t')$:

$$\begin{aligned} \mathbf{g}^>(T + \Delta, t') &= U(T + \Delta) \tilde{\mathbf{g}}^>(T + \Delta, t') U^\dagger(t') \\ &= U(T + \Delta) \left[\tilde{\mathbf{g}}^>(T, t') + \int_T^{T+\Delta} dt \partial_t \tilde{\mathbf{g}}^>(t, t') \right] U^\dagger(t') \\ &= U(\Delta) \mathbf{g}^>(T, t') - i U(T + \Delta) \int_T^{T+\Delta} dt U^\dagger(t) \underbrace{\mathbf{I}_1^>(t, t')}_{\approx \mathbf{I}_1^>(t')} \quad [(\text{B.9})] \\ &= U(\Delta) \mathbf{g}^>(T, t') - i U(\Delta) \left[\int_0^\Delta d\bar{t} \exp(i \bar{\mathbf{h}} \bar{t}) \right] \mathbf{I}_1^>(t') \\ &= U(\Delta) \mathbf{g}^>(T, t') - \underbrace{\frac{1}{\hbar} (1 - \exp(-i \bar{\mathbf{h}} \Delta))}_{= V(\Delta)} \mathbf{I}_1^>(t'). \end{aligned} \quad (\text{B.16})$$

ii. Calculate expression $\mathbf{g}^<(t', T + \Delta)$:

$$\begin{aligned}
 \mathbf{g}^<(t', T + \Delta) &= U(t') \tilde{\mathbf{g}}^<(t', T + \Delta) U^\dagger(T + \Delta) \\
 &= U(t') \left[\tilde{\mathbf{g}}^<(t', T) + \int_T^{T+\Delta} dt \partial_t \tilde{\mathbf{g}}^<(t', t) \right] U^\dagger(T + \Delta) \\
 &= \mathbf{g}^<(t', T) U^\dagger(\Delta) + i \int_T^{T+\Delta} dt \underbrace{\mathbf{I}_2^<(t', t)}_{\approx \mathbf{I}_2^<(t')} U(t) U^\dagger(T + \Delta) \quad [(B.10)] \\
 &= \mathbf{g}^<(t', T) U^\dagger(\Delta) + i \mathbf{I}_2^<(t') \left[\int_0^\Delta d\bar{t} \exp(-i \bar{\mathbf{h}} \bar{t}) \right] U(\Delta) \\
 &= \mathbf{g}^<(t', T) U^\dagger(\Delta) - \underbrace{\mathbf{I}_2^<(t') \frac{1}{\hbar} (1 - \exp(+i \bar{\mathbf{h}} \Delta))}_{= V^\dagger(\Delta)} . \quad (B.17)
 \end{aligned}$$

iii. Time-diagonal element $\mathbf{g}^<(T + \Delta, T + \Delta)$:

$$\begin{aligned}
 \mathbf{g}^<(T + \Delta, T + \Delta) &= U(T + \Delta) \tilde{\mathbf{g}}^<(T + \Delta, T + \Delta) U^\dagger(T + \Delta) \\
 &= U(\Delta) g^<(T, T) U^\dagger(\Delta) + U(T + \Delta) \int_T^{T+\Delta} dt \partial_t \tilde{\mathbf{g}}^<(t, t) U^\dagger(T + \Delta) \\
 &= U(\Delta) g^<(T, T) U^\dagger(\Delta) - i \int_0^\Delta d\bar{t} U(\Delta) U^\dagger(\bar{t}) \mathbf{I}_{12}^< \quad [(B.13)] \\
 &= U(\Delta) g^<(T, T) U^\dagger(\Delta) - i U(\Delta) \left[\int_0^\Delta d\bar{t} U^\dagger(\bar{t}) \mathbf{I}_{12}^< U(\bar{t}) \right] U^\dagger(\Delta) . \quad (B.18)
 \end{aligned}$$

The last term on the r.h.s of (B.18) is difficult to evaluate. However, one can make use of the operator series expansion

$$e^{\mathbf{A}} \mathbf{B} e^{-\mathbf{A}} = \mathbf{B} + [\mathbf{A}, \mathbf{B}] + \frac{1}{2} [\mathbf{A}, [\mathbf{A}, \mathbf{B}]] + \frac{1}{3} \left[\mathbf{A}, \left[\mathbf{A}, \frac{1}{2} [\mathbf{A}, \mathbf{B}] \right] \right] + \dots , \quad (B.19)$$

from which follows that

$$U^\dagger(\bar{t}) \mathbf{I}_{12}^< U(\bar{t}) = \mathbf{I}_{12}^< + i \bar{t} [\bar{\mathbf{h}}, \mathbf{I}_{12}^<] + \frac{i^2 \bar{t}^2}{2} [\bar{\mathbf{h}}, [\bar{\mathbf{h}}, \mathbf{I}_{12}^<]] + \dots . \quad (B.20)$$

Integrating Eq. (B.20) over time argument \bar{t} yields

$$\begin{aligned}
 -i \int_0^\Delta d\bar{t} U^\dagger(\bar{t}) \mathbf{I}_{12}^< U(\bar{t}) &= -i \mathbf{I}_{12}^< \Delta - \frac{i^2}{2} [\bar{\mathbf{h}}, \mathbf{I}_{12}^<] \Delta^2 - \frac{i^3}{6} [\bar{\mathbf{h}}, [\bar{\mathbf{h}}, \mathbf{I}_{12}^<]] \Delta^3 + \dots \\
 &=: \sum_{n=0}^{\infty} C^{(n)} , \quad (B.21)
 \end{aligned}$$

where the matrices $C^{(n)}$ are defined by the recursion relation $C^{(n)} = \frac{i\Delta}{n+1} [\bar{\mathbf{h}}, C^{(n-1)}]$ with initially $C^{(0)} = -i \mathbf{I}_{12}^< \Delta$. In total, one then has

$$\mathbf{g}^<(T + \Delta, T + \Delta) = U(\Delta) \left[\mathbf{g}^<(T, T) + \sum_{n=0}^{\infty} C^{(n)} \right] U^\dagger(\Delta) , \quad (B.22)$$

iv. Mixed Green's function $\mathbf{g}^\lceil(-i\tau, t' + \Delta)$:

$$\begin{aligned}
 \mathbf{g}^\lceil(-i\tau, t' + \Delta) &= \tilde{\mathbf{g}}^\lceil(-i\tau, t' + \Delta) U^\dagger(t' + \Delta) \\
 &= \left[\tilde{\mathbf{g}}^\lceil(-i\tau, t') + \int_{t'}^{t'+\Delta} dt \partial_t \tilde{\mathbf{g}}^\lceil(-i\tau, t) \right] U^\dagger(t' + \Delta) \\
 &= \tilde{\mathbf{g}}^\lceil(-i\tau, t') U^\dagger(\Delta) + i \int_{t'}^{t'+\Delta} dt \underbrace{\mathbf{I}^\lceil(-i\tau, t)}_{\approx \mathbf{I}^\lceil(-i\tau)} U(t) U^\dagger(t' + \Delta) \quad [(B.11)] \\
 &= \tilde{\mathbf{g}}^\lceil(-i\tau, t') U^\dagger(\Delta) + i \int_0^\Delta d\bar{t} \mathbf{I}^\lceil(-i\tau) U(\bar{t}) U^\dagger(\Delta) \\
 &= \tilde{\mathbf{g}}^\lceil(-i\tau, t') U^\dagger(\Delta) - \underbrace{\frac{1}{\hbar} (1 - \exp(+i \bar{\mathbf{h}} \Delta))}_{= V^\dagger(\Delta)} \mathbf{I}^\lceil(-i\tau). \quad (B.23)
 \end{aligned}$$

v. Mixed Green's function $\mathbf{g}^\lceil(t + \Delta, -i\tau')$:

$$\begin{aligned}
 \mathbf{g}^\lceil(t + \Delta, -i\tau') &= U(t + \Delta) \tilde{\mathbf{g}}^\lceil(t + \Delta, -i\tau') \\
 &= U(t + \Delta) \left[\tilde{\mathbf{g}}^\lceil(t, -i\tau') + \int_t^{t+\Delta} dt \partial_t \tilde{\mathbf{g}}^\lceil(t, -i\tau') \right] \\
 &= U(\Delta) \tilde{\mathbf{g}}^\lceil(t, -i\tau') - i \int_t^{t+\Delta} d\bar{t} \underbrace{\mathbf{I}^\lceil(t, -i\tau')}_{\approx \mathbf{I}^\lceil(-i\tau')} U^\dagger(\bar{t}) U(t + \Delta) \quad [(B.12)] \\
 &= U(\Delta) \tilde{\mathbf{g}}^\lceil(t, -i\tau') - i \mathbf{I}^\lceil(-i\tau') \int_0^\Delta d\bar{t} U^\dagger(\bar{t}) U(\Delta) \\
 &= U(\Delta) \tilde{\mathbf{g}}^\lceil(t, -i\tau') - \underbrace{\frac{1}{\hbar} (1 - \exp(-i \bar{\mathbf{h}} \Delta))}_{= V(\Delta)} \mathbf{I}^\lceil(-i\tau'). \quad (B.24)
 \end{aligned}$$

B.2. Computation of matrix elements $U_{ij}(\Delta)$ from $U(t) = \exp(-i \bar{\mathbf{h}} t)$

In order to calculate the matrix elements $U_{ij}(\Delta)$ of the time-evolution operator $U(t)$, one first needs to diagonalize the (self-)energy matrix \mathbf{h} obtaining the real eigenvalues ϵ_k and respective complex eigenvectors \mathbf{m}_k . With the eigenvectors being summarized as row-vectors in a matrix \mathbf{M} one then can express

$$U_{ij}(\Delta) = \sum_k M_{ki}^* M_{kj} \exp(-i \epsilon_k \Delta), \quad (B.25)$$

and it is easily proved that matrix $U(t)$ is unitary, i.e

$$\begin{aligned}
 \left(U^\dagger(t) U(t) \right)_{ij} &= \sum_\lambda U_{\lambda i}^*(t) U_{\lambda j}(t) \\
 &= \sum_{kl} \left(\sum_\lambda M_{k\lambda} M_{l\lambda}^* \right) M_{ki}^* M_{lj} \exp(+i \epsilon_k t) \exp(-i \epsilon_l t) \\
 &= \sum_k M_{ki}^* M_{kj} = \delta_{ij}, \quad (B.26)
 \end{aligned}$$

where the eigenvectors are orthonormal according to $\sum_k M_{ki}^* M_{kj} = \sum_k M_{ik} M_{jk}^* = \delta_{ij}$.

With the known eigensystem $\{\epsilon_k, \mathbf{m}_k\}$ it is also straightforward to compute the matrix elements $V_{ij}(\Delta)$ concerning Eq. (B.15) and Eq. (4.61) in Chap. 4, respectively.

C. Characterization of laser pulses

To study the system evolution under a time-dependent potential—such as a laser pulse with electric field $\mathcal{E}(t)$ —has been a detailed task of Chap. 6. Whereas in Sects. 6.2 and 6.3 mostly the system response to the pulse has been investigated, here, some general aspects concerning the characterization of short pulses are given. However, no explicit details are presented—for an extended overview of short-time laser pulses see e.g. Ref. [73], which covers both theoretical principles and experimental applications.

C.1. Duration and spectral width

Laser fields with envelope functions $F(t)$ and constraints $\lim_{t \rightarrow \pm\infty} F(t) = 0$ are well characterized by their temporal duration Δt and their spectral width $\Delta\omega$. These are accessible through the standard statistical averages

$$\langle \Delta t \rangle = \frac{\int_{-\infty}^{+\infty} t |F(t)|^2 dt}{\int_{-\infty}^{+\infty} |F(t)|^2 dt}, \quad \langle \Delta\omega^2 \rangle = \frac{\int_{-\infty}^{+\infty} \omega^2 |\tilde{F}(\omega)|^2 d\omega}{\int_{-\infty}^{+\infty} |\tilde{F}(\omega)|^2 d\omega}, \quad (\text{C.1})$$

with the Fourier transform $F(t) = \frac{1}{2\pi} \int_{-\infty}^{+\infty} d\omega \tilde{F}(\omega) \exp(-i\omega t)$. Further, it can be shown that both quantities are related through the so-called Fourier inequality, $\Delta t \Delta\omega \geq \frac{1}{2}$, where only for Gaussian time and spectral envelopes the equality holds. In particular, from this follows that one has to be able to manipulate wide spectra in order to realize a short duration. Δt and $\Delta\omega$ are well defined by (C.1) but experimentally not that easy to handle than are full width half-maximum quantities (FWHM). If one denotes $\Delta\bar{t}$ as the half-maximum duration and $\Delta\bar{\nu}$ as the frequency full width at half-maximum, the Fourier inequality can be stated in the form $\Delta\bar{t} \Delta\bar{\nu} = \kappa$, where κ is a pulse-shape depending constant. Table C.1 summarizes some of the most commonly used symmetrical pulse shapes including their characteristic κ -values.

In dipole approximation, interactions of the system with the laser field are described by a time-dependent electric field $\mathcal{E}(t)$ and a dipole moment d which enter the Hamiltonian as the external potential $V_{\text{ext}}(t) = d\mathcal{E}(t)$. Consisting of the amplitude vector \mathcal{E}_0 , the envelope function $F(t)$ and a time-dependent phase $\Phi(t)$ the electric field further reads

$$\mathcal{E}(t) = \Re \mathbf{e} \left(\mathcal{E}_0 F(t) e^{-i\Phi(t)} \right). \quad (\text{C.2})$$

The time-dependence of the phase thereby determines the instantaneous modulation frequency $\omega(t) = \partial\Phi/\partial t$ during the pulse. If $\partial_t\Phi \neq 0$, one generally speaks about a chirped pulse and when the electric field changes sign only a few times the pulse is referred to as a few cycle laser pulse.

Besides the pulse shapes enumerated in Table C.1, there exist another often used pulse whose electric field has the analytical form

$$\mathcal{E}(t) = \mathcal{E}_0 \sin^2(\pi t/\tau) \cos(\Omega t + \delta), \quad 0 \leq t \leq \tau, \quad (\text{C.3})$$

$$= \frac{1}{4} \mathcal{E}_0 [2 \cos(\Omega t + \delta) - \cos(\Omega^+ t + \delta) - \cos(\Omega^- t + \delta)], \quad (\text{C.4})$$

and equals zero outside the time interval $[0, \tau]$. Thereby, τ states the temporal duration, Ω denotes the modulation frequency and $\delta \in [-\frac{\pi}{2}, +\frac{\pi}{2}]$ is the pulse phase with respect to its

Pulse shape	$F(t)$	κ
Gaussian envelope	$\exp[-(t/t_p)^2/2]$	0.441
Exponential envelope	$\exp[-(t/t_p)/2]$	0.140
Hyperbolic secant	$1/\cosh(t/t_p)$	0.315
Cardinal sine	$\sin^2(t/t_p)/(t/t_p)^2$	0.336
Lorentzian envelope	$[1 + (t/t_p)^2]^{-1}$	0.142

Table C.1: Various pulse shapes and corresponding values of κ (quoted from Ref. [73]), obtained from the FWHM quantities $\Delta\bar{t}$ and $\Delta\bar{\nu}$.

maximum. The decomposition (C.4) into three different cosine contributions including two additional lateral frequencies $\Omega^\pm = \Omega \pm 2\pi/\tau$ is easily obtained by applying addition theorems, and reveals the main spectral features of this pulse which will affect the system response during laser excitations. The simplicity of the frequency spectrum further simplifies the analysis of time-dependent phenomena and their interpretation.

D. Record of (frequently) used abbreviations and symbols

Abbreviation	Explanation
BEC	Bose-Einstein condensate/condensation
CE	canonical ensemble
COM	center of mass
CPU	central processing unit
DFT	density functional theory
GCE	grand canonical ensemble
GEP	generalized eigenvalue problem
GF	Green's function
HF	Hartree-Fock
HFO	Hartree-Fock orbital(s)
KKBE	Keldysh/Kadanoff-Baym equations
KMS	Kubo-Martin-Schwinger (boundary conditions)
KT	(quantum) kinetic theory
LDA	local density approximation
MGF	Matsubara (equilibrium) Green's function
NEGF	nonequilibrium Green's function
NO	natural orbital(s)
PIMC	path-integral Monte-Carlo
PT	perturbation theory
QFT	quantum-field theory
QMC	quantum Monte-Carlo
SCHF	self-consistent Hartree-Fock
TDDFT	time-dependent density functional theory
TDHF	time-dependent Hartree-Fock
TDSE	time-dependent Schrödinger equation
UPM	uniform power-mesh
XC	exchange

Table D.1: *List of (introduced) abbreviations in alphabetical order.*

D. Record of (frequently) used abbreviations and symbols

Symbol	Explanation
$l = (x_1, t_1)$	space-time coordinate
N	particle number
m	particle mass
q_0	particle charge
x_0	confinement length *
Ω	confinement frequency *
$E_0 = \hbar\Omega$	confinement energy *
$\beta = 1/(k_B T)$	inverse temperature (k_B : Boltzmann constant, T : temperature)
$\beta_0 = E_0^{-1}$	measure of inverse temperature *
α	interaction strength
a_B	(effective) Bohr radius
λ	coupling parameter (relative interaction strength)
$G(1, 2); \mathbf{g}(t_1, t_2)$	nonequilibrium Green's function; basis representation of G
$\Sigma(1, 2); \mathbf{\Sigma}(t_1, t_2)$	self-energy; basis representation of Σ
$A(1, 2); \mathbf{A}(t_1, t_2)$	spectral function; basis representation of A
$G^M, G^{\gtrless}, G^{\uparrow/\downarrow}$	subordinated quantities: Matsubara, correlation and mixed function(s)
$\Sigma^{\text{HF}}; \Sigma^{\text{corr(B)}}$	Hartree-Fock self-energy; correlation part (Born approx.)
\mathcal{C}	(Schwinger)/Keldysh-contour
$T_{\mathcal{C}}$	time-ordering operator acting on the Keldysh-contour
$\delta_{\mathcal{C}}(1 - 2)$	contour delta function
$\Psi^{(\dagger)}; \Psi_H^{(\dagger)}$	bosonic/fermionic field operator; Heisenberg representation
$c_i^{(\dagger)}(t)$	creation/annihilation operator in the Heisenberg picture
$\phi_i^{(*)}(x)$	basis functions, natural orbitals (NO)
$\Phi_i^{(*)}(x)$	Hartree-Fock orbitals (HFO)
ϵ_i	Hartree-Fock energy eigenvalues
A_{ij}	Hartree-Fock eigenvectors
n_b	number of (HFO) basis functions
(u, p)	uniform power-mesh (UPM) parameters
n_{Δ}	number of time-steps with spacing Δ
μ	chemical potential
ρ	density matrix
$n_k(t)$	time-dependent occupation probability of HFO k
a	small parameter within the pair-interaction potential $w(x, y) = [\sqrt{(x-y)^2 + a^2}]^{-1}$
$n(1) = n(x_1, t_1)$	time-dependent spatial resolved density
$d(t); \mathbf{d}(t)$	time-dependent dipole moment; basis representation of d
$h^0(1); \mathbf{h}^0(t_1)$	one-particle energy; basis representation of h^0
$w(x-y); w_{ij,kl}$	pair-interaction potential; respective matrix elements
$\mathcal{E}(t)$	time-dependent electric field strength
ω	laser (modulation) frequency

Table D.2: List explaining (frequently) used symbols. * means corresponding to a parabolic trap.

References

- [1] D.J. Wineland, J.C. Bergquist, W.M. Itano, J.J. Bollinger, and C.H. Manney, Phys. Rev. Lett. **59**, 2935 (1987).
- [2] D.H.E. Dubin, and J.P. Schiffer, Phys. Rev. E **53**, 5249 (1996).
- [3] O. Arp, D. Block, A. Piel, and A. Melzer, Phys. Rev. Lett. **93**, 165004 (2004).
- [4] M. Bonitz, D. Block, O. Arp, V. Golubnychiy, H. Baumgartner, P. Ludwig, A. Piel, and A. Filinov, Phys. Rev. Lett. **96**, 075001 (2006).
- [5] L. Brey, N.F. Johnson, and B.I. Halperin, Phys. Rev. B **40**, 10647 (1989).
- [6] A.V. Filinov, M. Bonitz, and Yu.E. Lozovik, Phys. Rev. Lett. **86**, 3851 (2001).
- [7] *Bose-Einstein Condensation in Dilute Gases*, C.J. Pethick and H. Smith, Cambridge, New York (2002).
- [8] *Electrons in artificial atoms*, R.C. Ashoori, Nature (London) **379**, 413 (1996).
- [9] S. Bednarek, B. Szafran, and J. Adamowski, Phys. Rev. B, **59**, 13036 (1999).
- [10] C. Yannouleas and U. Landman, Phys. Rev. B **61**, 15895 (2000).
- [11] *Progress in Nonequilibrium Greens's Functions III*, M. Bonitz and A. Filinov (Eds.), J. Phys.: Conf. Ser. **35** (2006).
- [12] *Quantum Kinetic Theory*, M. Bonitz, B.G. Teubner, Stuttgart/Leipzig (1998).
- [13] *Introduction to Computational Methods in Many-Body Physics*, Michael Bonitz and Dirk Semkat (Eds.), Rinton Press, Princeton (2006).
- [14] *Quantum Statistical Mechanics*, Leo P. Kadanoff and Gordon Baym, W.A. Benjamin, Inc., New York (1962).
- [15] N.E. Dahlen, R. van Leeuwen, and A. Stan, J. Phys.: Conf. Ser. **35**, 324-339 and 340-348 (2006).
- [16] N.E. Dahlen and R. van Leeuwen, Phys. Rev. Lett. **98**, 153004 (2007).
- [17] *Quantum Theory of Many-Particle Systems*, A.L. Fetter and J.D. Walecka, McGraw-Hill Book Company, New York (1971).
- [18] *Methods of the Quantum Field Theory in Statistical Physics*, A.A. Abrikosov, L.P. Gorkov and I.E. Dzyaloshinskii, Pergamon, Oxford (1965).
- [19] *Many-Particle Physics, Second edition*, Gerald D. Mahan, Pergamon, Plenum Press, New York (1990).
- [20] T. Matsubara, Prog. Theor. Phys. **14**, 351-378 (1955).

- [21] G. Baym and L.P. Kadanoff, Phys. Rev. **124**, 287 (1961).
- [22] L.V. Keldysh, ZhETF **47**, 1515 (1964) [Sov. Phys.-JETP **20**, 235 (1965)].
- [23] *Self-consistent Quantum-Field Theory and Bosonization for Strongly Correlated Electron Systems*, Rudolf Haussmann, Springer, Berlin-Heidelberg (1999).
- [24] *Progress in Nonequilibrium Green's functions II*, M. Bonitz and D. Semkat (Eds.), World Scientific, New Jersey (2003).
- [25] Paul C. Martin and Julian Schwinger, Phys. Rev. **115**, 1342 (1959).
- [26] R. Kubo, J. Phys. Soc. Jpn. **12**, 570 (1957); Rep. Prog. Phys. **29**, 255 (1966).
- [27] E. Wigner, Phys. Rev. **40**, 749-759 (1932).
- [28] *Progress in Nonequilibrium Green's functions I*, M. Bonitz (Ed.), World Scientific Publ., Singapore (2000).
- [29] P. Danielewicz, Ann. Phys. (N.Y.) **152**, 305 (1984).
- [30] H.S. Köhler, Phys. Rev. C **51**, 3232 (1995).
- [31] P. Božek, Phys. Rev. C **56**, 1452 (1997).
- [32] Yu.B. Ivanov, J. Knoll, and D.N. Voskresensky, Nucl. Phys. A **657**, 413 (1999).
- [33] *Lectures in Theoretical Physics*, D.F. DuBois, edited by W.E. Brittin, Gordon and Breach, New York (1967); B. Bezzerides and D.F. DuBois, Ann. Phys. (N.Y.) **70**, 10 (1972).
- [34] *Quantum Statistics of Nonideal Plasmas*, D. Kremp, M. Schlanges, and W.D. Kraeft, Springer, Heidelberg-New York (1996).
- [35] D. Kremp, D. Semkat, and M. Bonitz, J. Phys.: Conf. Ser. **11**, 1-13 (2005).
- [36] N.H. Kwong and M. Bonitz, Phys. Rev. Lett. **84**, 1768 (2000).
- [37] D. Semkat, D. Kremp, and M. Bonitz, Phys. Rev. E, **59**, 1557 (1999).
- [38] M. Bonitz, D. Kremp, D.C. Scott, R. Binder, W.D. Kraeft, and H.S. Köhler, J. Phys.: Cond. Mat. **8**, 6057 (1996).
- [39] K. Henneberger and H. Haug, Phys. Rev. B **38**, 9759 (1988).
- [40] *Quantum Theory of the Optical and Electronic Properties of Semiconductors*, Hartmut Haug and Stephan W. Koch, World Scientific, Singapore (2004).
- [41] *Quantum Kinetics in Transport and Optics of Semiconductors*, H. Haug and A.-P. Jauho, Springer, Berlin-Heidelberg (1996).
- [42] R. Binder, H.S. Köhler, and M. Bonitz, Phys. Rev. B **55**, 5110 (1997).
- [43] N.H. Kwong, M. Bonitz, R. Binder, and S. Köhler, phys. stat. sol. (b) **206**, 197 (1998).
- [44] P. Gartner, J. Seebeck, and F. Jahnke, J. Phys.: Conf. Ser. **35**, 175-181 (2006); M. Lorke, T.R. Nielsen, J. Seebeck, P. Gartner, and F. Jahnke, J. Phys.: Conf. Ser. **35**, 182-189 (2006).

-
- [45] R. van Leeuwen, Phys. Rev. Lett. **76**, 3610 (1996).
- [46] W. Kohn, Phys. Rev. **123**, 1242 (1961).
- [47] S.V. Faleev and M.I. Stockman, Phys. Rev. B **62**, 16707 (2000).
- [48] N.E. Dahlen and R. van Leeuwen, J. Chem. Phys **122**, 164102 (2005).
- [49] A. Stan, N.E. Dahlen, and R. van Leeuwen, Europhys. Lett. **76** (2), 298-304 (2006).
- [50] K.M. Indlekofer, J. Knoch, and J. Appenzeller, Phys. Rev. B **72**, 125308 (2005).
- [51] D. Semkat, D. Kremp, and M. Bonitz, J. Math. Phys. **41**, 7458 (2000).
- [52] *Grundkurs Theoretische Physik 5/2, Quantenmechanik—Methoden und Anwendungen*, W. Nolting, Springer, Berlin-Heidelberg (2004).
- [53] G. Cuniberti, E. De Micheli, G.A. Viano, Commun. Math. Phys. **216**, 59-63 (2001).
- [54] G. Baym, Phys. Rev. **127**, 1391 (1962).
- [55] *Many-Body Problems and Quantum Field Theory, An Introduction*, Ph.A. Martin and F. Rothen, Springer, Berlin-Heidelberg (2002).
- [56] *Modern-Many Particle Physics—Atomic Gases, Quantum Dots and Quantum Fluids*, Enrico Lipparini, World Scientific, Singapore (2003).
- [57] *Introduction to Computational Chemistry*, Frank Jensen, John Wiley & Sons Ltd., Chichester (1999).
- [58] *Reviews in Computational Chemistry*, Kenny B. Lipkowitz and Donald B. Boyd (Eds.), VCH Publishers, Inc. (1990).
- [59] C.C.J. Roothaan, Rev. Mod. Phys. **20**, 69 (1951); G.G. Hall, Proc. R. Soc. (London) **A205**, 451 (1951).
- [60] Wei Ku and Adolfo G. Eguiluz, Phys. Rev. Lett. **89**, 126401 (2002).
- [61] H.S. Köhler, N.H. Kwong, and H.A. Yousif, Comp. Phys. Comm. **123**, 123 (1999).
- [62] *Introduction to Perturbation Theory in Quantum Mechanics*, Francisco M. Fernández, CRC Press LLC, Boca Raton (2001).
- [63] W. Wonneberger, Phys. Rev. A **63**, 063607 (2001).
- [64] F. Gleisberg, W. Wonneberger, U. Schlöder, and C. Zimmermann, Phys. Rev. A **62**, 063602 (2000).
- [65] P. Vignolo and A. Minguzzi, J. Phys. B: At. Mol. Opt. Phys. **34**, 4653-4662 (2001).
- [66] Z. Akdeniz, P. Vignolo, A. Minguzzi, and M.P. Tosi, Phys. Rev. A **66**, 055601 (2002).
- [67] S.N. Artemenko, Gao Xianlong, and W. Wonneberger, J. Phys. B: At. Mol. Opt. Phys. **37**, 49-58 (2004).
- [68] J. Friedel. Nuovo Cimento Suppl. **7**, 287 (1958).
- [69] K. Balzer, C. Nölle, M. Bonitz, and A. Filinov, J. Phys.: Conf. Ser. **35**, 209-218 (2006).

- [70] K. Balzer, C. Nölle, M. Bonitz, and A. Filinov, *phys. stat. sol. (c)* **3**, 2402-2405 (2006).
- [71] Muoi N. Tran, M.V.N. Murthy, and R.K. Bhaduri, *Phys. Rev. E.* **63**, 031105 (2001).
- [72] M. Bonitz, K. Balzer, and R. van Leeuwen, to be published, arXiv:cond-mat/0702633 (2007).
- [73] *Femtosecond Laser Pulses*, Claude Rullière (Ed.), Springer Science+Business Media, Inc. (2005).
- [74] B. Velický, A. Kalvová, and V. Špička, *J. Phys.: Conf. Ser.* **35**, 1-16 (2006).
- [75] *Mathematica und C in der modernen Theoretischen Physik mit Schwerpunkt Quantenmechanik*, Jens-Peer Kuska, Springer-Verlag, Berlin Heidelberg (1997).

Acknowledgments

First of all, I am very grateful to Prof. Dr. Michael Bonitz, who has been a committed supervisor during this work. I acknowledge his way and support of leading students like me to independent scientific work. Due to his specialist knowledge and guiding comments he has played a part in progress of this treatise.

I also express thanks to the theoretical chemists Prof. Dr. Robert van Leeuwen and Dr. Nils Erik Dahlen at the Zernike Institute of Advanced Materials (University of Groningen, The Netherlands), who invited me to Groningen in June 2006 to learn much about nonequilibrium Green's functions and their—in particular numerical—applicability to atoms and molecules. Without their detailed theoretical and numerical understanding I would not have come that far in the present thesis.

Furthermore, I would like to thank the whole study group, which I always found as helpful and considerate and which offers a lively and kind working atmosphere. Special thanks are thereby due to my—now former—office colleague Andrea Fromm whose presence often led to stimulating discussions on both physical grounds and subjects (far) beyond.

It is due to Prof. Dr. Barbara Schrempp's generous efforts that I, in addition, may thank the German National Merit Foundation (Studienstiftung des Deutschen Volkes) for a many and diverse accompaniment and financial support of my six-month study abroad in Perth (Western Australia) in 2004 and my final period of study in Kiel.

Finally ☺, many many words of thanks are devoted to my family and my lovable girlfriend Bożena Magrowska.

Eidesstattliche Erklärung

Die vorliegende Arbeit ist von mir selbständig und nur unter Zuhilfenahme der angegebenen Quellen und Hilfsmittel angefertigt worden.

(Ort, Datum)

(Unterschrift)